Optimisation of VSC-HVDC Transmission for Wind Power Plants

Silva, Rodrigo Da

Publication date:
2012

Optimisation of VSC-HVDC Transmission for Wind Power Plants

by

Rodrigo da Silva

Dissertation submitted to Faculty of Engineering, Science, and Medicine at Aalborg University in partial fulfilment of the requirements for the degree of Doctor of Philosophy in Electrical Engineering

Aalborg University
Department of Energy Technology
Aalborg, Denmark
October 2012

Aalborg University
Department of Energy Technology
Pontoppidanstræde 101
9220 Aalborg East
Denmark
Phone: +45 9940 9240
Fax: +45 9815 1411
Web: http://www.et.aau.dk

Printed in Denmark by UniPrint
ISBN

Abstract

Connection of Wind Power Plants (WPP), typically offshore, using VSC-HVDC transmission is an emerging solution with many benefits compared to the traditional AC solution, especially concerning the impact on control architecture of the wind farms and the grid.

The VSC-HVDC solution is likely to meet more stringent grid codes than a conventional AC transmission connection. The purpose of this project is to analyse how HVDC solution, considering the voltage-source converter based technology, for grid connection of large wind power plants can be designed and optimised. By optimisation, the project aims to study the control of DC grids.

The first part considers the static analysis of the multiterminal DC connection. An optimal design methodology for loss minimisation and one based in the dispatch error minimisation are proposed. The algorithm outputs are the droop factors which are included as most outer controllers in the onshore shore converter stations. With the voltage drops given by the controllers, the schedule dispatch for the DC grid is then defined.

The optimisation technique applied in the definition of the droop factor in the multiterminal control mode presents flexibility in meeting the requirements established by the operators in the multiterminal VSC-HVDC transmission system. Moreover, the possibility in minimising the overall transmission losses can be a solution for small grids and the minimisation in the dispatch error is a new solution for power deliver maximisation.

The second study takes into account the dynamics of the system. The converter stability analysis is performed and, from its results, the optimisation criteria used fo the static operation of multiterminal DC systems can be refined. The application of the robust control technique based in μ-synthesis appears as a contribution to the study of parameter variations in the DC systems. This method is able to simplify the system modelling, considering the range of variations of the system variables instead of the use of a complete dynamic description of interconnected system.

The performance of the system dynamics when the robust control technique is applied is compared with the classical proportional-integral (PI) performance, by means of time domain simulation in a point-to-point HVDC connection. The three main parameters in the discussion are the wind power delivered from the offshore wind power plant, the variation of the DC voltage reference in the onshore converter station and, at the end, the grid equivalent short-circuit ratio

impedance.

Connecting both, the static optimisation and dynamic analysis, the project is a starting point to the quantification of the ability of the system in support standalone operation and/or justify the insertion of high speed communication link whether the robust performance of the system does not meet the requirements established by the partners tied by the HVDC multiterminal link as an example.

The study of the system stability using uncertainty model can simplify the analysis of large networks in order to design the control parameters of voltage source converters. This technique, based in structure singular values and the control design by means of μ-synthesis, presents as disadvantages the use of higher order controllers. On the other hand, the improvements in the dynamic performance under system variations justify the usage of such approach.

Abstrakt

Tilslutning af vindkraftværker (WPP), typisk offshore ved hjælp VSCHVDC transmission er en spirende løsning med mange fordele i forhold til den traditionelle AC løsning, navnlig vedrørende indvirkningen påstyringsarkitektur af vindmølleparkerne og gitteret.

Den VSC-HVDC løsning vil kunne opfylde de andre netkrav end en konventionel AC transmission forbindelse. Formålet med dette projekt er at analysere, hvordan HVDC løsning, overvejer spænding-source converter baseret teknologi, for nettilslutning af større vindkraftværker kan designes og optimeres. Ved optimering, sigter projektet mod at studere kontrol af DC tavler.

Den første del mener statisk analyse af den multiterminal jævnstrømsforbin - delse. En optimal design metode til tab minimering og en baseret påforsendelsen fejl minimering foreslås. Algoritmen udgange er de hænge faktorer, der indgår som mest ydre controllere i onshore shore omformerstationer. Med spændingen falder givet af de tilsynsførende, er tidsplanen afsendelse til DC gitteret derefter defineret.

Den optimering teknik anvendt i definitionen af droop faktor i den multiterminal styremode præsenterer fleksibilitet i opfyldelsen af de krav, som de erhvervsdrivende i den multiterminal VSC-HVDC transmissionssystem. Desuden kan muligheden i at minimere de samlede transmissionstab være en løsning for smånet og minimering i forsendelsen fejl er en ny løsning i forhold til den klassiske sum af vægt kvadrater om magten levere maksimering.

Den anden undersøgelse tager hensyn til systemets dynamik. Konverteren stabilitet analyse udføres, og fra dets resultater, brugte optimeringskriterier fo den statiske drift af multiterminal DC-systemer kan forbedres. Anvendelsen af den robuste kontrol teknik baseret på μ-syntese vises som et bidrag til studiet af parameter variationer i DC-systemer. Denne fremgangsmåde kan forenkle systemmodellering, overvejer, hvilke variationer påsystemvariablene stedet for anvendelsen af en fuldstændig dynamisk beskrivelse af sammenkoblede system.

Udførelsen af systemets dynamik, når den robuste kontrol teknik anvendes sammenlignes med den klassiske proportional-integral (PI) ydelse, ved hjælp af tids-domÃ¦ne simulering i et punkt-til-punkt HVDC-forbindelse. De tre vigtigste parametre i diskussionen er leverede vindkraft fra offshore vindkraftværk, variationen af DC spænding reference i onshore converter station og i sidste ende, er gitteret tilsvarende kortslutningsforhold impedans.

Tilslutning begge, den statiske optimering og dynamisk analyse af projektet er

et udgangspunkt for kvantificeringen af systemets evne til støtte standalone operation og / eller begrunde indsættelsen af højhastigheds kommunikationsforbindelse hvorvidt den robuste ydeevne systemet ikke opfylder de krav, som de partnere bundet af den HVDC multiterminal link som et eksempel.

Undersøgelsen af systemets stabilitet ved hjælp af usikkerheden model kan lette analysen af store netværk med henblik på at udforme styreparametre spændingskildeorgan omformere. Denne teknik, der er baseret på struktur singulære værdier og kontrol design ved hjælp af μ-syntese, viser som ulemper anvendelsen af højere orden controllere. På den anden side, begrunder de forbedringer i den dynamiske ydeevne under System variationer brugen af en sådan metode.

Acknowledgements

The gratitude for enhancement in both, academic and personal skills, are difficult to measure after the three years journey. For all the people who, directly or indirectly helped with this work, I would like to express my thankfulness and gratitude for all the efforts and patience in having this work complete.

First of all, I would like to kindly thank Aalborg University and Vestas Energy System S/A, for the financial support. Thanks, as well, for the Department of Energy Technology in providing the appropriate infrastructure to conduct the project .

I would like to express my sincerest gratitude to all my supervisors. My gratitude must be expressed to my main supervisor, Professor Remus Teodorescu. My thanks to Professor Pedro Rodriguez who was my co-supervisor during the period of October/2009 to December/2011. My appreciation for the contribution of Professor Claus Leth Bak for his supervision from September/2012 to October/2012. My many thanks to Sanjay Chaudhary for the thesis review and technical discussions.

My gratitude for the Vestas Reference Group, Philip Carne Kjaer and Jen Pale, who provided guidance and technical contribution for the entire project. Thanks as well for Florin Iov for the unofficial contributions and comments. Thanks for the friend Lorenzo Zeni, who I had the pleasure to work with for a short period of time.

Special thanks to Professor Udaya D. Annakkage, Professor at the University of Manitoba, Canada, who was my host professor during my study abroad period. Dr. Annakkage provided me the support in some topics of my work regarding stability analysis of power systems. The conversations were very fruitful.

To all my colleagues from the Vestas Power Program who shared with me their knowledge and friendship, my gratitude. Thanks for all the colleagues from the Department of Energy Technology.

My special thanks to wife, Larissa Bittencourt da Silva, who has been supporting me from the beginning of this challenging period. To her patience, helpfulness and love, thanks. To all my family, my Father, my Mother and my Brother.

Rodrigo da Silva
Aalborg, Denmark
October, 2012

Contents

Introduction

Background

According to the European Commission the electricity consumption in 2012 in the European Union was about 868.7 TWh. In comparison with the fourth quarter from 2011, the growth is 6.8%. This global trend in the continuous rise of the electricity consumption is consequence of economic issues. Nowadays, more markets are becoming important. Big economies such as United States and European Union are, recently, sharing the opportunities with other countries. The main representation of economic developments is China, with rates averaging 10% over the 30 years past. As a consequence, the seek for energy resources is a necessity and, with the environmental recent appeals, the most attractive candidates for replacement and combination with the usual electricity supplies are renewables: wind and solar energy.

The clean energy, has received increasingly investments mainly due to governmental initiatives. The policy for the commitment in reducing carbon emission reached the level of legislation. The European Commission, for example, launched the *20-20-20* which sets the following targets for 2020:

- 20% reduction of gas emission in comparison with the levels from 1990
- 20% rise in energy consumption originated from renewable resources
- 20% efficiency improvements

Following the tendency, the market of the wind energy has grown. According to data from the *European Wind Energy Association* (EWEA), after the hydropower contribution, wind is the fastest growing source of renewable energy. In the *2011 European Statistics* from EWEA, during 2011, 9616 MW of wind infrastructure was installed in the European Union. From this amount, 8750 MW are onshore installations and the minor 866 MW is the offshore contribution. Those values are related with investments about €10.2 *billion* for the onshore market and 2.4 *billion* for the offshore. The main contributor for the numbers is Germany, with a 2100 MW new installations in 2011. UK and Spain are the followers with 1300 MW and 1050 MW, respectively. A map for the wind energy installation shares for European Union Nations is given by figure 1.

Another interesting scenarios presented by the market trend is the move from the installation on land to the ones placed on the sea sites. Despite the fact

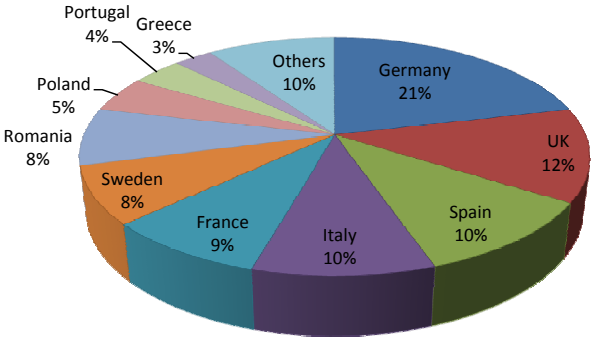

Figure 1: *EU members shares for installed wind capacity by 2011.*

that being more costly, the offshore wind farms are under the effect of more constant wind profiles with less obstacles and more constant. This means that the production can be higher and the payback time can justify the investments. In order to illustrate the the current scenario of the offshore and onshore wind market, figure 2 illustrates the history and perspectives between the onshore and offshore wind markets.

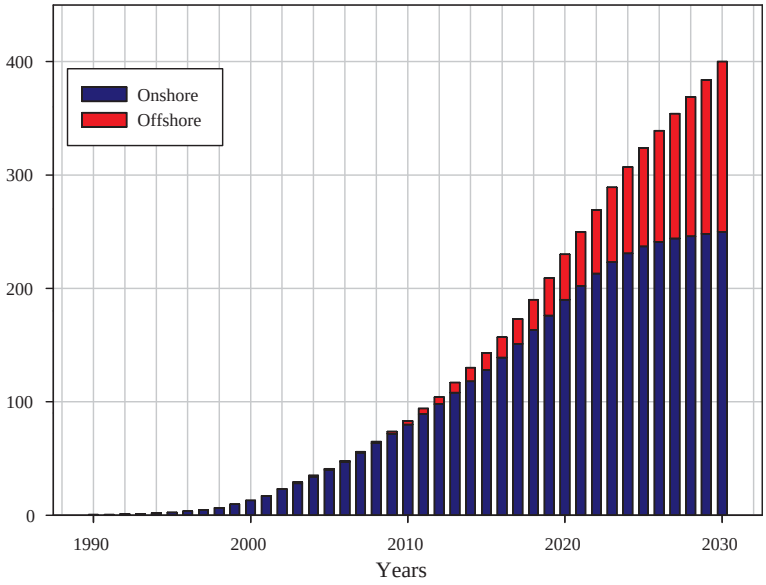

Figure 2: *Installed wind power capacity in the EU and prospects up to 2030.*

As a consequence of the increase in the offshore wind market, the necessity to transmit bulk amount of energy, produced offshore by the wind farms, to the land is, nowadays, a must. The AC solution, in deep sea applications, is not practical due to the necessity of cable reactive power compensation. In some cases, the HVAC connection is not even possible.

The second solution for power transmission is the use of classical Line Commu-

tated Converters (LCC). However, this topology presents some drawbacks with regard to the black start capability and connection with weak offshore grids. Besides those facts, usually the converter station has larger size and weight compared to the VSC solution. The main advantage in the LCC case is still in the loss level as well as in the capability to support higher voltages at the DC link due to the switching devices range of operation.

With the Voltage Source Converters (VSC), which are nowadays available for high voltage and high power range operation, the HVDC can offer the same advantages that the LCC case presents over the HVAC transmission system added with the advantages in overtake the deficiencies that the thyristor solution is unable to offer to offshore applications.

Motivation and Objectives

The clear trend in the market of offshore wind and its alliance to the VSC-HVDC technology bring the necessary justification for its selection as a research project. The classical control of voltage source converter is an established knowledge, however, its interaction with large networks and their dynamics is still a challenge. The study of controllers, which can improve the performance of the DC transmission systems, can be in the same direction as the increase in the requirements requested by the grid codes.

The aims of this work is to demonstrate that modern control solutions can be applicable to the field of High Voltage Transmission DC Systems bringing better performance and flexibility to the operation of voltage source converters tied to the grid utilities.

As hypothesis of the work, the list below shows the considerations assumed to the developments:

1. The connection of large offshore wind power plants has the most attractive candidate the VSC-HVDC solution. The wind turbines are equipped with full-scale converters and they act as controllable current sources. Their amplitude and frequency are dependent of the voltage and frequency imposed by the offshore HVDC converter.

2. The offshore HVDC converter directly controls the AC voltage at the terminals at the point of common coupling (PCC). The current controls are internal and are integrated in the system to improve stability and protection for the converter. The dynamic of the power which comes from the wind farm is totally delivered to the DC network (despite losses).

3. In a multiterminal DC case, the connection with multiple offshore and onshore stations can be operated by means of droop controllers applied on the stations where the DC voltage control mode are active. The variation in the DC voltage levels must be appropriate chosen in order to comply with the requirements imposed by the utility grids connected to the DC

network. The droop factor can be selected considering limitations of the lines, power distribution such that the losses in the system are minimised or even minimisation of the power sharing among receiving end stations.

4. The dynamic properties of the transfer power corridor offered by the HVDC link can have the performance improved in case of lower bandwidth. The classical proportional integral controllers are welcome in the application due to the simplicity and robustness. However, in this case, the increase in the order of the control architecture can improve the dynamic properties of the converter operation during transients.

Simulation Tools

Two main analysis are developed in this work. The first one is related to the static analysis which considers the selection of the droop controller parameters in a multiterminal network. At this point the use of low flow analysis is the main simulation platform. Matlab® is the mathematical software to develop the coding for the load flow. All the statical models, cable and converters, are included in the load flow solution. For the droop factor selection the Optimisation Toolbox offered by this platform is applied.

For the dynamic analysis the time domain is required. The PSCAD/EMTDC simulation software was selected. The choice of this platform lies in the fact that it is a well established simulation toll for the power system studies. There, the switched model of the converter and control simulations are integrated.

For the robust control design, the Robust Control Toolbox is selected to design the controller. The use of uncertainty model, linear fraction transformation and $D-K$ iteration are crucial to the dynamic developments. This toolbox provided all the necessary apparatus to the design of the augmented control techniques applied in the work.

The small signal stability models are derived analytically and included in Matlab® for the control design. For model validation, the small signal model was compared with the non-linear model, in time domain, using PSCAD. This connection is provided by means of development of C code and its integration with EMTDC simulations.

Limitations

It was assumed from the offshore side that wind turbines are equipped with permanent magnet synchronous generators and connected with the offshore grid by means of full-scale converters. The aggregation and simplification of this power plant reaches the level of considering the entire wind farm as an unique current

source where its value is dependent of the power order, simulating the wind scenario, and the voltage imposed by offshore converter. In the dynamic studies, the power reference order can change up to 1 ms as worst case scenario.

The HVDC converter topology is the two-level type. In the current market, the two level bridge seems to be obsolete, however, the benefits in the dynamic properties presented by the controller applied in the two-level case can be extended to the modular multilevel converter by generalisation. The loss model presented by the static analysis can be replaced by the loss model of the modular converter and included in the optimal load flow analysis.

The cables are simplified by π-section. The parameters of each section are described in the text when they are required. The minimum section size is 25 km.

The utility grid is simplified to a Thevenin model. The short circuit ratios vary from three to five in the dynamic analysis. The converter transformer is simplified by a series connected inductance included in the impedance presented by the grid. The converter high frequency filters present one branch tuned at the switching frequency value.

Outline of the Thesis

The thesis is structure in the following chapter contents:

Chapter 1:

This chapter is an introduction to HVDC technologies. A brief comparison among the Line Commutated and Voltage Source Converters is given. The trends in the switching devices and the connection with new converter topologies are included. The chapter finalises with a description of possible applications of VSC technologies with projects already in operation and prospects for future projects.

Chapter 2:

The concept of supergrids comes with the introduction of multiterminal DC networks. In this stage of the work, there are discussions regarding the prospectives of the HVDC technologies to become a mature technology and to be the backbone to the creation of DC grids. Some challenges in the role are pointed and an introduction about the control concepts for meshed DC networks are described. References concerning technical and economical matters are included during the descriptions.

Chapter 3:

This chapter focus in the control of multiterminal DC systems. The droop control was chosen as the most attractive candidate to operate the multiterminal DC system. The study of optimisation in the definition of the droop controllers is the centre part of the chapter. The guidelines required by the operation of the DC grid as well as system limitations are included in the control parameter definition. Two main cases are analysed and the results compares the advantages

and disadvantages in each of the operation modes.

Chapter 4:

The small signal analysis of a point-to-point VSC-HVDC is the main topic in this chapter. The theory of small signal and averaging model are the main tools to derive the analytical model of a two-level voltage source converter in two operation modes. The first operation mode is used for offshore control of AC voltages emulating an infinite bus for the operation of the wind farms. The second control mode is applied at the onshore sites and the DC outer control loop is the actuator in the balancing of the energy in the DC link.

Chapter 5:

The final chapter describes the use of robust control technique in the VSC-HVDC technologies. A brief introduction about optimal robust control starts the chapter and the requirements for the HVDC operation are translated in the robust control framework by means of weight functions. The uncertainty models of each of the control loops presented in the converters, for both operation modes, are illustrated. The time domain results provide the necessary proves for the improvements in the dynamic response for the augmented controllers.

The conclusions are presented in the end of the document summarising the outcomes and highlighting some significances. The possibilities of future work are also listed.

In the following one can find three appendices. The first one show results which are related with the model validation of the small signal model analysis built in the chapter 4. The second appendix gives a introductory background to the study of linear system uncertainties, optimal robust control description and overview of μ-synthesis. The last chapter illustrates the PSCAD/EMTDC model built for time domain simulation.

CHAPTER 1

VSC-HVDC Overview

As consequence of the penetration of renewable energy, mainly in the market of wind, the High Voltage Direct Current (HVDC) transmission system appears as the most cost/effective solution for some applications. First applied in connecting high distance in land electric grids, nowadays HVDC technology has become more and more attractive due to integration challenges when considering high penetration of wind energy, for example.

The following chapter presents an overview of the HVDC technology and its application in wind energy. The two main technologies are presented and the further description of the VSC based one is emphasized. The converter topologies are exposed and the main applications, trends and challenges of such devices are cited and referenced.

1.1 HVDC Technologies

In the high voltage DC systems, the principle of transmission relies on two main technologies: the thyristor-based line commutated converters (LCC-HVDC) or voltage source-based converter (VSC-HVDC).

For the LCC case, the converter topology based on thyristors offers the highest cost benefit compared with the fully controlled VSC technique for high power ratings. The increase in the power ratings is indeed a limitation for the VSC topologies. Losses are still smaller in the LCC case. On the other hand, the high susceptibility to AC network disturbances is its main troublesome [1, 2]. Considering to commutation failures, the converter can be temporally disabled or even permanently shut-off. Such situation can even disconnect the entire HVDC system from the AC grids.

Pointing the main limitation of power electronics switching devices, the constraints in voltage levels and processed power include bounds to the usage of such kind of topologies for high power high voltage applications. As no direct measurable benefit, the full controllability of such kind of converter is highly suitable for the current status of AC transmission systems due to the strict requirements

established by the transmission operators in many countries.

As an overall comparison, table 1.1 summarizes the main characteristics of each of the DC transmission techniques.

	LCC	**VSC**
Converter Type	Current-Sourced	Voltage-Sourced
Switch Technology	Thyristor	Transistor (IGBT, GTO, etc)
Switch Voltage Polarity Withstand	Voltage	Current
Power Direction Changeable Variable	Voltage Polarity	Current Direction
Storage Element	Inductively	Capacitively
Semiconductor Control Action	ON	ON and OFF
Turn-off Control Source	External Circuit	Independent
Power Capability	High	Lower
Overload Capability	Good	Weak
AC System Requirements	Strong Grid ($SCR \geq 3$)	Weak or Strong (SCR not critical)
Black Start Capability	No (External Circuit Needs)	Yes
Harmonic Filter Size	Large	Small
Reactive Power Control	Coarser	Finer
Losses	Lower ($\cong 0.75\%$)	Higher ($\cong 1.1\%$)
Cost	Lower	Higher (about 10-15%)
Reliability	Higher	Lower
Technology Maturity	Mature	Less Mature
Cable Requirements	MI	XLPE
Converter Transformer	Specily Built	Conventional

Table 1.1: *LCC and VSC comparison for HVDC appplication.*
Source: Alstom Grid - Introduction to HVDC LCC and VSC - Comparison by Dr. Radnya A. Mukhedkar.

Even still presenting a niche of applications, the LCC-based HVDC is not considered in further analysis, since for offshore wind application, the VSC-HVDC technology presents more suitability. Additionally, the drawback presented by the classical HVDC concerning DC grid possibilities restrict its usage in multiterminal cases. More information with respect LCC converter and its application in HVDC transmission systems can be found in the literature by [3, 4, 5, 6].

The VSC-HVDC technology is the main concern by them. In the VSC-HVDC systems, the concept relies on the switching device developments and new converter topologies.

1.2 Switching Devices

Initially developed for machine drive applications, voltage source converters have been applied in high power and high voltage systems as a result of developments in the increase in power ratings of semiconductors. The first VSC-HVDC transmission in the history dates March, 10^{th} of 1997, when the DC line between Hellsjön and Grängesberg in the Hellsjön Project was energized.

The seek of new technologies for semiconductor devices brought two main types of high-power semiconductor devices: the thyristor-based (current switched) devices, which includes SCR, GTO, and IGCT (or GCT), and the transistor-based (voltage switched) devices, such as IGBT and IEGT [7]. Table 1.2 shows a comparison among the power devices and their characteristics.

	GTO	IGBT LV	IGBT MV	IGCT	SGCT	IEGT
AC/DC Convertion	✓	✓	✓	✓	✓	✓
CSC	✓				✓	
VSC	✓	✓	✓	✓		✓
Efficiency	Low	High	High	Medium	Medium	High
Gate Control	Current	Voltage	Voltage	Current	Current	Voltage
Gate Current	0.4-1kA	0.1A	≤1A	4kA	4kA	¡1.5A
Gate Complexity	High	Low	Low	High	High	Low
Voltage Rating	High	to 1.2kV	4.5kV	to 6kV	6kV	4.5kV
Current Rating	1kA	1kA	to 1.2kA	4kA	5kA	to 4kA
Switching Losses	High	Low	Low	Medium	Medium	Low
Snubber Parts	Many	Low	None	None	None	Low
Switching Speed	Low	Very High	High	Medium	Medium	High
Mounting	Press-Pack	Single Side	Single Side	Press-Pack	Press-Pack	Press-Pack Single Side

Table 1.2: *Driver power device application comparison.*
Source: GE Toshiba Automation Systems - Medium Voltage AC Drive Topology and Medium Voltage AC Drive Topology.

From the switching device characteristics (tale 1.2), the evolution of the devices lead mainly to reduce power losses, simplify gate drive circuits, as well as increase the switching speed, the reliability and finally the cost [8].

Figure 1.1 shows the relationship between typical voltage and power ratings for different converter applications that available in the market or applied in project

from industrial fields.

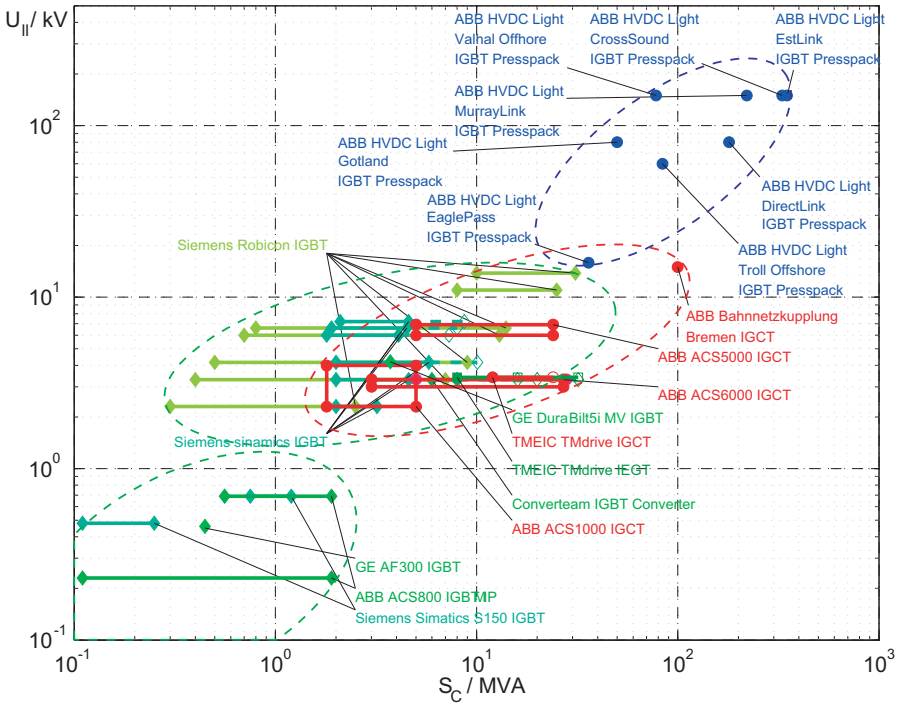

Figure 1.1: *Application of voltage source converters based on switching device ratings in the maket.*
Source: Automatisierte messtechnische Charakterisierung von 10kV Integrierten Gate-kommutierten Thyristoren (IGCTs) by Sven Tschirley (Elektrotechnik und Informatik der Technischen Universität Berlin - Ph.D. Thesis).

1.3 Converter Topologies

The suitability of VSC-HVDC for grid connection application became possible, as mentioned before, due to the development of power electronics. Those converters when connected to the AC grids are able to operate with less sensitiveness to the strength of those grids and also provide fast and decoupled control of active and reactive power [9].

This operating mode is in behalf of the high switching frequency capability of power electronic converters. Concerning the rise in the switching frequency, the losses in the semiconductor devices also increase and determine the higher contribution in the total loss level of the converter stations. Such losses are one of the most challenging issues to deal with application for VSC-HVDC high power converter [10].

In one hand, the development of semiconductor switched devices contributed to the scenario (see table 1.2). The second party is related with the advances of

new converter topologies and their building technologies.

In terms of topologies, three main families of converters can be selected: two level converters, multi-level converters and modular multilevel converters [8]. For applications of HVDC transmission, three main topologies, one from each of the families, became the most popular ones: the two-level bridge (figure 1.2(a)), the three-level NPC [11] (figure 1.2(b)) and the modular multilevel converter [12] (figure 1.2(d)).

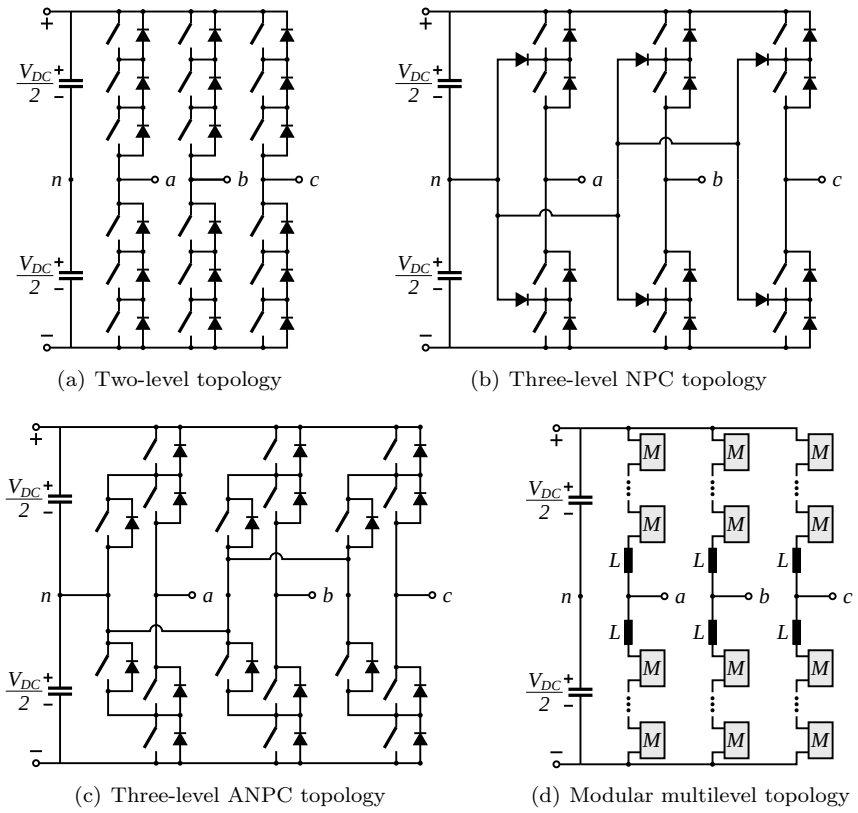

(a) Two-level topology

(b) Three-level NPC topology

(c) Three-level ANPC topology

(d) Modular multilevel topology

Figure 1.2: *VSC-HVDC converter topologies.*

The two-level converter from figure 1.2(a) was the first topology of voltage source converters applied for DC transmission. It is a well known structure since its circuitry design, modulation and control are solidly established. The series connection of switching devices are its main concern, in order to allow high voltages in the DC link. For this purpose, the gate drivers require high complexity to provide synchronization during the turn-on and turn-off commands and avoiding overvoltages applied on the semiconductors [13]. Another obstacle for such kind of topology in high power application is the relationship between processed power and switching frequency. This limitation narrows the power bounds around 400 MW to the switching frequencies not higher than 2 kHz.

The NPC converter came as a solution to increase the power versus frequency limitation of the two-level one. For each switching device, the voltage stresses supported by them is divided by two in a three-level topology. However, the loss distribution among all the switches is not homogeneous. Some semiconductors present more problems with heat dissipation than others which brings some challenges regarding cooling mechanisms. By then, an active clamping structure (ANPC) can diminish such behaviour. The ANPC topology is presented in figure 1.2(c). The balancing of the DC capacitor voltages is a troublesome for NPC as well as in ANPC. Their control requires finer strategies and its operation in HVDC applications can become misled [14, 15]. This is another aggravating aspect when the number of levels increase, since more the number of levels, more DC capacitor balancing controllers are required.

The modular multilevel converter is the state-of-art in converter topologies for high power application. Since it appeared, the MMC converter has attracted interest from academia [16, 17, 18] as well as it appears to emerge as the most tempting topology for HVDC converter adopted by companies [19, 20, 21, 22, 23].

Named as HVDC Plus®, HVDC Light® and HVDC MAXSine®; labels for HVDC products from three main companies in the market, Siemens, ABB and Alstom, respectively; the particularities among all the solutions are in the control strategies and converter modules. For control techniques, further chapters will illustrate the main characteristics in each of the solutions. For the hardware differences, the modules for the three of providers are illustrated in figure 1.3.

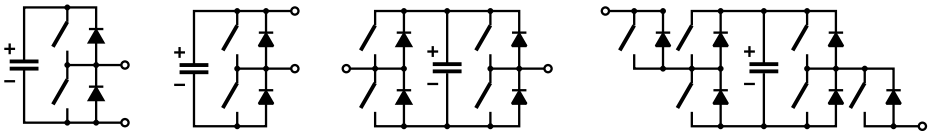

(a) Siemens (b) ABB (c) Alstom (d) Alstom (hybrid)

Figure 1.3: *Modular multilevel converter module topologies.*

Siemens and ABB, figures 1.3(a) and 1.3(b) respectively, have modules with half-bridge type, just the connection among the different modules of the structure is changed. For the Alstom solution, the use of full bridges allows the DC grid faults control with the disadvantages of having higher losses due to the higher number of switching elements (figure 1.3(c)). In order to overtake this disadvantage, a hybrid solution, using both modular and series connected devices was proposed (figure 1.3(d)).

1.4 Applications

The significant impact of the penetration of power electronics in the high power market has shown the cost effective opportunities for high voltage transmission system. DC transmission applications envisage the range from the growing market of renew ables to the low voltage distribution and storage technologies.

From the beginning stages, VSC-HVDC technologies were applied mainly for transmission of bulk power transmission as well as the interconnection of asynchronous networks. With the energy market deregulation and the increase of requirements demanded by the power system operators services for the AC grids, such as voltage and frequency support, low voltage fault-right through (LVFRT) capability, resonant frequency damping and fast dynamics are also becoming needs requested by such systems.

Emerging applications can be listed in some key areas and listed as the following [10]:

- Connection of remote loads;
- Power infeed in urban areas;
- Connection with distributed generation;
- Connection with offshore generation;
- Deep-sea crossing interconnection;
- Multiterminal systems;
- Linking medium frequency networks;
- Low voltge DC for power distribution in industrial applications;
- Storage system interconnections.

1.5 Summary

The increasing amount of VSC-HVDC projects in the world reflects the energy market trend in integrating high power converters and DC transmission.

The key benefits and the competitive advantages presented previously can justify such tendency. The niche of application for the mentioned converters is broad, however, the offshore wind energy is the application which leads the amount of investments. Table 1.3 summarizes some of recent VSC-HVDC projects worldwide and relates the applications.

Project	Year	Power	DC Link	Topology	Manufacture	Application
Hellsjön, Sweden	1997	3 MVA	±10 kV	Two-Level	ABB	Trial operation
Gotland HVDC, Sweden	1999	50 MVA	±80 kV	Two-Level	ABB	Wind power and voltage support
Eagle Pass, USA	2000	36 MVA	±15.9 kV	NPC	ABB	Asynchronous connection for trading and voltage control
Tjæreborg, Denmark	2000	8 MVA	±9 KV	Two-Level	ABB	Demonstration project for wind power
Directlink, Australia	2000	180 MVA	±80 KV	Two-Level	ABB	Asyncronous connection
Murraylink, Australia	2002	220 MVA	±150 kV	ANPC	ABB	Controlled connection for trading
Cross Sound, USA	2002	330 MVA	±50 kV	ANPC	ABB	Power exchange
Troll-A, Norway	2005	88 MVA	±60 kV	Two-Level	ABB	Offshore oil and gas application
Estlink, Finland-Stonia	2006	350 MVA	±150 kV	Two-Level	ABB	Asynchronous connection and sea crossing
BorWin1, Germany	2009	400 MVA	±150 kV	Two-Level	ABB	Offshore wind and asynchronous connection (First offshore VSC-HVDC link)
Caprivi, Namibia	2009	300 MVA	350 kV	Two-Level	ABB	Weak grid connection and overhead lines tansmission. First bipole VSC-HVDC with overhead lines
Valhall, Norway	2009	78 MVA	150 kV	Two-Level	ABB	Offshore oil and gas application
Trans Bay Cable	2010	700 MVA	±200 kV	MMC	Siemens	Submarine cable connection
EirGrid, Ireland and UK	2012	500 MVA	±200 kV	Two-Level	ABB	Submarine cable, black start, reactive power support, controlability
DolWin1, Germany	2013	800 MVA	±320 kV	MMC	ABB	Length of land and sea cables
BorWin2, Germany	2013	800 MVA	300 kV	MMC	Siemens	Offshore wind
HelWin1, Germany	2013	576 MVA	259 kV	MMC	Siemens	Offshore wind
Skagerrak, Norway	2014	700 MVA	500 kV	MMC	ABB	Length of sea crossing, asynchronous link, power quality features

†- No available information.

Table 1.3: *Worldwide VSC-HVDC projects summary.*

Project	Year	Power	DC Link	Topology	Manufacture	Application
Mackinac, USA	2014	200 MW	70 kV	Two-Level	ABB	Islanded operation, voltage stability, power flow control
INELFE, France-Spain	2014	2x1000 MVA	±320 kV	MMC	Siemens	Underground cable
SylWin1, Germany	2014	864 MVA	±320 kV	MMC	Siemens	Offshore wind
Svenska Kraftnät, Sweden	2014	1440 MVA		MMC	Alstom	Power flow control
Tres Amigas	2014	750 MVA		MMC	Alstom	Energy hub
NordBalt, Lithuania-Sweden	2015	700 MVA	±500 kV	MMC	ABB	Length of sea crossing, asynchronous networks
DolWin2	2015	900 MVA	±320 kV	MMC	ABB	Length of land, sea cables, offshore wind
Troll A, Norway	2015	100 MVA	±60 kV	Two-Level	ABB	Long submarine cable distance, compactness of converter
HelWin 2, Germany	2015	690 MVA	±320 kV	MMC	Siemens	Offshore wind

†- No available information.

Table 1.4: *Worldwide VSC-HVDC projects summary - Continuation.*

CHAPTER 2

Introduction to Multiterminal HVDC Systems

The applicability of DC transmission system and voltage source converters in the modern power systems present their advantages and suitability, similarly as it was outlined in previous chapter. For future trends, the interconnection of multiple VSC-HVDC stations is an envisage and has a backbone to the increase in the number of offshore wind farms which have been built and are planned for a near future (see tables 1.3 and 1.4).

The following text summarizes the concepts and challenges in Multiterminal VSC-HVDC (MTDC) technology. The principle of operation and possible layout configuration are firstly explored. Challenges on the role of MTDC systems such as protection and control issues are itemized lately. Final remarks regarding economic obstacles and prospects for supergrid concept are also briefly analysed.

2.1 General Description

The effects of the penetration of renewable energy has been felt by the European power grid [2]. As main contributor for the modern energy market, the wind energy has been moving to offshore areas. The distances related with seaward land application, absence of reactive power compensation and size minimization of offshore platforms, make the HVDC more competitive than the classical high voltage AC (HVAC) solutions.

Considering mainly the high penetration level of renewables, the connection of those geographically remote energy resources, located far from shore, their limited correlation and their widely disperse distribution, the needs for the DC supergrids become potentialised.

The idea of supergrids is not new. The first proposal dates from 1930s, when, in the US, the creation of a long distance transmission network appeared. The project would drive the energy from the hydropowers linking the Pacific Northwest

to the consumption areas located at the Southern California [24].

Meanwhile, this concept has become more and more mature by means of advances in the electronics, control and cable technologies and, by 2001, its intends for the European unified power grid was launched. At that time, the interconnection among the existent power plants and the new generation from renewables from wind in the north Europe and photovoltaic resources from South of Europe and Northern Africa was introduced. An extra benefit in balancing power appears in the different time zones between east and west and the interconnected system can take advantages by strengthening the grid. Figure 2.1 illustrates the European Supergrid map which integrates all the main energy resources from Europe by means of DC supergrid.

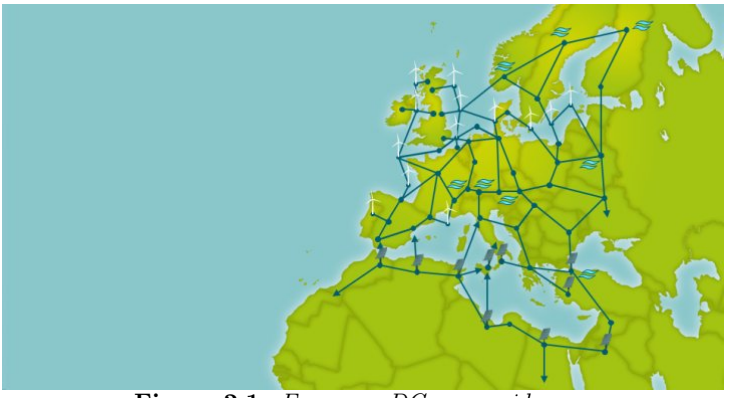

Figure 2.1: *European DC supergrid map.*
Source: Friends of the supergrid.
Web: http://www.friendsofthesupergrid.eu/supergrid.aspx

2.2 Configurations

A multiterminal DC connection can be viewed as a link among three or more HVDC converters. For the LCC based type, the control of parallel converter becomes more troublesome, since the polarity of the DC voltage must change for power flow reversal operation. This situation points the VSC-based HVDC as the most appropriate technology for supergrids concept for HVDC applications.

For the layout configuration viewpoint, the connection of converter for DC grids can vary in number of interconnections and number of converters stations, depending on the dispersion of the load centers and generation zones. Though, one can group the layout in five main structures[25, 26]:

- Multiterminal with tappings;
- Grid with independent DC lines;
- Meshed DC grid;

- DC grid with controllable devices;
- AC system connected by DC connections.

The first configuration (figure 2.2(b)) is the most simple multiterminal system. It is a radial connection and no redundancies are available. Topology could be used as a very practical alternative for an AC connection. The proposed SouthWest Link (see tables 1.3 and1.4) is planed to be a multiterminal connection with radial configuration.

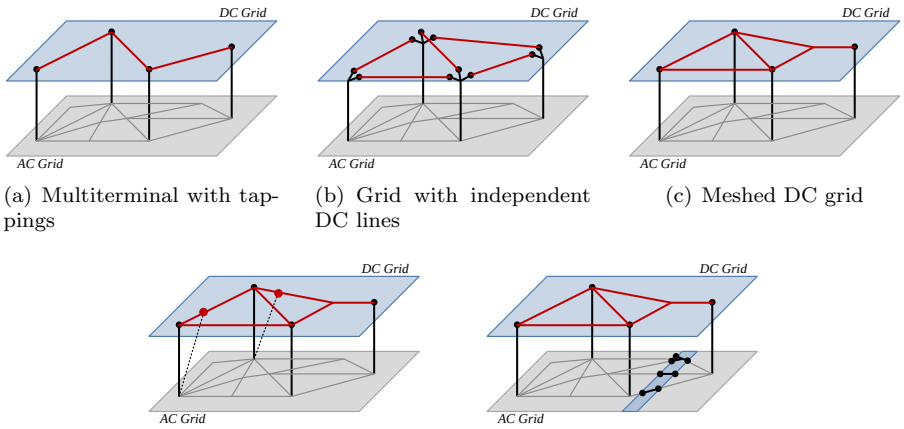

(a) Multiterminal with tappings

(b) Grid with independent DC lines

(c) Meshed DC grid

(d) DC grid with controllable devices

(e) ACSystemConnectedbyDCConnections

Figure 2.2: *Different DC grid topologies for potential supergrid application.*

Figure 2.2(b) illustrates where all the buses are AC type. The AC lines were replaced by DC with a point-to-point connection with two converter stations promoting fully controllability of the power flow. This layout can operate with hybrid systems where LCC merges with VSC technology. The main advantage in such configuration is based on the fact that the AC protection system can be incorporated. The number of converter is a troublesome in the mentioned interconnection.

The following topology, the third (figure 2.2(c)), is a meshed DC grid. The links can have or not have the presence of a converter station. It is the configuration with the closest similarities from the classical AC systems. The interconnected network supports redundancies since multiple paths are available. The reliability and flexibility of meshed grids promote this kind of layout. However, the protection equipments are still not mature and is a limiting factor for its development.

The composition among the meshed connection with additional converters (dotted lines connected by red dots) forms the layout presented in figure 2.2(d). Such devices can be connected by the AC side and series connected in the DC link. In one station, the combination can present LCC and VSC topologies at the same time. With this merge, the power flow control can still be guaranteed

but the losses and cost of the total converter station can be reduced. DC-to-DC converter can also be included as candidate. However, for high power and high voltage application, the cost of the devices is still the main issue.

The last configuration (figure 2.2(e)) represents the connection of AC grids by means of DC. This configuration splits the AC systems in smaller segments. Such approach can limit the fault propagation and cascading blackouts as well as power exchange among decoupled systems. It means that the operation of the AC systems can be independently accomplished with mitigation of the propagating disturbances from one AC system to the others.

2.3 Challenges

The advantage in promoting high integration level of energy resources, as illustrated in figure 2.1, makes the multiterminal VSC-HVDC technology very attractive by its efficiency. However, as a consequence of its youthfulness, several challenges related to technical as well as economic issues are still emerging. Some examples of the drawbacks which the multiterminal VSC-HVDC technologies affront nowadays are listed as follows:

2.3.1 Protection

One of the main obstacles in the growth of multiterminal DC systems is related to the DC overcurrent protection. The problem in DC networks lies in the absence of current zero crossing combined with the low system impedance increase the complexity of the DC breaker elements.

In the case of point-to-point connection, the operation of voltage source converters during DC faults can be accomplished by the coordination of AC circuit breakers and chopper resistors presented in the DC link [27].

Nonetheless, for MTDC application (mainly in meshed DC grids), this technique meets its limitations [28] which is the low system impedance in the DC. In this scenario, the development of solid state DC circuit breakers [29] and VSC topologies which enables the fault handling capability [30] are envisaged.

The necessity of fast and reliable DC circuit breaker for DC fault clearance in DC grid applications brought the appeal in development of the *Modular Hybrid IGBT DC Breaker*. Simplified circuit diagram is presented in figure 2.3.

During normal operation, the DC current flows through the bypass. At the moment of the fault, the auxiliary DC breaker starts switching and modulating the DC current. At the same time, the fast disconnecter is opened and the main DC breaker extinguishes the current. As a final stage of the fault clearance procedure, the mechanical switch isolates the primary voltage across the main DC breaker.

The claims in such topologies lies in the fact that the losses of the hybrid topology of the modular DC breaker are reduced to the equivalent losses of a

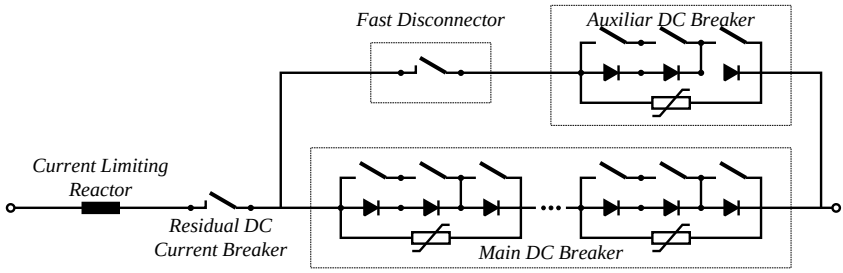

Figure 2.3: *Simplified circuit diagram of the modular hybrid IGBT DC breaker [29].*

pure semiconductor breaker and the opening time required by such circuitry is on the range of 2 ms.

The second solution presented by fault handling in the meshed DC networks integrates the modular multilevel converter topologies were briefly exposed in the previous chapter (figure 1.2(d)).

Considering the combination of the low loss ratings and modularity of modular multilevel converters, the hybrid solution makes use of hybrid modules to assemble the converter cells. In this topology, series connected IGBT devices are assembled with full bridge modules as illustrated in figure 1.3(d). During the faulted period, the proper control of the stack hybrid cells can change the polarity of the entire DC arm voltages and, by this means, control the flow of the converter DC current.

2.3.2 Communication

The communication requirements in a DC grid is still an opened issue, since it is related with the size, control architecture and measurement units of the network. Depending on the size and the number of interconnection, the communication links can require very complex structures.

Three main communication levels are considered. The first one is related to the reference power set points. For this purpose, the ratings in the communication speeds can be relatively slow, requiring lower bandwidth.

The second stage of communication level integrates the dynamic control of power systems for stability improvement such as power oscillation damping among the partners in the DC grid. The requirements for this application demands coordination and high reliability in the communication links.

The protection schemes will rely in the communication in some applications. For these conditions, very fast coordination among the converter stations are necessary. Higher bandwidth is needed due to the fact the transit periods for protection issues are in the range of ms.

2.3.3 Grounding

During a pole to ground fault type, the surge currents pass through ground. High or low impedance grounding schemes can be applied for reducing ground currents and assisting the protection scheme increasing the clearance time.

On the other hand, depending on the choice of the ground circuitry, while the ground impedance is increased (as well the clearance time requirements) the pole voltage is boosted. With this increase, the converter voltage ratings and, as direct consequence, the final price of the converter station.

2.3.4 Operation

In case of a DC supergrid, more than one Transmission System Operator (TSO) is in charge of the control and coordination of the system. In the connection with many areas, the deregulated DC transmission system will require different types of operation: coordinated operation, independent operation and integrated operation [31].

In the coordinated control, as the same as it is presented by large multi-TSO power systems, the need for a central MTDC TSO is essential. Having the security assessment as a main purpose, the central controller defines the operation of the MTDC system based in the agreed TSO interests and benefits.

Ancillary services, such as primary frequency control, are handled. Due to the interconnected scheme, the sharing of primary reserves and its control on time assures that different reserves resources and their time period are satisfactory for all the partners.

For short-term power unbalances, which is applied in areas with limited reserves resources, the HVDC TSO can operate the DC system with the aim of smoothing the changes in the power flow. The dynamic impact, resulting from the fast changes in the interconnected areas, can be handled.

By considering the independent operation, the HVDC TSO handles the converter and line loadings according to its revenue maximisation. The operation is similar to the generation policies where the rewards are counted by providing reserves where they are more profitable, based in connection and economic rules.

Compared with the coordinated condition, this operation mode allows more deviations with regards to power deviations.

The operation mode considers the integrated operation of the DC system. It is assumed that the TSOs of some areas can manage the converter stations, the loading of lines and cables. In this situation, the TSOs are able to support their own AC systems as well as support the operational costs. In this case, the agreements in negotiating ancillary services among partners rely on technical flexibility and in the policies of interdependencies among the many partners.

2.3.5 Control

Considering the MTDC control of power, the DC voltage compensation plays an important role in promoting the full flexibility of the MTDC in the sharing of power. Four main control strategies have been studied as the most suitable candidates for multiterminal VSC-HVDC transmission systems [32, 33, 34].

- Voltage droop
- Ratio control
- Priority control
- Voltage margin method

2.3.5.1 Voltage Droop

Similarly to the frequency control in AC systems, where the dependency of the load and frequency is used as an effective adjust the generator power of synchronous machines, in MTDC applications, the droop control regulates the DC voltage according to the receiving power for balancing enforcement.

The maximum and minimum values for the DC voltage are set and, depending on the level of the DC current/power, the set point of the converter voltage reference can drop or increase according to the slope θ of the droop curve. The operation of the converter as rectifier or inverter is dependent of the DC voltage level as shown in figure 2.4.

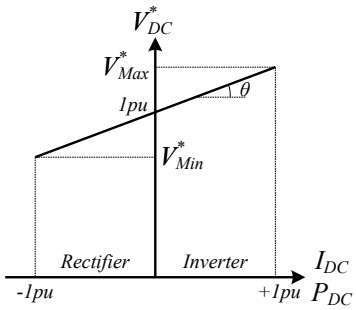

Figure 2.4: *Example of DC droop curve for multiterminal DC applications.*

2.3.5.2 Ratio Control

The ratio control is a special case of droop control where the DC voltage droop factors are applied just in the inverter end stations. The receiving end station is able to share the power from the sending end terminals depending on the defined relationship among the droop factor applied in the voltage controllers. Figure 2.5 illustrates an example of a droop curve for the ratio control scheme.

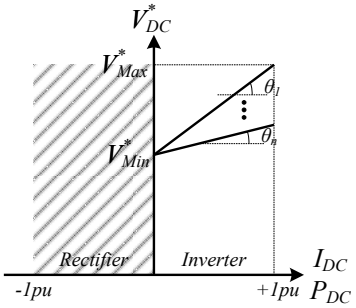

Figure 2.5: *Example of DC droop curve for multiterminal DC applications using ratio control.*

2.3.5.3 Priority Control

In this control mode, one of the converters in the DC link has priority in the power transfer. This terminal has the direct DC voltage control and, as soon as the processed power reaches the set point, established by the operation rules, the DC voltage regulator has no longer capability for maintain the DC voltage balance which will increase as a consequence of increasing in power. Thus, the other terminals in the link start to process power once the converter in which the priority was included reached its limits. The curve presented in figure 2.6 illustrates an example of a priority control droop curve.

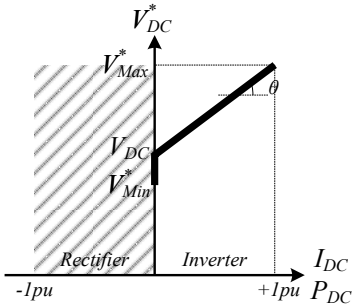

Figure 2.6: *Example of DC droop curve for multiterminal DC applications using priority control.*

2.3.5.4 Voltage Margin

The voltage margin method combines the power and direct voltage control modes. A voltage margin is given to each of the converter connected to the DC grid. This margin is defined as a maximum and minimum values in which range the DC bus voltage reference can deviate. By changing the limits of the DC voltage regulators according to the power set point, the maximum and minimum values of the DC voltage compensation defines the operation of the converter as rectifier or inverter modes. Figure 2.7 gives an example for a system that adopts

the voltage margin method.

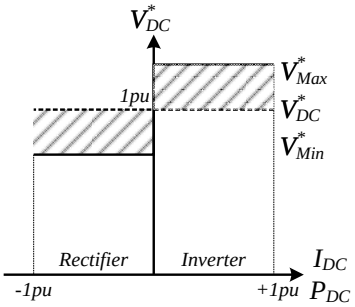

Figure 2.7: *Example of voltage margin curve for multiterminal DC applications.*

2.3.6 Standardisation

As an immature but with high potential technology, multiterminal VSC-HVDC does not experience, nowadays, any effort in standardisation such as DC voltage levels and compatibility, as already presented in AC power systems. Different manufacturers are today in the market, and with the prospects in growing and matureness, more competition and parties can appear in the increasing scenario.

At this moment, no real standards for DC voltage levels, for example, are in operation. From table 1.3, it is possible to verify that there is no accordance in the DC bus voltage levels among the released and the new projects to be commissioned. This first issue can bring many challenges in the future prospects in interconnecting all those established systems.

The different converter topologies, protection schemes, operation and control strategies adopted by the manufactures can interact. The effects in one into the other can be unsuitable when the prospects in integrating all those system in a real meshed MTDC power system.

2.3.7 Economics

The technical benefits of having an interconnecting DC system is a clear advertising for MTDC due to lower losses, high distance transmission using cable technologies and power flow control flexibility, mainly considering the market of renewable resources.

In some applications, the HVDC transmission appears as an unique solution for power transmission. One example is the offshore wind application, remotely connected by means of submarine cables. In this case, the AC interconnection becomes costly enough to overtake the high cost off HVDC converter stations.

However, when the use of multiterminal HVDC to reduce the congestion in transmission capacity is taken into account, the necessary investments in build-

ing such infrastructure are nowadays doubtful. The competition with the well established and reliable AC transmission systems and its cost make the supergrid concept unsure. Significant investments are essential and require multiple investors. For such, the positive return and acceptable pay-back time is dubious and undetermined.

2.3.8 Supergrid Foresee

The multiterminal connection of VSC-HVDC transmission system (the pioneer of the supergrid) is a growth but still immature technology. There is no systems at the moment and its commissioning will be predicted to the following years to come. The DC supergrid formed by the interconnection of multiple voltage source converters in a meshed layout is even more futuristic.

Many technical and politic/economic issues are still opened. However, the current developments in the HVDC technologies make the supergrid a possible scenario for the future of transmission power system.

CHAPTER 3

Control Optimisation in Multiterminal VSC-HVDC

THE selected method to control the power flow in multiterminal HVDC is based on DC voltage droop in each of the converter stations in which the DC voltage controllers are enabled. Considering the back-to-back wind generation converter type and AC collector for offshore connection, the droop controls applied in the onshore stations are able to define the appropriate voltage levels for a desired power dispatch. Moreover, using such an approach, it is possible to have more buses in which the DC voltage can be controlled, bringing more flexibility for large DC networks.

This chapter is focused in the design of the droop factors for DC networks and the optimisation methods to select the proper values for the reference set points are introduced. The constrained optimisation scenarios are listed and they are presented in study cases for loss minimisation and two cases involving dispatch maximisation problem.

3.1 Optimisation Objectives

In layman's terms, an optimisation problem consists in finding the best point of a function, considering maximum or minimum conditions, for the set of its feasible solutions. A more restrict issue appears when constraints are included in those conditions, narrowing down, even more, the solution group.

The general mathematical model for such problem is represented by (3.1).

$$\begin{aligned} &\textit{minimise} && f_o(\mathbf{x}) \\ &\textit{subject to} && f_i(\mathbf{x}) \leq 0, \quad i = 1, 2, 3, \ldots, m \end{aligned} \tag{3.1}$$

In (3.1), $\mathbf{x}$ is the optimisation variable (or decision variable) with n components. The function $f_o : \mathbb{R}^n \to \mathbb{R}$, is the objective function, the one in which maximum or minimum requirements are placed. $f_i : \mathbb{R}^n \to \mathbb{R}$ are the m constraints.

Whether the optimum solution of the objective function under the constraints conditions is feasible, this point is specified by $\mathbf{x}^*$ and $f_o(\mathbf{x}^*)$ is the critical point.

Based on the properties of the objective function and its constraints, the complexity in finding the solution $f_o(\mathbf{x}^*)$ can considerably vary. In order to overtake this bottleneck, a solution method for many of the optimisation problems can be released by computer based algorithms where the critical points, when feasible, are numerically obtained. Many of these tools are available today and they differ on the complexity and effectiveness in finding the solution [35].

The method adopted for further development is called interior point. Also known as barrier method, this algorithm, roughly speaking, changes a complex problem summarized by the framework given by (3.1) into a simpler one, just adding a dual function in the objective function such as is written in (3.2).

$$minimise \quad f_o(\mathbf{x}) + \Phi(\mathbf{x}) \tag{3.2}$$

The graphical representation of the dualisation method is shown in figure 3.1, where a modulus function (continuous blue line) is firstly approximated by a second order polynomium (dashed red line) and by a sixth order polynomium (dotted black line).

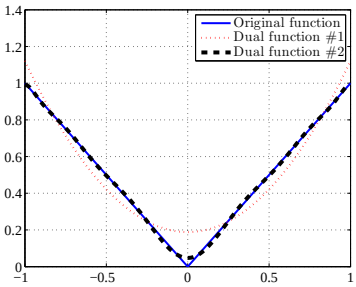

Figure 3.1: *Graphical representation of an optimisation problem dualisation.*

The original objective function $f_o(x)$ is represented by the continuous blue line in figure 3.1. Due to the conner at the origin, no feasible solution can be found, since the derivatives in that point vanish. However, approximating $f_o(x)$ to a second order polynomium (red dotted line), the new function is differentiable. Increasing the the order of polynomium, the new function is represented by the black dashed function in figure 3.1. Higher the order of the polynomium, higher is the accuracy of the approximation.

The objective of the algorithm is, then, to change the value of a parameter of a dual function which is completely differentiable (in the current case, the order of a polynomium that best fits the original objective function). The critical point of such dual function can be found using regular linear optimisation methods like *Newton's Method* or even analytical methods.

For the general problem presented by (3.1), the dualisation is taken by repre-

senting $\Phi(\mathbf{x})$ in (3.1) using the sum of the logarithm of the constraints (3.3).

$$\Phi(\mathbf{x}) = -\frac{1}{t}\sum_{i=1}^{m}\log\left(-f_i(\mathbf{x})\right) \tag{3.3}$$

where t is the changeable parameter. Higher the value of t, closer the dual objective function is to the original one. As an illustrative example, it is possible to verify the variation of the parameter t in a optimisation problem by looking into figure 3.2.

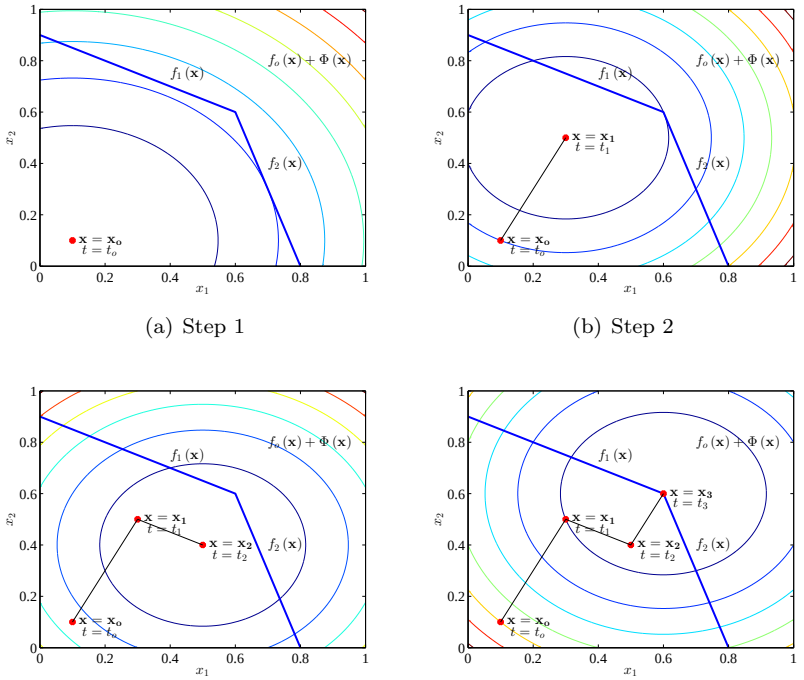

(a) Step 1

(b) Step 2

(c) Step 3

(d) Step 4

Figure 3.2: *Representation of the path taken by the optimum point for variation in the parameter t.*

In the first iteration, an optimum point to the function $f_o(\mathbf{x})+\Phi(\mathbf{x})$ is found at $\mathbf{x}=\mathbf{x_o}$ for parameter value $t=t_o$ (figure 3.2(a)).

Second, a new parameter $t=t_1$ is chosen such that $t_1=\mu t_o$, for $\mu>1$. A new optimum point $\mathbf{x}=\mathbf{x_1}$ is found (figure 3.2(b)). The tolerance ϵ is checked by verifying the difference between $\mathbf{x_o}$ and $\mathbf{x_1}$. The same procedure is taken in the steps 3 and 4 (figures 3.2(c) and 3.2(d)). However, in the step 4 the iterative loop stops since the tolerance is achieved. Algorithm 1 summarizes the procedure presented in figure 3.2.

Algorithm 1 Interior point algorithm

Given a initial parameter value $t = t_0$, $\mu > 1$ and tolorence $\epsilon > 0$
repeat
  Compute $\mathbf{x}^*$ which minimises $f_o(\mathbf{x}) + \Phi(\mathbf{x})$
  Update the value of $\mathbf{x}$ by $\mathbf{x} = \mathbf{x}^*$
  Increase the value of t by $t = \mu t$
until $\frac{m}{t} < \epsilon$

3.2 Application of Optimisation in Droop Factor Design: Study Cases

The selection of the droop gains for DC networks by means of optimisation can assess many objectives. Considering the static viewpoint, some of them can be mentioned. The first one is to select the values of the droop controllers in order to decide for appropriate voltage levels, aiming to achieve minimum transmission losses. For the same scenario, quantification of the converter losses can be also included in the model.

Another possible solution can be related with the optimisation in the power delivered to the AC grids connected to the DC transmission system. By doing that, the error in the dispatch can come into picture and can characterize the objective function.

For the determination of droop factors using one of the previous cited scenarios, a general procedure is adopted. However, the test benchmark for evaluation properties consider a DC grid formed by two onshore stations and two offshore stations connected to offshore wind farms as illustrated in figure 3.3.

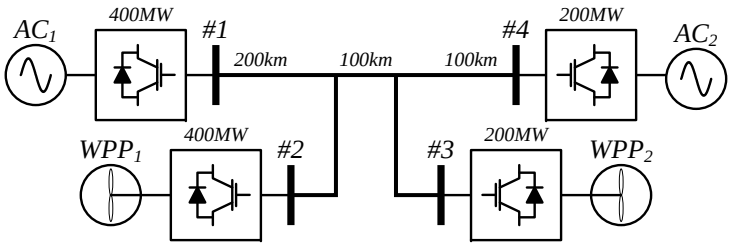

Figure 3.3: *Multiterminal VSC-HVDC benchmark employed in the optimisation analysis.*

Voltage and nominal power for each of the converter stations are summarized by table 3.1.

	1	2	3	4
DC Voltage	$\pm 150kV$	$\pm 150kV$	$\pm 150kV$	$\pm 150kV$
DC Power	$400MW$	$400MW$	$200MW$	$200MW$

Table 3.1: *System nominal parameters.*

Cable lengths and impedance per kilometer are presented in table 3.2

Bus from	Bus to	Distance $[km]$	Impedance $\left[\frac{\Omega}{km}\right]$
1	**2**	200	0.0176
2	**3**	100	0.0366
3	**4**	100	0.0366

Table 3.2: *Cable lengths and impedances.*

Clearly, the power flow in the system from figure 3.3 is driven by the voltage difference among the DC buses. Compared with classical AC connection, the system is more restrictive. In sinusoidal operation, two degrees of freedom are available for power transfer control properties: voltage difference and phase angle. Changing both variables, active and reactive power are transferred from one bus to the other.

However, one degree of freedom is lost in a DC network, which means that only active power is available. This fact can be seen as a simplification for the system load flow calculation and, on the other hand, an increase in the control effort to keep the stability or system performance.

Considering, first of all, the static scenario, the power flow can be analysed. Using the load flow calculation, voltage and power in each of the converter stations can be predicted [36]. As a result, the set points for the converter controllers are set and, indirectly, the droop factors can be derived. At this point, the mentioned set points are calculated using load flow. In the next chapters, the droop factors are going to be analysed since dynamic models are presented and variations are considered.

Two main cases are included in the load flow calculation and each of them are split in two more cases. They are listed as follows:

1. Loss minimisation
   (a) Cable loss minimisation
   (b) Cable and converter loss minimisation
2. Dispatch optimisation
   (a) Dispatch error minimisation
   (b) Power delivery maximisation

In all of the cases, the main core of the load flow is the definition of the objective function in the framework presented in (3.1). The procedure is similar in all the scenarios. Due to that, the methodology is deeply explored in the loss minimisation case and repeated in the other items.

To define the set point values in a DC network such method can be applied in the DC load flow problem. Advantage of this implementation is that none of the buses are treated specially such a slack bus. Besides all the voltage levels in all the buses in the system can be properly chosen since the objective function is optimized and the constrains are satisfied.

3.2.1 Loss Minimisation

3.2.1.1 Cable Loss Minimisation

The problem in minimising the DC transmission losses is the simplest case to be presented. In some real cases, the losses in the system can justify its application [**?**]. Despite the fact that it does not consider some main requirements for the grid, it can be seen as a starting point to build more general strategies. Additionally, this is an evaluation tool to verify the operational aspects of the optimisation.

Considering the test system from figure 3.3, for the load flow analysis the system can be simplified considering just the nodes and branch impedances as illustrated in Figure 3.4.

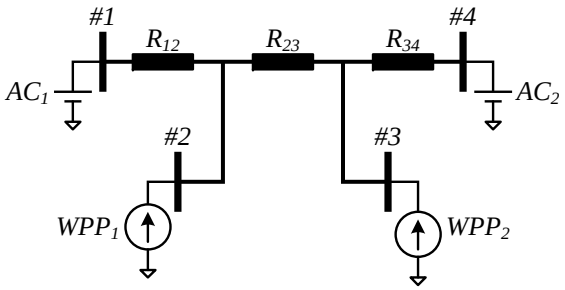

Figure 3.4: *Simplified circuit for DC load flow analysis.*

In figure 3.3, the impedances are represented by cable resistances and two type of buses are considered. The ones where the DC voltage control is enable are represented by voltage sources. The infeed points, which are the HVDC stations where the wind farms are connected, are represented by current sources. The HVDC converter that is in active power mode control can also be represented by this model.

The node voltage are V_1, V_2, V_3 and V_4 and the currents I_{12}, I_{23} and I_{34} flow thought the terminals of the resistors R_{12}, R_{23} and R_{34} driven by the node voltage differences. The currents in each of the branches are written as follow:

$$I_{12} = \frac{V_1 - V_2}{R_{12}} \tag{3.4}$$

$$I_{23} = \frac{V_2 - V_3}{R_{23}} \tag{3.5}$$

$$I_{34} = \frac{V_3 - V_4}{R_{34}} \tag{3.6}$$

Using vectorial notation, the currents can be grouped as $\mathbf{i} = [I_{12} I_{23} I_{34}]^T$. For the case of loss optimisation, the cost function $J(.)$ can be written as presented

in (3.7).

$$J\left(\mathbf{v}_{DC}\right) \quad = \quad \mathbf{v}_{DC}^{T} \cdot \mathbf{Y} \cdot \mathbf{v}_{DC} \tag{3.7}$$

where $\mathbf{v}_{DC}$ is the DC voltage vector and its elements are the voltages at each station in the network and $\mathbf{Y}$ is the admittance matrix formed by the branch conductances of the DC cables. The superscript $.^{T}$ indicates the vector transpose operation.

The admittance matrix can be written following (3.8).

$$\mathbf{Y}_{DC,ij} \quad = \quad \begin{cases} -y_{DC,ij} & \text{if } i \neq j \\ \sum_{j=1}^{N} y_{DC,ij} & \text{if } i = j \end{cases} \tag{3.8}$$

where $y_{DC,ij}$ is the conductance between the buses i and j and N is the number of buses. Due to the way in which the admittance matrix is built, it is possible to assure that $\mathbf{Y}_{DC}$ is symmetric.

As a constrained optimisation problem, since the network equation must be satisfied, (3.9) can be written.

$$g\left(\mathbf{v}_{DC}, \mathbf{p}_{DC}\right) \quad = \quad \mathbf{Y} \cdot \mathbf{v}_{DC} + \left(diag\left(\mathbf{v}_{DC}\right)\right)^{-1} \cdot \mathbf{p}_{DC} = 0 \tag{3.9}$$

where $\mathbf{p}_{DC}$ is the power processed by each bus and $diag\left(\mathbf{v}_{DC}\right)$ the diagonal matrix formed by the values for the DC voltages. This power vector contains the constant components of power, that are generated by the wind farms $\mathbf{p}_{DC_{WPP}}$, and the ones $\mathbf{p}_{DC_{D}}$ which are going to be calculated during the load flow analysis and delivered to the AC grids.

It should also be considered the physical limitation of the system into the vector $\mathbf{v}_{DC}$ by means of considering the voltage boundaries, which means write (3.10).

$$\mathbf{v}_{DC}^{min} \quad \leq \quad \mathbf{v}_{DC} \quad \leq \quad \mathbf{v}_{DC}^{max} \tag{3.10}$$

The power limits should also be considered as constraints. Two main purposes are related to this topic. The first one is the limitation of the the DC cables and the second case is related with converter ratings. It is going to be considered that the power ratings of the cables are the same presented by the converters in which the power is delivered to the grid. So, similar to (3.10), the power vector limits are written according to (3.11).

$$\mathbf{p}_{DC}^{min} \quad \leq \quad \mathbf{p}_{DC} \quad \leq \quad \mathbf{p}_{DC}^{max} \tag{3.11}$$

The power limits can be set differently from the system limits. The power bounds are going to drive the system to the power control mode during the operation. Moreover, it is possible to the converter operates in a bidirectional mode meaning that the onshore station is injecting power in the grid. In this condition, the same limitation for the bounds can be applied, however the signal of the power vector elements must be changed from positive to negative.

Taking into account, first of all, the optimal voltage vector $\mathbf{v}^*_{DC}$, the optimal sharing condition distribution $\mathbf{p}^*_{DC_D}$ is inside the set formed by cost function and constraints as showed above. The following Lagrangian function can be expressed.

$$\mathscr{L}\left(\mathbf{v}_{DC}, \mathbf{p}_{DC_D}, \boldsymbol{\lambda}\right) = J\left(\mathbf{v}_{DC}\right) + g\left(\mathbf{v}_{DC}, \mathbf{p}_{DC}\right) \cdot \boldsymbol{\lambda}^T \tag{3.12}$$

and $\boldsymbol{\lambda}$ are the Lagrangian multipliers for the constrained optimisation problem given by (3.12).

Since the seeking for candidates for critical points are inside the bounded region, where the partial derivatives of (3.12) can be computed, the first order-necessary optimability conditions are (3.13), (3.14) and (3.15).

$$\frac{\partial \mathscr{L}\left(\mathbf{v}_{DC}, \mathbf{p}_{DC_D}, \boldsymbol{\lambda}\right)}{\partial \mathbf{v}_{DC}} = 0 \tag{3.13}$$

$$\frac{\partial \mathscr{L}\left(\mathbf{v}_{DC}, \mathbf{p}_{DC_D}, \boldsymbol{\lambda}\right)}{\partial \mathbf{p}_{DC_D}} = 0 \tag{3.14}$$

$$\frac{\partial \mathscr{L}\left(\mathbf{v}_{DC}, \mathbf{p}_{DC_D}, \boldsymbol{\lambda}\right)}{\partial \boldsymbol{\lambda}} = 0 \tag{3.15}$$

For this propose, just the components $\mathbf{p}_{DC_D}$ are taken into account because the power from the wind farm is considered to be constant.

Deriving (3.13), (3.14) and (3.15), it is possible to obtain:

$$2 \cdot \mathbf{Y}_{DC} \cdot \mathbf{v}_{DC} - \left(diag\left(v_{DC}\right)\right)^{-2} \cdot \mathbf{p}_{DC} \cdot \boldsymbol{\lambda}^T = 0 \tag{3.16}$$

$$\left(diag\left(v_{DC}\right)\right)^{-1} \cdot \boldsymbol{\lambda} = 0 \tag{3.17}$$

$$\left(diag\left(v_{DC}\right)\right)^{-1} \cdot \mathbf{p}_{DC} = 0 \tag{3.18}$$

Considering what (3.16), (3.17) and (3.18) show, the interior region belonging to the constrained and bounded problem given by (3.12) does not contain the minimum for the problem since the equations converge to conditions where the voltages are all zero. Assuming that (3.7) is convex, the minimum presented by (3.16), (3.17) and (3.18) shows a unique global solution. Figure 3.5(a) illustrates this problem.

With this conclusion in hands, there are more two conditions where it is possible to find the solution: the boundaries and the corners. Considering a general case where the vector variable is $\mathbf{x}$, when the boarders (inequality constraints) of the domain are taken into account, the derivatives vanish due to discontinuities and the equations given by (3.12) are not valid anymore. It means that the global critical point $\mathbf{x}^*$ does not belong to the bounded region and a local critical point $\mathbf{x}^*_{Local}$ is found instead. The algorithm starts by seeking for critical points from the initial condition $\mathbf{x}_o$ and the boundaries, given by inequality constraints. Figure 3.5(b) brings the description of evaluating optimisation problems in bounded regions.

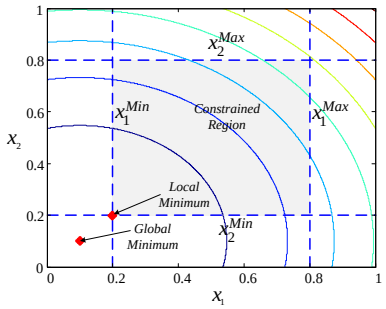

(a) Simplified diagram to compare the influence of constraints in a optimisation problem.

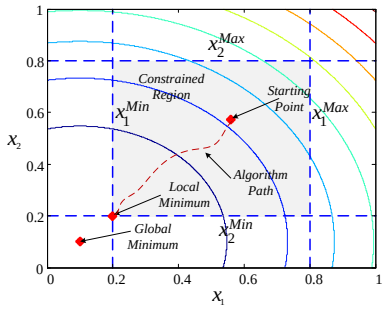

(b) Influence of constrains in the optimisation algorithm.

Figure 3.5: *Representation of constraints in an optimisation problem.*

Analysing the problem from (3.7) with the constraints (3.9), (3.10) and (3.11), the equality constraint, given by the network equation, and the inequality constraints given by the voltages and power limits, play an important role in finding the solution for the problem of losses minimisation. When choosing to stay on the line of the boundary, one degree of freedom is lost and the analysis using Lagrangian can be used again. However, the new vector has less one dimension.

Considering the loss optimisation case from figure 3.4, and it is possible to infer that the voltage at bus number 2 will be guided to the highest voltage level compared to the other buses. Choosing this bus for fixing the voltage level at one of the limits, the new equations for the objective function and the equality constraint becomes:

$$J\left(\widetilde{\mathbf{v}}_{DC}\right) = \widetilde{\mathbf{v}}_{DC}^{T} \cdot \widetilde{\mathbf{Y}} \cdot \widetilde{\mathbf{v}}_{DC} \tag{3.19}$$

$$\mathbf{g}\left(\widetilde{\mathbf{v}}_{DC}, \widetilde{\mathbf{p}}_{DC}\right) = \widetilde{\mathbf{Y}} \cdot \widetilde{\mathbf{v}}_{DC} + \left(diag\left(\widetilde{\mathbf{v}}_{DC}\right)\right)^{-1} \cdot \widetilde{\mathbf{p}}_{DC} \tag{3.20}$$

where $\widetilde{.}$ is new vector or matrix with less one element in case of a vector, or line in case of a matrix.

The inequality constraints, given by the voltage limitation, are written as follows:

$$\widetilde{\mathbf{v}}_{DC}^{min} \leq \widetilde{\mathbf{v}}_{DC} \leq \widetilde{\mathbf{v}}_{DC}^{max} \tag{3.21}$$

With less one degree of freedom, the Lagrangian equations can be applied again. For all the boundaries this checking must be considered. For the current system, four buses are available and 2 voltage limits per bus must be examined. For N buses, $2N$ boundaries must be checked. For meshed DC grids, it is possible to find more cases where the DC limits are achieved, and once more, the number of degrees of freedom is decreased. After checking of all the boarders, the checking in the corners come into picture. In the end, all of these results are put together and the minimum is selected.

For the loss minimisation case, the mathematical model, using the framework from (3.1), can be written according to (3.22).

$$\begin{aligned} &\textit{minimise} && \mathbf{v}_{DC}^{T} \cdot \mathbf{Y} \cdot \mathbf{v}_{DC} \\ &\textit{subject to} && \mathbf{Y} \cdot \mathbf{v}_{DC} + (diag\,(\mathbf{v}_{DC}))^{-1} \cdot \mathbf{p}_{DC} = 0 \\ & && \mathbf{v}_{DC}^{min} \leq \mathbf{v}_{DC} \leq \mathbf{v}_{DC}^{max} \\ & && \mathbf{p}_{DC}^{min} \leq \mathbf{p}_{DC} \leq \mathbf{p}_{DC}^{max} \end{aligned} \tag{3.22}$$

For the case presented in figure 3.4, there are six unknowns, the voltage values in the buses and the power shared by each onshore grid. For the equality constraints, three equations are derived from the node equation and they take into account the power balanced processed by the network.

The analytical solution presented above can be archived using the calculation of the Lagrangian function. However, for big systems it becomes not practical allowing the interior point algorithm to be used. Other methodologies are also available today. Examples of algorithms, besides interior point, are trust region reflective and active set. More advanced techniques are still in development and they apply genetic algorithms, neural networks and fuzzy logic.

The optimisation algorithm and the load flow analysis are related according to the flow diagram presented in the chart 2.

Algorithm 2 Optimized DC load flow algorithm for calculating operating points in DC networks

Require: Inputs:
- # of buses: $N + M$
- Type of buses: 1 or 2
- Power of Injection: P_M
- Cable impedances: $r_{i,j}$

Require: Variables Initialization:
- $V_n = 1.0$
- $V_m = 1.0$
- error = 1.0
- tolerance = 1.0e-9

function Y-BUS CREATION(Y_{Bus})
  Equation (3.8)
end function
Initialization of the optimisation vector: $\mathbf{x} = [V_1, \ldots, V_{N+M}, P_1, \ldots, P_N]$
function OPTIMIZATION($\mathbf{x}$)
  Determine a direction $\Delta\mathbf{x}$
  Objective function calculation: $\mathbf{J}(\mathbf{x})$ ▷ Required input $\mathbf{J}(\mathbf{x})$
  Line search
  Update $\mathbf{x}$
  if Constraints satisfied are not satisfied **then return**
  end if ▷ Required input $\mathbf{g}(\mathbf{x})$
end function
Update network variables

Implementing the algorithm presented in Figure 2, the results for the DC voltages values are presented in Figure 3.6.

Figure 3.6 shows the dashed lines illustrating the allowed region of variation of ±3%. As expected, the voltage levels on the infeed points (the buses where there

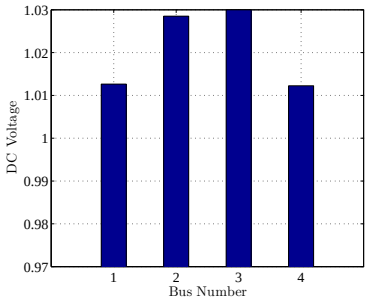

Figure 3.6: *DC voltage profile in the DC network.*

are power injection from the wind farms) achieve the maximum allowed values. On the other buses, they assume similar values as consequence of the minimisation of the objective function. For the power distribution, the measurements presented by the simulation is showed in Figure 3.7.

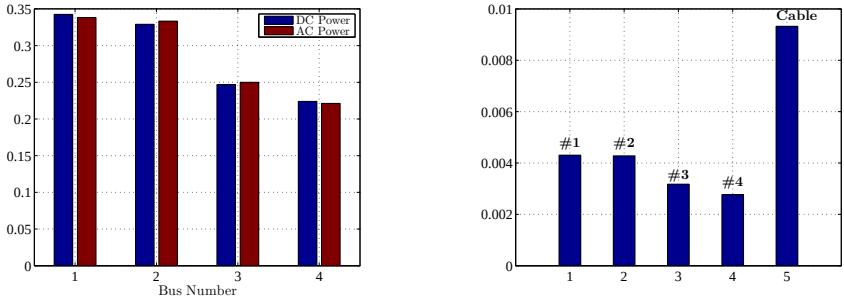

(a) Processed Power (b) Power Losses

Figure 3.7: *Power distribution for the transmission loss minimisation.*

The results presented by figure 3.7 show the possibilities and the explanation of operation of a DC network using DC voltage droop. However, just one operating point was considered. One can infer what are the conditions which are going to define the control signals for different operating points. The variability of the injected wind power and the different conditions of cable impedances can be taken into account.

For the power variation case, it is aimed to verify what are going to be voltage profiles for different wind conditions. The behaviour described by figure 3.8 shows the tendency of the system in maintaining the symmetry since the voltages in the terminal buses decrease at same ratings for variation in the wind farm production.

For the power and losses distribution, considering the delivered power from the wind power plants and the infeed powers injected in the AC grids, the results are showed in Figure 3.9.

Equations derived above to define the optimum DC load flow for transmission loss minimisation are related with the voltages at the DC buses and the system

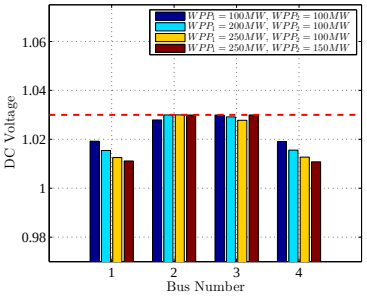

Figure 3.8: *Voltage profile variation in case of modification of wind power set points.*

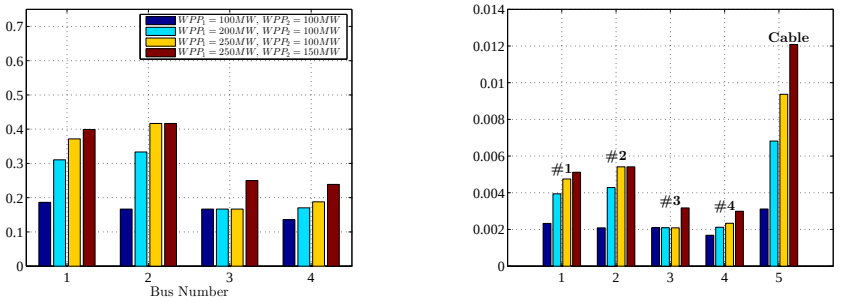

(a) Processed Power (b) Power Losses

Figure 3.9: *Power distribution for the transmission loss minimisation.*

characteristic given by branch impedances. The power flow results as consequence of the those variables. With this information in hands, a verification of the influence of cable variation over the voltage profile and power distribution can be intended.

Considering that the cable impedance of the branch with connects the offshore wind farm at bus number 2 to the land, thought bus number 4 changes its impedance from the minimum value of $100km$, and assuming the values $175km$ and later achieving the maximum values of $250km$, figure 3.10 shows a variation of impedances and how the voltage profile and power distribution are affected.

As the same as the previous results presented a symmetric variation of the voltage profile, the algorithm for the DC load flow based on transmission losses minimisation varies the onshore bus voltages with the same portion. The power instead, varies accordingly, flowing to the branches were the impedances are lower.

Observing the results, for a DC network, the classical load flow can be used and the choice of slack buses must be included, since the system presents more degrees of freedom than equations. However, the scenario is suitable for optimisation tools and, besides the fact that the algorithms can provide the load flow analysis, they are able to bring more flexibility.

A method based on the loss minimisation was analysed and its behaviour under

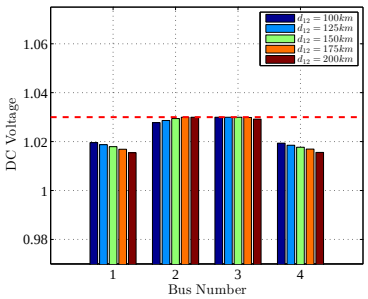

(a) Voltage profile

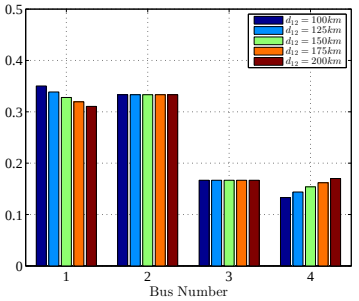

(b) Power distribution

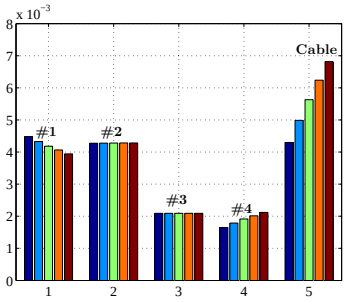

(c) Loss distribution

Figure 3.10: *System behaviour under cable impedance variation for transmission losses optimisation case.*

wind power injection variation and changes in the cable impedances were verified. For this approach, however, the power flow is a consequence of the parameters of the system, characteristic that can not be so tight in real applications since it is necessary to have the proper control of power or, at least, to control how the total power is shared among the stations connected in the DC link.

3.2.1.2 Total Loss Minimisation

The previous method showed an objective function based on the transmission losses in the DC link. However, one can consider to calculate the losses of the system and include the converter losses in the objective function. For the present case, the losses to be considered are the phase reactor losses and converter losses. Converter losses take into account the conduction losses and switching losses of the IGBT [38].

The phase reactor losses $P_{L,Reactor}$ are calculated using (3.23).

$$P_{L,Reactor} = 3\, r_{Reactor} I^2_{RMS} \tag{3.23}$$

where $r_{Reactor}$ is the phase reactor impedance and I_{RMS} is the RMS value of the

current through the reactor.

For the IGBT losses, two kind of losses are taken into account: the switching losses and conduction losses. For the following calculations, a basic linear loss model for power semiconductors is assumed. It means that, during each switching period, the voltage and current in the valve will follow a ramp curve during the increasing or decreasing conditions.

The equation of the switching losses of a VSC with sinusoidal AC line current and with IGBT switching devices is given by equation (3.24).

$$P_{Sw} = \frac{6}{\pi} f_{sw} \left(E_{ON,IGBT} + E_{OFF,IGBT} + E_{OFF,D} \right) \frac{V_{DC}}{V_r} \frac{i_o}{i_r} \tag{3.24}$$

where, f_{sw} is the switching frequency, $E_{ON,IGBT} + E_{OFF,IGBT} + E_{OFF,D}$ is the sum of turn-on and turn-off energies in the power modules, V_{DC} is the DC link voltage, i_o is the peak value of the AC line current and V_r and i_r are the blocking state voltages and currents occurring before the corresponding commutation. For the entire grid cycle, the sum of values calculated by (3.24) gives the average values for the losses.

For the conduction losses, the equation for calculation of it is given by (3.25).

$$\begin{aligned} P_C = 6 \Bigg(& \frac{\left(V_{CE} + V_F \right) i_o}{2\pi} \int_0^{\pi} \sin\left(\omega t\right) \frac{1 + m(t)}{2} d\left(\omega t\right) + \dots \\ & \frac{\left(r_{CE} + r_F \right) i_o^2}{2\pi} \int_0^{\pi} \sin^2\left(\omega t\right) \frac{1 + m(t)}{2} d\left(\omega t\right) \Bigg) \end{aligned} \tag{3.25}$$

where V_{CE} and V_F are the IGBT and diode threshold voltage, r_{CE} and r_F the differential resistances and $m(t)$ is the modulation function give by equation (3.26).

$$\begin{aligned} m(t) = & M \sin\left(\omega t\right) + \frac{3\sqrt{3}}{8\pi} \sum_{k=0}^{\infty} \Bigg(\frac{\sin\left(3\left(4k+1\right)\omega t\right)}{18k^2 + 9k + 1} - \dots \\ & \frac{\sin\left(3\left(4k+3\right)\omega t\right)}{18k^2 + 27k + 1} \Bigg) \end{aligned} \tag{3.26}$$

For this loss minimisation case, the upgraded cost function must present the previous equation, given by the total DC transmission losses, and added now with the factors given by equations (3.24) and (3.25). The phase reactor losses will not be taken into account since it will drive the results to minimum power transmission which is not desired. Proceeding on the same way as mentioned before for the transmission loss minimisation case, the cost function can be defined according to (3.27).

$$J\left(\mathbf{v}_{DC}\right) = \mathbf{v}_{DC}^T \cdot \mathbf{Y} \cdot \mathbf{v}_{DC} + \left(\mathbf{P_C} + \mathbf{P_{Sw}} \right) \tag{3.27}$$

Once more, the values for the DC voltage and the power delivered to the AC grids are the aims. At this time, a more complicated function is considered

since the vector $\mathbf{P_C}$ and $\mathbf{P_{Sw}}$, always positive, related with the power losses in each converter station are taken into account in the optimisation loop. The same constraints are still used.

As soon as the values for $\mathbf{P_C}$ and $\mathbf{P_{Sw}}$ are inserted in the object function, more calculation is required to process the same algorithm used in figure 2. For each iteration, an updated value of converter losses must be given to the optimisation block which will define the proper values for DC voltages and processed power.

First of all, the sending end station (in this case the bus number 2 and 3) calculates the voltages and currents in the terminals of the converters for the desired AC voltage, active power and reactive power. The values for the series reactors and their impedances are also given. Calculating the voltages in the terminals of the converter, currents processed by each phase throughout a simple circuit analysis, and for a initial values for DC voltage, the injected DC power is calculated.

With the injected DC power in the offshore terminals, the same algorithm presented by figure 2 and for the cost function given by (3.27) new values for the DC voltages and DC powers are calculated. New values for the offshore converters are loaded and updated values for the injected DC power are estimated. Once more, the optimisation loop starts until the new updated value for the injected DC powers match with the previous calculated ones.

For the inverter stations, the calculation of the power delivered to the AC grid requires another checking and error loops. However, it is not required to happen simultaneously to the optimisation loop. This function just needs to identify the correct values for the DC losses an calculated the variables inside the onshore stations.

Taking the DC power, calculated with the optimisation processed before, this value is updated as the converter is lossless. An estimation for the power losses in the converter is performed. The difference between the new DC power and the real one calculated using the optimisation tool is updated in the new AC power processed by the converter. If a tolerance is achieved, the loop stops, if not, new values are calculated. The simplified flow diagram of the algorithm described here is presented in the chart 3.

Algorithm 3 Optimized DC load flow algorithm for calculating operating points in DC networks considering converter losses

Require: Inputs:
- # of buses: $N + M$
- Type of buses: 1 or 2
- Power of Injection: P_M
- Cable impedances: $r_{i,j}$

Require: Variables Initialization:
- $V_n = 1.0$
- $V_m = 1.0$
- error $= 1.0$
- tolerance $= 1.0\text{e-}9$

function Y-Bus Creation(Y_{Bus})
  Equation (3.8)
end function
function Converter Initialization(Y_{Bus})
  Initialization of converter variables
  (Equations (3.23), (3.24),(3.25) and (3.26)) ▷ Required input: converter parameters
end function
if error $\geq$ tolerance **then**
  Initialization of the optimisation vector: $\mathbf{x} = [V_1, \ldots, V_{N+M}, P_1, \ldots, P_N]$
  function Optimization($\mathbf{x}$)
    Determine a direction $\Delta\mathbf{x}$
    Objective function calculation: $\mathbf{J}(\mathbf{x})$ ▷ Required input $\mathbf{J}(\mathbf{x})$
    Line search
    Update $\mathbf{x}$
    if Constraints satisfied are not satisfied **then return**
    end if ▷ Required input $\mathbf{g}(\mathbf{x})$
  end function
  Update network variables
  function Offshore Converter Parameter Calculation
    Converter loss calculation
    Converter variable calculation
    Error calculation
  end function
else
  function Onshore Converter Parameter Calculation
    if error $\geq$ tolerance **then**
      Onshore AC power estimation
      Converter loss calculation
      Error calculation
    end if
  end function
end if

For the present case, the converter parameters were adjusted using trying and error method for achieving IGBT losses around 1.1% and phase reactor losses close to 0.12%

The converter minimisation losses can be analysed using two conditions. The first one, just the converter losses are taken into account. Just the two latest components of (3.27) are considered. The second case uses all the parameters. The voltage profile provided by both cases are showed in Figure 3.11(a).

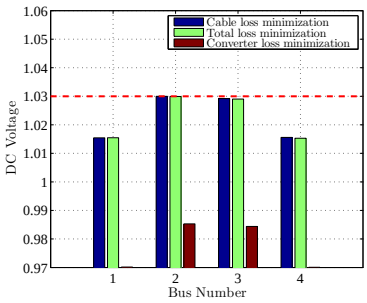

(a) DC voltage profile in the DC network.

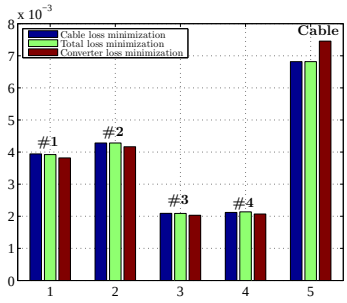

(b) Comparison of losses among the loss minimisation methods.

Figure 3.11: *Loss minimisation voltage profile and loss distribution results.*

The transmission losses drive the voltages to the values close to the ones presented by the cable loss minimisation case. Also, the gains for minimal converter are not considerable. Figure 3.11(b) shows the comparison of losses among the loss minimisation methods.

The inclusion of the converter in the optimisation does not contribute with the total losses minimisation when the cable losses is also considered. The power distribution is not controllable and a considerable converter loss minimisation is followed by a significant increase in the cable losses. The main conclusion here is that for the converter loss point of view, better converter topologies is required.

3.2.2 Dispatch Optimisation

As presented before, despite the fact that for the DC transmission losses achieve the optimum operation point for network constrains and voltage limits, the power delivered to each onshore stations is a result of the configuration and parameters of the DC network. For the control viewpoint, the power sharing is one of the main issues since the agreement among the owners of the assembled DC network, converter station and wind farms can consent in different schedules for delivered power in each onshore site. At this point, it is possible to analysed the voltage profile of the DC network regarded the perspective of the power sharing control.

3.2.2.1 Dispatch Error Minimisation

The first case is directly related with the error in the power schedules. It takes into account the normed error among all of the power sharing set points and the resultant given by the network considering losses in converters and cables (3.28).

$$J\left(\mathbf{v}_{DC}, \mathbf{p}_{DC_D}\right) \quad = \quad \left\|\mathbb{P}_{DC} - \mathbf{p}_{DC_D}\right\| \tag{3.28}$$

where $\mathbb{P}_{DC_D}$ is the desired value for the delivered power in each offshore converter and $\mathbf{p}_{DC_D}$ is the calculated value.

Considering that the total wind power is committed to be shared by rating of $\mathbf{p}_{DC_1} : \mathbf{p}_{DC_4}$ of the total power produced by the wind farms, as a result, minimising (8) represents the minimal error in the dispatch. The voltage profile and power distribution calculated for this cost function are illustrated in Figure 3.12.

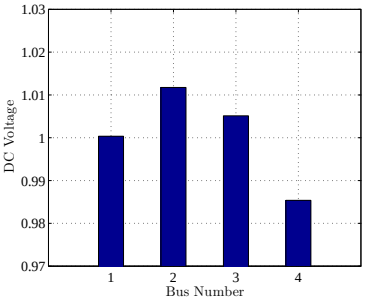

(a) Voltage profile

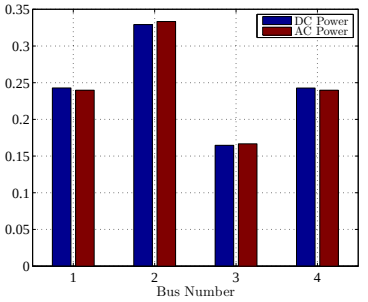

(b) Power distribution

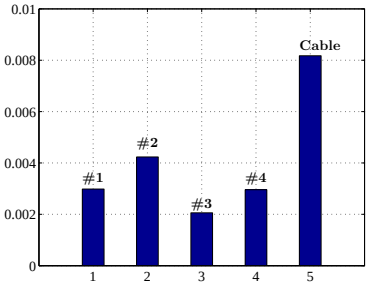

(c) Loss distribution

Figure 3.12: *Voltage profile and power distribution as result of DC load flow.*

3.2.2.2 Power Delivery Maximisation

Not taking into account the losses in the system, (3.28) can be replaced by a weight squared function in which the results combine the power sharing and loss

minimisation problem. Such equation is represented by (3.29).

$$J\left(\mathbf{v}_{DC}, \mathbf{p}_{DC_D}\right) = \sum_{i=1}^{N} w_i P_{DC,D_i}^2 \tag{3.29}$$

For (3.29) the algorithm tries to maximise the power delivered to both grids. The weights w_is are directly related with the agreed sharing in the schedule.

The same conditions for the previous are simulated in order to calculate the voltage profile in the system from figure 3.4. The results are showed in figure 3.13.

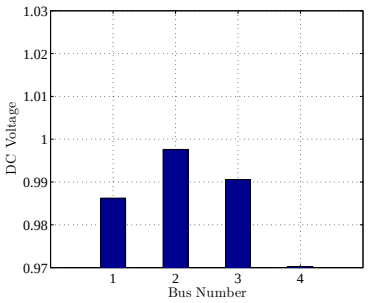

(a) Voltage profile

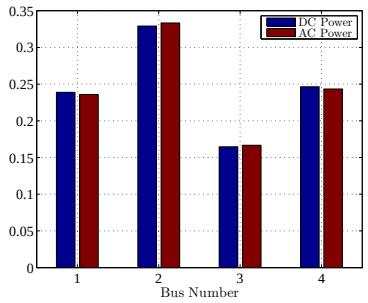

(b) Power distribution

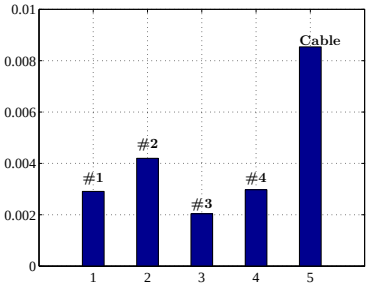

(c) Loss distribution

Figure 3.13: *Voltage profile and power distribution as result of DC load flow.*

3.3 Performance Evaluation

The simulation results show the influence of the optimizer in the transmission losses of the system. The first case shows the comparison between the solution given by a classical load flow and the one provided by the loss minimisation case. The classical load flow results would be affected by the scheduled power dispatch at bus #4, as bus #1 is defined as the slack bus. Figure 3.14 shows the results.

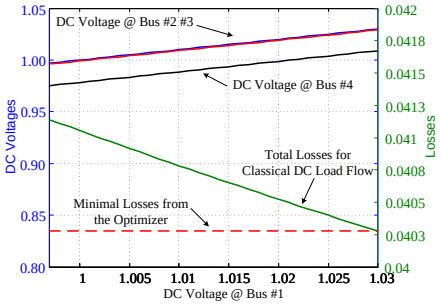

Figure 3.14: *Influence of the optimizer in the of determination minimum loss.*

From Fig. 3.14, the variation of the power flow in the bus #1 was from 0.542 pu to 0.543 pu for a base power equal to $600MW$. This represents a very small difference for the desired schedule. Moreover, the power for bus #4 was kept constant at 0.250 pu. Meanwhile, the AC power processed by the converters #1 and #4 in case where the optimizer was processing the minimum loss case presented the values of 0.523 pu and 0.270 pu, respectively.

The final study considering, all the optimisation conditions, are illustrated in the power distribution and voltage profiles from Fig. 3.15(a) and 3.15(b), respectively.

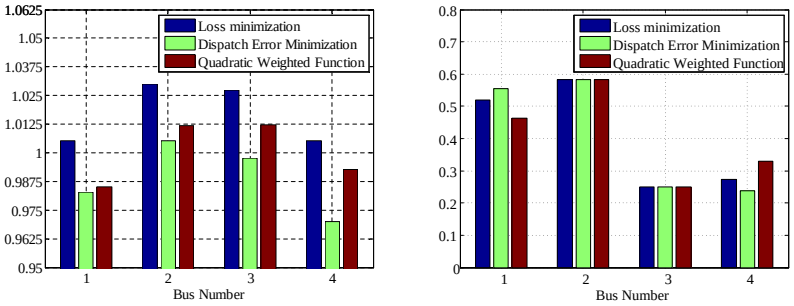

(a) Voltage Profile (b) Power Distribution

Figure 3.15: *Optimal operating points comparison.*

The voltage variation among the considered methods is very narrow, less than 2% for the worst case. Besides that, the losses presented by the cases are very similar to each other which means that, even not beeing the optimal solution for the losses, they offer an operating point in which the dispatch is satisfied and the losses are close to the minimal possible solution allowed by the system limitation range.

CHAPTER 4

Linear Dynamic Model of Voltage Source Converters for HVDC Application

The VSC-HVDC power converters connected by means of DC cables exhibit a dynamic behaviour that affects the entire DC link as well as the AC grids in which they are tied. The converter controllers play an important role in the HVDC integration and their interaction can be studied using linear analysis. Such approach can investigate the effectiveness of controllers and converter interaction into the power system.

This chapter describes the analysis by means of small signal stability approach of a single-link HVDC transmission system. The contents are going to, first of all, present the converter modelling by means of linearisation and frequency response. The converter control feedback system is formed by inner controller which is responsible for controlling AC currents and the outer control loops for DC and AC voltage compensation.

The modelling is split in following main sections. The first is related to the characterisation, by means of state space, of the AC side of the converter. The current control is the main focus and the interactions with synchronisation, high frequency filter and grid impedance are modelled during the inner loop modelling. The outer controllers are presented in the following.

The last section presents a dynamic model for a single-link VSC-HVDC transmission system based. The main results in this chapter are related to such simulation scenario. The intermediate results, showing the model validation for the AC current control as well as for the DC and AC control systems are presented in appendix A.

4.1 Introduction

As a solution for long distance and absence of reactive power compensation, the high voltage DC transmission system has become attractive for the renewable energy market, focusing in offshore wind systems. An overview of the number of HVDC projects as a backbone are listed in tables 1.3 and 1.4.

Considering a back-to-back HVDC connecting the offshore wind farms to the land by submarine cables, this system can be represented by following modules. The first main module is represented by the offshore wind farm that is connected with the offshore HVDC converter station by the AC cables. The HVDC converter station contains the voltage source converter which is the responsible for the energy conversion and exchange between the AC side collector and the DC link bus.

Between offshore and land, the cable links both stations. At onshore side, the second converter station, having the same type of components presented offshore, delivers the offshore to the utility which is the former module of a DC transmission representation. A simplified schematic for a single-link VSC-based transmission system is illustrated by the figure 4.1.

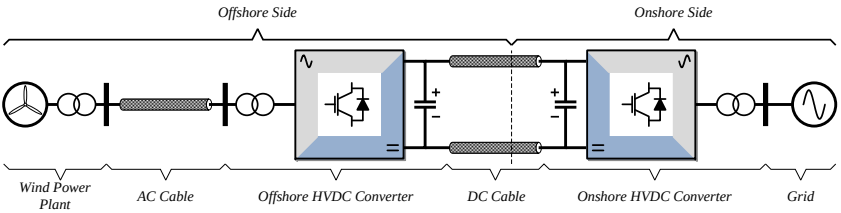

Figure 4.1: *Simplified schematic of a single-link VSC-HVDC transmission.*

As the centre part of the system in the schematic from figure 4.1, the voltage source converter is required to perform according to the grid codes defined by the utility grid where the energy is delivered. In order to fulfil such requirements, each of the converter station requires high performance of their internal controllers. The dynamic response of the VSC-controller, as well as the wind farm controllers are the main players in defining the appropriate energy transfer dynamics from offshore to onshore.

4.2 Modelling and Control of the VSC

Using classical feedback control, the voltage source converter can present different methods for its control architecture. Some of them are well known in the literature and the three more attractive ones are: power-angle control [39], vector control [40] and power-synchronization control [41]. In all the cases, there is a control for AC currents that tries to shape the AC currents as near as possible of a sinusoidal waveform. On the same time, the four quadrant angle operation

enabling the bidirectional power transfer capability is as well aimed. The compensation of the variation in the DC voltage or AC voltages are also in the control objectives.

This text makes use of the current vector control and the voltage compensation by means of linear output feedback control. The overall control architecture is split in inner loop and outer loops. The most inner feedback system shapes the amplitude and frequency of the AC currents and, the outer controllers are regulators for the DC voltages or AC voltages.

The definition of the control mode in the outer loops (DC or AC voltage control modes) is dependent of the grid conditions. For the onshore operation mode, the voltage source converter is in the DC voltage operation mode. The measurement of the DC voltage is taken for a reference error generation and further compensation. The control output defines the reference for the D-axis current i_D^*. The Q-axis component related to reactive power compensation is not considered in the studies and a reference value for this variable is applied directly in the inner controller reference. The control diagram for the voltage source converter in DC voltage control mode is illustrated in figure 4.2.

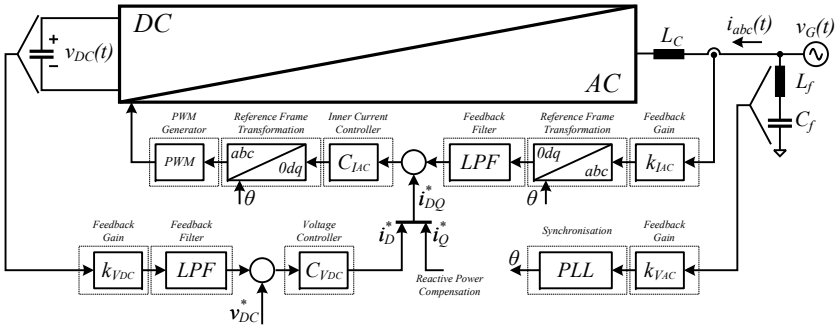

Figure 4.2: *General feedback system architecture of voltage source converters in DC voltage control mode.*

In the AC voltage control mode, the voltage source converter defines the amplitude and frequency of the voltage waveform applied in the point of common coupling. This type of control is used in case of very weak AC grids [42] and has been used in this study in the offshore stations where the wind farms are connected with. The control block diagram of the offshore stations are depicted in figure 4.3.

The further developments in this chapter describe the linear modelling process of voltage source converter. The analysis is performed by means of state space linear approach. The current model is tested with a classical proportional-integral control. The synchronisation loop as well the grid model are also included. The outer loops appear in the following two separated sections of the present chapter. The validation of the model is realised by means of comparison with time domain simulation using EMTDC type platform, and the results with comparisons between linearised state space model and ETMDC model are presented in last section, where the model is validated in a single-link VSC-HVDC transmission as

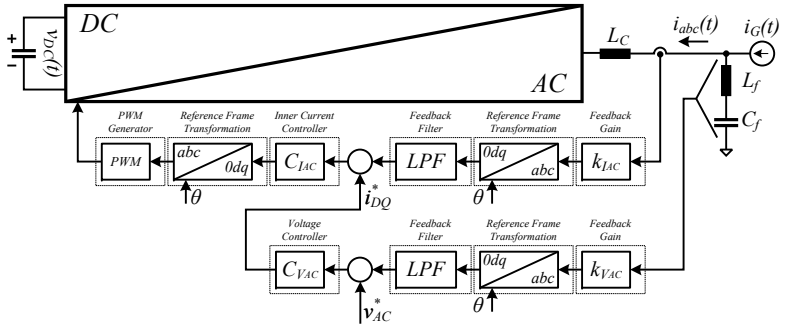

Figure 4.3: *General feedback system architecture of voltage source converters in AC voltage control mode.*

study case. Appendix A presents the preliminary model validation for each of the modules inside in each of the main blocks from figure 4.1.

4.3 The Inner AC Current Control Loop

The HVDC converter considered for this analysis is a two level converter type. The three phase system is formed by six current bidirectional switches, two per phase. The Pulse Width Modulation (PWM) controls the firing instants of the IGBT switches. The converter schematic is presented in figure 4.4.

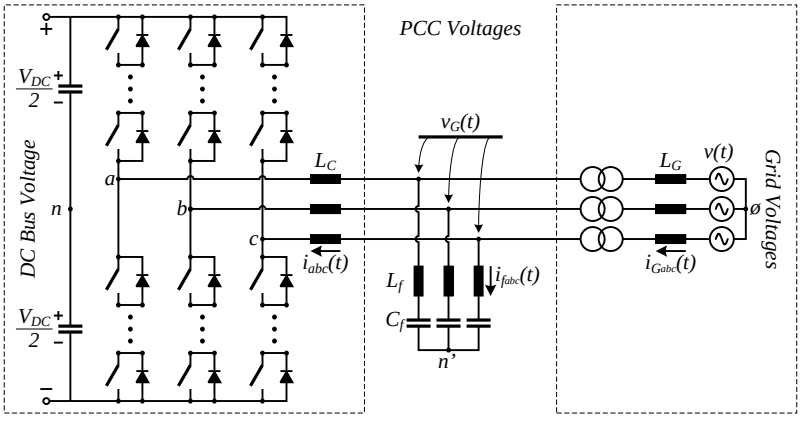

Figure 4.4: *Two level converter topology circuit diagram.*

The inductor L_C acts as a filter for the phase currents and the capacitor in the DC link is the voltage filter. The harmonic content of the phase reactor currents requires filtering. The branch tuned filter, composed by an inductor L_f and C_f offers a low impedance path for the high frequency components of the phase reactor currents. A resistor R_f is connected in parallel with the filter inductor in order to offer a damping effect for the system.

For this study, just one filter branch is included in the system. In real applications, usually, two branches are present; one for the switching frequency and another branch for twice this frequency.

The power transformer is placed at the output of the converter in order to adapt voltage levels. An equivalent inductor models the effect of the transformer and such inductance is included in the final value of the grid impedance L_G. The AC grid is simplified using an equivalent Thèvenin model.

The top level ratings for the system, such as voltage and power levels, were based in a real system presented in [43] and summarised in table 4.1.

Parameter	Value	Unit	Comment
Power Rating	400	MW	[43]
Number of Circuits	1		[43]
AC Voltage	150	kV	Assumed
DC Voltage	±150	kV	[43]
Converter Type			Two-Level VSC

Table 4.1: *Parameters for the voltage source converter from reference project [43].*

The converter modelling procedure follows the average model; analysis presented by [44, 42]. The converter switching effect is not considered, which means that just lower frequencies than the switching frequency can be analysed.

Due to dynamic decoupling, the converter modelling is split in inner and outer loops where the current dynamics is controlled in the inner loop and for the outer loops, the DC or AC voltage compensation are present. The synchronization between grid voltage and converter is performed by the phase-locked loop (PLL) as an extra control loop presented in the system in case of onshore control mode.

In the current loop modelling purpose, the outer loops represented by the voltage controllers are not considered and the variables related to DC and AC voltages, as well as the converter current references are taken as inputs for the system. The proper model of the figure 4.4 can be split in three main blocks: one representing the current control loop detailed in figure 4.5 and two extra blocks representing the dynamics of the high frequency filter and the grid impedance. Figure 4.5 illustrates the interconnection among the main blocks considered in the AC current inner loop.

The grid model contains the dynamic properties of the grid impedance set by the assumed short circuit ratio. The high frequency filter model covers the differential equations relating the filter capacitor, the filter inductor and the damping resistor connected in parallel with it. The converter model, controller, measuring devices and modulator are all included in the converter current loop block.

The PLL is the synchronisation loop. It is not explicitly shown in figure 4.4, however, it is represented an external block in the figure 4.5. The phase-lock loop is not present in the offshore converter station controller as well due to the fact that the VSC-HVDC converter imposes the amplitude and frequency for the voltages at the point of common coupling with the AC collector of the offshore

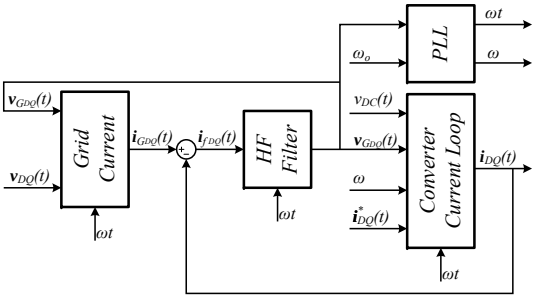

Figure 4.5: *Block diagram representation of inner current controller.*

wind farm.

For the converter control loop, the most inner loop is the converter model, the figure 4.6 illustrates the general control block diagram of a VSC.

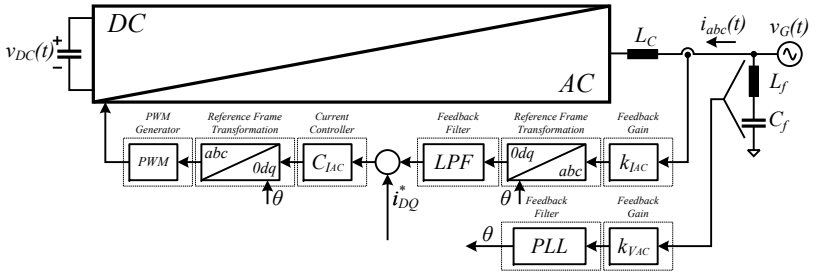

Figure 4.6: *General VSC control block diagram for the current control.*

From figure 4.4, $v_G(t)$ is the instantaneous grid voltage at the point of common coupling (PCC), L_C is the phase reactor inductance, $d_n(t)$ is the PWM firing pulse of the n^{th} IGBT, $v_C(t)$ is the instantaneous DC voltage at the terminals of the converter and C_{DC} is the DC link capacitor. $m(t)$ is the continuous modulation index signal applied in the modulator to generate the gate signals. The instantaneous grid voltages are cosine waveforms written in (4.1), (4.2) and (4.3).

$$v_{G_a}(t) = V_G \cos(\omega t + \theta_G) \tag{4.1}$$

$$v_{G_b}(t) = V_G \cos\left(\omega t - \frac{2\pi}{3} + \theta_G\right) \tag{4.2}$$

$$v_{G_c}(t) = V_G \cos\left(\omega t + \frac{2\pi}{3} + \theta_G\right) \tag{4.3}$$

Considering the circuit from figure 4.4, from the Kirchhoff's voltage law, the converter output voltages at the points a, b and c and the grid voltages $v_{G_a}(t)$, $v_{G_b}(t)$ and $v_{G_c}(t)$ can be written according to equations (4.4), (4.5) and (4.6).

$$v_{G_a}(t) = L_c \frac{d}{dt} i_a(t) + v_a(t) + v_n(t) \tag{4.4}$$

$$v_{G_b}(t) = L_c\frac{d}{dt}i_b(t) + v_b(t) + v_n(t) \quad (4.5)$$

$$v_{G_c}(t) = L_c\frac{d}{dt}i_c(t) + v_c(t) + v_n(t) \quad (4.6)$$

Equations (4.4), (4.5) and (4.6) are in the *abc* reference frame. For simplification purpose, the linear transformation given by (4.7) is applied.

$$A^{-1} = \sqrt{\frac{2}{3}}\begin{bmatrix} 1 & 0 & 0 \\ 0 & \cos(\omega t) & \sin(\omega t) \\ 0 & -\sin(\omega t) & \cos(\omega t) \end{bmatrix}\begin{bmatrix} \frac{1}{\sqrt{2}} & \frac{1}{\sqrt{2}} & \frac{1}{\sqrt{2}} \\ 1 & -0.5 & -0.5 \\ 0 & \frac{\sqrt{3}}{2} & -\frac{\sqrt{3}}{2} \end{bmatrix} \quad (4.7)$$

where A^{-1} represents the transformation matrix from the *abc* frame (canonical vector space) to rotating vector space such as is presented, generally, by equation (4.8).

$$\mathbf{x}_{\phi dq} = A^{-1}\mathbf{x}_{abc} \quad (4.8)$$

where $\mathbf{x}_{abc}$ are the coordinates of any three dimensional vector, which can be transformed to the new basis (ϕdq) by means of the Park's power invariant transformation A^{-1}.

Expanding the variables that represents the output voltage of the voltage source converter by its relationship representation with DC link voltage and modulation index and considering (4.7), it is possible to derive (4.9), (4.10) and (4.11).

$$L_c\frac{d}{dt}i_{\emptyset}(t) = v_{G_{\emptyset}}(t) - m_{\emptyset}(t)\frac{v_{DC}(t)}{2} - v_n(t) \quad (4.9)$$

$$L_c\frac{d}{dt}i_D(t) = v_{G_D}(t) - m_{\alpha}(t)\frac{v_{DC}(t)}{2} + \omega L_C i_Q(t) \quad (4.10)$$

$$L_c\frac{d}{dt}i_Q(t) = v_{G_Q}(t) - m_{\beta}(t)\frac{v_{DC}(t)}{2} - \omega L_C i_D(t) \quad (4.11)$$

Rewriting (4.9), (4.10) and (4.11) using vectorial form, and considering that the converter is working under balanced three-phase condition, which eliminates the necessity to carry the zero sequence component, the final equation for the AC converter current model is represented by (4.12).

$$L_c\frac{d}{dt}\mathbf{i}_{DQ}(t) = \mathbf{v}_{G_{DQ}} - \frac{v_{DC}(t)}{2}\mathbf{m}_{DQ}(t) + \omega\begin{bmatrix} 0 & 1 \\ -1 & 0 \end{bmatrix}\mathbf{i}_{DQ}(t) \quad (4.12)$$

For the purpose of this thesis, the model does not consider grid unbalances what simplifies (4.12) by considering just the last two components of the vectors (d and q components). The grounding current is also not considered. With this examination, (4.12) can be represented by the block diagram from figure 4.7.

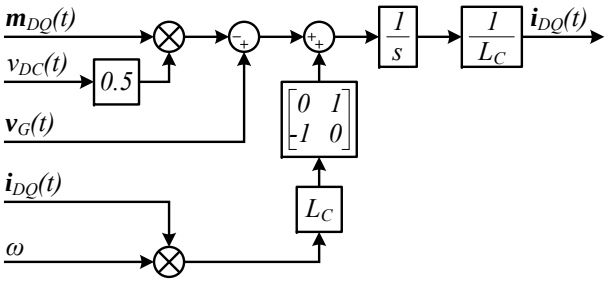

Figure 4.7: *Block diagram of the non-linear model of converter AC current.*

4.3.1 Small Signal Linear Model

The model from (4.12) is a non-linear model. The non-linearities are represented by the multiplier blocks from figure 4.7. In order to obtain a linear model for the converter current loop, a linearisation process using Taylor's Series is used. The Taylor's Series of the multiplication of two time domain variables $x(t)$ and $y(t)$ can be written such as (4.14).

$$\begin{aligned} x(t)y(t) &\approx XY + (x(t) - X)\left.\frac{\partial}{\partial x(t)}\left(x(t)y(t)\right)\right|_{X,Y} + \\ &\quad + (y(t) - Y)\left.\frac{\partial}{\partial y(t)}\left(x(t)y(t)\right)\right|_{X,Y} \qquad (4.13) \\ x(t)y(t) &\approx XY + X\Delta y(t) + Y\Delta x(t) \qquad (4.14) \end{aligned}$$

where X and Y are the values of the $x(t)$ and $y(t)$ variables at the equilibrium points and $\Delta x(t)$ and $\Delta y(t)$ are the increment variables. The approximation does not consider the higher order terms.

The standard form for representing dynamic linear systems is through state space model, where a n order system has its coupled differential equations represented by a set of first order differential equations and its input-to-output relationship are preserved. The standard state space representation is shown by (4.15).

$$\left.\begin{array}{rcl} \dot{\mathbf{x}}_{n\times 1}(t) &=& A_{n\times n}\mathbf{x}_{n\times 1}(t) + B_{n\times p}\mathbf{u}_{p\times 1}(t) \\ \mathbf{y}_{q\times 1}(t) &=& C_{q\times n}\mathbf{x}_{n\times 1}(t) + D_{q9\times p}\mathbf{u}_{p\times 1}(t) \end{array}\right\} \qquad (4.15)$$

where $\dot{\mathbf{x}}$ are the n state variables, $\mathbf{u}$ and $\mathbf{y}$ the p input and q output signals respectively. The general block diagram for the state model from (4.14) is illustrated in the figure 4.8.

The complete model of the AC side of the voltage source converter is split in four sub-systems with connection diagram presented in figure 4.5. The complete state space model for the AC currents and AC voltages for such device is divided in the following tasks:

- Converter modelling
  - AC current ($i_{abc}(t)$)

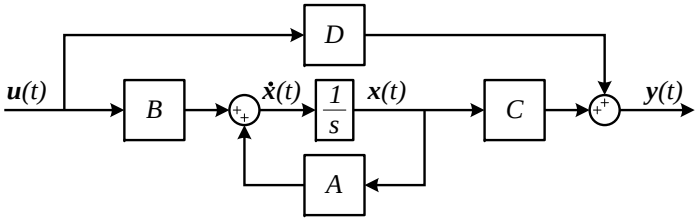

Figure 4.8: *State space representation system block diagram.*

  - AC current controller
  - Feedforward compensation

- Grid current modelling ($i_{G_{abc}}(t)$)
- High frequency filter modelling ($i_{fabc}(t)$ and $v_{Gabc}(t)$)
- Synchronisation (PLL) modelling

4.3.1.1 Converter Current State Space Model

Linearising (4.12) by means of (4.14), the linear model for the AC currents of the voltage source converter can be represented by the linear state space model in (4.15). Its linearised block diagram is illustrated in figure 4.9.

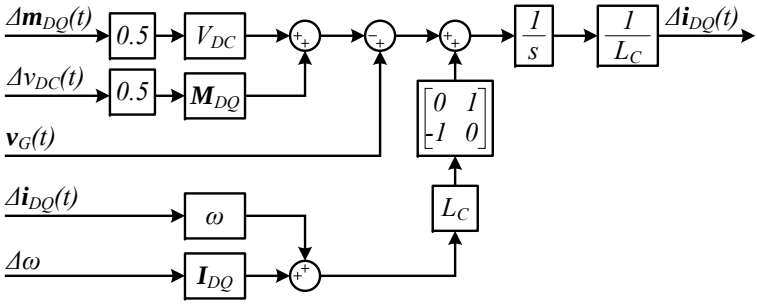

Figure 4.9: *Block diagram of the linear model of converter AC current.*

The non-linearity given by the multiplier block is replaced by a summation and gains which values are referenced by the system operating points.

The state space realization for the current loop considers as inputs the modulation signals $\Delta\mathbf{m}_{DQ}$, DC and AC voltages Δv_{DC} and $\Delta\mathbf{v}_{G_{DQ}}$, and grid frequency $\Delta\omega$. The state variables are the converter AC currents in the synchronous reference frame multiplied by the phase reactor inductance $\Delta\mathbf{i}_{DQ}$. The state vector,

input and output vectors are given by (4.16), (4.17) and (4.18), respectively.

$$\mathbf{x}_P(t) = \begin{bmatrix} L_C\Delta i_D(t) & L_C\Delta i_Q(t) \end{bmatrix}^T \tag{4.16}$$

$$\mathbf{u}_P(t) = \begin{bmatrix} \Delta v_{DC}(t) & \Delta v_{G_D}(t) & \Delta v_{G_Q}(t) & \Delta\omega & \Delta m_D(t) & \Delta m_Q(t) \end{bmatrix}^T \tag{4.17}$$

$$\mathbf{y}_P(t) = \begin{bmatrix} \Delta i_D(t) & \Delta i_Q(t) \end{bmatrix}^T \tag{4.18}$$

The state space matrices, A_P, B_P, C_P and D_P, for the current loop is given by (4.19), (4.20), (4.21) and (4.22).

$$A_P = \begin{bmatrix} 0 & \omega \\ -\omega & 0 \end{bmatrix} \tag{4.19}$$

$$B_P = \begin{bmatrix} -\frac{M_D}{2} & 1 & 0 & I_Q L_C & -\frac{V_{DC}}{2} & 0 \\ -\frac{M_Q}{2} & 0 & 1 & -I_D L_C & 0 & -\frac{V_{DC}}{2} \end{bmatrix} \tag{4.20}$$

$$C_P = \begin{bmatrix} \frac{1}{L_C} & 0 \\ 0 & \frac{1}{L_C} \end{bmatrix} \tag{4.21}$$

$$D_P = \begin{bmatrix} 0 & 0 & 0 & 0 & 0 & 0 \\ 0 & 0 & 0 & 0 & 0 & 0 \end{bmatrix} \tag{4.22}$$

The converter parameters are calculated according to the general project description give by [43]. The main values related to the block diagram from figure 4.9 are presented in table 4.2.

Parameter	Value	Unit	Comment
Nominal Converter Power	400	MVA	[43]
DC Link Voltage	±150	kV	[43]
AC Voltage	150	kV	Assumed
Phase Reactor	21.5	mH	0.12pu - Assumed
Converter Topology			Two level
Switching Frequency	1950	Hz	Assumed
Modulation Type			Carrier-triangular-based PWM

Table 4.2: *Parameters for the voltage source converter.*

4.3.1.2 Proportional-Integral Control Action

The traditional controller adopted to compensate the error in the current closed loop system is a proportional-integral (PI) compensator type. The proportional part improves the system response and, meanwhile, the integral action guarantees zero error at steady state. The block diagram of a proportional-integral controller is presented by figure 4.10.

From figure 4.10, the reference signal $r(t)$ is compared with the measured system output signal $y'(t)$ and a error $e(t)$ is generated. This signal is processed

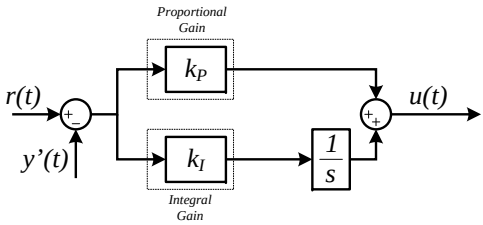

Figure 4.10: *General block diagram of a proportional-integral compensator.*

by the proportional and integral branches and combined to the controller output signal $u(t)$ which will drive the plant to the proper changes based in the error signal condition.

The states are the integrator input signals from 4.10. Two states are required since the vector control is adopted and they are labelled x_{I_I} and x_{I_Q}. The inputs are the reference signals i_D^* and i_Q^* and the feedback output signals i'_D and i'_Q. The PI output signals are u_D and u_Q.

For the current loop, where both, direct and quadrature, components of the currents are controlled, the state space model for its PI compensator is given by (4.23) and (4.24), where k_I and k_P are the proportional and integral gains tuned for a desired dynamic response.

$$\begin{bmatrix} \dot{x_{I_I}}(t) \\ \dot{x_{I_Q}}(t) \end{bmatrix} = \begin{bmatrix} 0 & 0 \\ 0 & 0 \end{bmatrix} \begin{bmatrix} x_{I_I}(t) \\ x_{I_Q}(t) \end{bmatrix} + \dots \\ \begin{bmatrix} -k_{I_D} & k_{I_D} & 0 & 0 \\ 0 & 0 & -k_{I_D} & k_{I_D} \end{bmatrix} \begin{bmatrix} i_D^*(t) \\ i'_D(t) \\ i_Q^*(t) \\ i'_Q(t) \end{bmatrix} \tag{4.23}$$

$$\begin{bmatrix} u_D(t) \\ u_Q(t) \end{bmatrix} = \begin{bmatrix} 1 & 0 \\ 0 & 1 \end{bmatrix} \begin{bmatrix} x_{I_I}(t) \\ x_{I_Q}(t) \end{bmatrix} + \dots \\ \begin{bmatrix} -k_{P_D} & k_{P_D} & 0 & 0 \\ 0 & 0 & -k_{P_D} & k_{P_D} \end{bmatrix} \begin{bmatrix} i_D^*(t) \\ i'_D(t) \\ i_Q^*(t) \\ i'_Q(t) \end{bmatrix} \tag{4.24}$$

Combining the state space model for the PI controller and the previous equations which describes the dynamics for the current loop and the feedback filter, the closed loop system for the current control of the voltage source converter is achieved. The parameter used for the current controller are given by the table 4.3.

4.3.2 Disturbances Effect

The control strategy adopted is a feedback control with PI controller. The integral gain guarantees the zero error in steady-state and the proportional gain

Parameter	Value	Unit
Proportional Gain	1.0	
Integral Gain	2450	
Bandwidth	390	Hz

Table 4.3: *AC current PI controller parameters.*

improves the dynamic response. More than just the control inputs, the feedforward terms are presented in order to assist faster response for the measurable disturbances: DC link voltage, grid voltage and coupling effect.

4.3.2.1 Feedback Linearization for DC Bus Voltage

The DC link voltage variation has effect over the output currents. The effect is directly compensated in the controller and the control commands mitigates, under a transient response, the consequence. The feedforward for the voltage controller is also included in the EMTDC and small signal model as illustrated in figure 4.11.

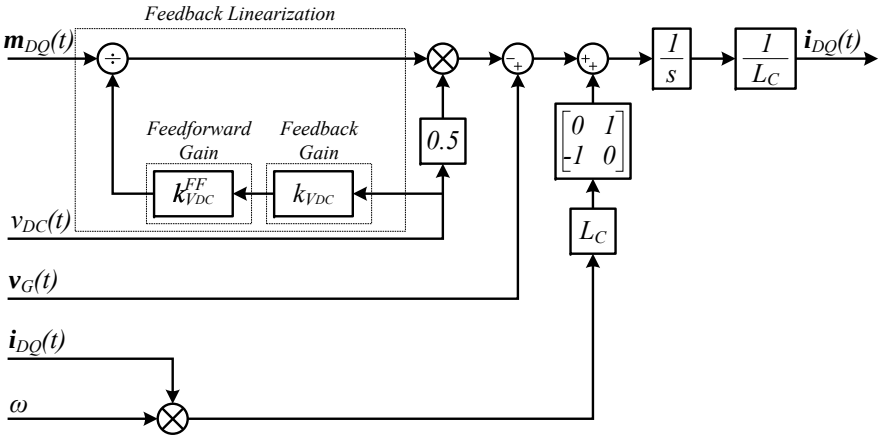

Figure 4.11: *Feedback linearization by means of feedforward control of DC link voltage.*

The feedforward path for the DC link voltage directly influences the controller, since all the effort for DC link disturbance mitigation is driven by the DC feedforward controller.

4.3.2.2 Grid Voltages Feedforward

From the dynamic model presented in the figure 4.8 shows the voltage at the point of common coupling as a disturbance input. This reflects in the control action during voltage transients, since the AC voltages have the additive effect.

In the presence of the feedforward control action, the effect of the voltage disturbances is mitigated on the current response. The feedforward for the AC

voltage compensation is represented by a simple signal addition in the output of the current control. Just the sensor gain and a feedforward gain $k_{FF_{i_{AC}}}$ are required to scale properly the signal in the control level. The error signals are not noticeably influenced by such variation. As a consequence, the control signal from the feedforward direct compensation takes the lead for disturbance reduction.

4.3.2.3 Feedback Linearisation for Decoupling Network

The effect of the current coupling terms in the synchronous reference frame appear where changes in each of the axis current references reflects in disturbances in the opposite current component. A feedforward term can be included in the complete control model, that such compensation is directly performed by a secondary branch in loop. As a consequence, the influence of one component into another is attenuated and the PI control does not have action in such situation.

4.3.2.4 Structure of the Inner Current Controller Feedforward

The disturbances presented in the current loop can distort the converter output currents and, as a consequence, the current controller is required to act to mitigate such effect. For fast response, however, the feedforward terms are included.

For the DC link voltage and the coupling between the DQ-axes currents, the feedforward requires non-linear operations. For the AC grid voltages, the compensation is made by a linear combination os signals.

Considering the the whole current controller as a combination of the PI controller, DC voltage, AC voltage and decoupling feedforward terms, the block diagram of the of the complete inner loop compensator is depicted in figure 4.12.

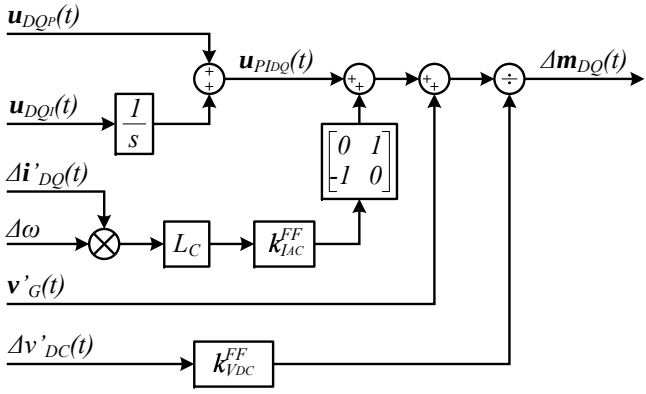

Figure 4.12: *Current controller block diagram with PI and feedforward compensation.*

where the $'$ symbols are the input variables weighted by the sensor gains. The

input and output vectors a given by (4.25) and (4.26), respectively.

$$\mathbf{u}_{PI}(t) = \left[\; v'_{DC}(t) \quad v'_{G_D}(t) \quad v'_{G_Q}(t) \quad \omega \quad i'_D(t) \quad i'_Q(t) \quad \ldots \quad u_{PI_D}(t) \quad u_{PI_Q}(t) \; \right] \tag{4.25}$$

$$\mathbf{y}_{PI}(t) = \left[\; m_D(t) \quad m_Q(t) \; \right]^T \tag{4.26}$$

The algebraic matrix which relates the output of the complete control model $\Delta m_{DQ}(t)$ and the PI output $u_{PI_{DQ}}(t)$ including the feedforward linearised compensation are presented in equation (4.27).

$$PI_{FF} = \begin{bmatrix} \frac{-M_D}{V''^{\,2}_{DC}} & \frac{1}{V''_{DC}} & 0 & \frac{I_Q L_C}{V''_{DC}} & 0 & \frac{\omega L_C}{V''_{DC}} & \frac{1}{V''_{DC}} & 0 \\ \frac{-M_Q}{V''^{\,2}_{DC}} & 0 & \frac{1}{V''_{DC}} & \frac{-I_D L_C}{V''_{DC}} & \frac{-\omega L_C}{V''_{DC}} & 0 & 0 & \frac{1}{V''_{DC}} \end{bmatrix} \tag{4.27}$$

The double prime symbols in the parameters in (4.27) are referenced to the measured input variables weighted by the feedforward gains in figure 4.12.

4.4 Grid Synchronisation

A phase locked loop (PLL) is required in the connection of voltage source converters and electric grid for the propose of reference tracking. The generation of unit sine and cosines signals required in the reference frame transformation is basically originated by the synchronization block. By then, it is required for the PLL an accurate tracking of the grid angle even under abnormal grid operation and under some harmonic content conditions [42, 45].

The basic structure of the three-phase synchronously rotating reference frame (SRF) based PLL has the basic block diagram illustrated by the figure 4.13.

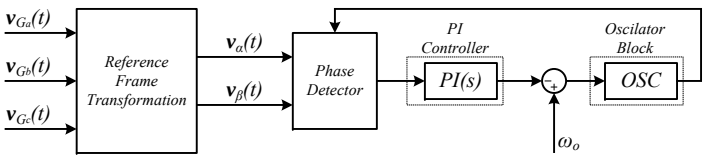

Figure 4.13: *Simplified block diagram of SFR PLL.*

The phase detector is responsible for generating the output signal proportional to the phase difference between the grid angle and generated angle reference. The loop filter, a PI controller which leads the error difference to zero in steady state. The voltage oscillator block generates the output signal whose frequency is a function of the input frequency of the grid.

Considering that the grid angle is represented by θ, as well as a balanced grid condition, the α and β components for the rotating frame is given by (4.28)

and (4.29).

$$v_{\alpha}^{'}(t) = \sqrt{\frac{3}{2}} V_G^{'} \cos(\theta) \tag{4.28}$$

$$v_{\beta}^{'}(t) = \sqrt{\frac{3}{2}} V_G^{'} \sin(\theta) \tag{4.29}$$

The output of the multiplicative phase detector from figure 4.13 extracts the phase of the system by means of 4.30.

$$\begin{aligned} \sqrt{\frac{3}{2}} V_G^{'} \sin(\theta - \omega t) &= -\sqrt{\frac{3}{2}} V_G^{'} \cos(\theta) \sin(\omega t) \ldots \\ &\quad + \sqrt{\frac{3}{2}} V_G^{'} \sin(\theta) \cos(\omega t) \end{aligned} \tag{4.30}$$

For small angle differences the component $\sin(\theta - \omega t)$ gives approximately the value of difference between the grid angle and the PLL synchronizing current angle. Considering the simplification from 4.30, the non-linear block diagram from figure 4.13 can be simplified by the linearised PLL control architecture given by the figure 4.14.

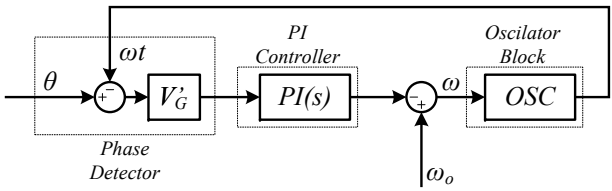

Figure 4.14: *Linearised block diagram for the SRF PLL.*

The state space representation of the system in which the block diagram is depicted in figure 4.14 is characterised by the matrices A_{PLL}, B_{PLL}, C_{PLL} and D_{PLL}. The input signals are the angle θ of the voltage at the PCC and nominal value of the grid angular frequency ω_o. The output of the PLL state space model is the PLL angle ωt. The states are the integrators from the PI integrator and from the voltage oscillator, respectively. The state space representation is by then, given through the equations (4.31) and (4.32).

$$\begin{bmatrix} \dot{x}_{PLL_{PI}}(t) \\ \dot{x}_{PLL_{OSC}}(t) \end{bmatrix} = A_{PLL} \begin{bmatrix} x_{PLL_{PI}}(t) \\ x_{PLL_{OSC}} \end{bmatrix} + B_{PLL} \begin{bmatrix} \theta \\ \omega_o \end{bmatrix} \tag{4.31}$$

$$\omega t = C_{PLL} \begin{bmatrix} x_{PLL_{PI}}(t) \\ x_{PLL_{OSC}} \end{bmatrix} + D_{PLL} \begin{bmatrix} \theta \\ \omega_o \end{bmatrix} \tag{4.32}$$

By then, the state space representation of the grid synchronisation block is

explicitly showed by (4.33), (4.34), (4.35) and (4.36).

$$A_{PLL} = \begin{bmatrix} 0 & -V_G' k_{I_{PLL}} \\ -1 & V_G' k_{P_{PLL}} \end{bmatrix} \tag{4.33}$$

$$B_{PLL} = \begin{bmatrix} V_G' k_{I_{PLL}} & 0 \\ -V_G' k_{P_{PLL}} & 1 \end{bmatrix} \tag{4.34}$$

$$C_{PLL} = \begin{bmatrix} 0 & 1 \end{bmatrix} \tag{4.35}$$

$$D_{PLL} = \begin{bmatrix} 0 & 0 \end{bmatrix} \tag{4.36}$$

The parameter V_G' represents the weighted amplitude of the voltage at the point of common coupling and $k_{I_{PLL}}$ and $k_{P_{PLL}}$ the parameters of the PI compensator. The control parameters for the nominal operating points are presented in table 4.4.

Parameter	Value	Unit
Proportional Gain	92	
Integral Gain	628.3185	

Table 4.4: *Control parameters for the PLL synchronisation loop.*

4.5 Grid Impedance and High Frequency Filter Models

The grid impedance can play an important role in the integration of the converter and the grid. For stiff grids, the impedance has a small effect under the effect of the other modes presented by internal converter loops. When the grid is considered a weak grid, this impedance may have effect over the other controllers and the performance of the entire system can unexpectedly be lower than the one in which it was design for[46]. The differential equation for the grid impedance considering the model presented by 4.4 is written by (4.37).

$$\mathbf{v}(t) = L_G \frac{d\mathbf{i}_G(t)}{dt} + R_G \mathbf{i}_G(t) + \mathbf{v}_G(t) + v_n'(t) \begin{bmatrix} 1 \\ 1 \\ 1 \end{bmatrix} \tag{4.37}$$

where, $\mathbf{v}(t)$ is the internal grid voltage vector, L_G the equivalent grid inductance and R_G is the equivalent grid series resistance. $\mathbf{i}_G(t)$ represents the converter currents after the high frequency filtering effect.

In equation (4.37) is written in the *abc* frame. The transformation from (4.7) is still valid and can remove the effect of the zero sequence for balanced grid conditions. Equation (4.37) can be written in synchronous reference frame according

to (4.38).

$$L_G \frac{d\mathbf{i}_{G_{DQ}}(t)}{dt} + R_G \mathbf{i}_{G_{DQ}}(t) = \mathbf{v}_{DQ}(t) - \mathbf{v}_{G_{DQ}}(t) + \ldots \\ \omega L_G \begin{bmatrix} 0 & 1 \\ -1 & 0 \end{bmatrix} \mathbf{i}_{G_{DQ}}(t) \tag{4.38}$$

For the equation (4.38), the block diagram for such differential equation is represented by figure 4.15.

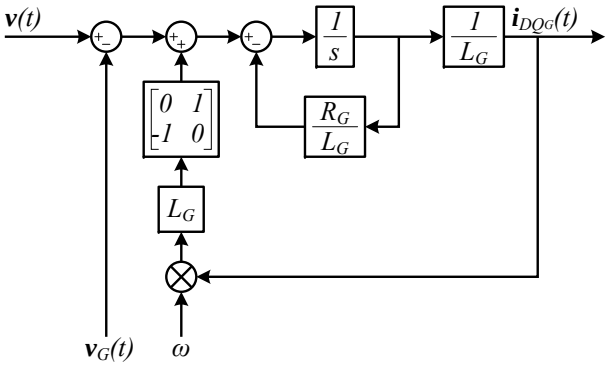

Figure 4.15: *Block diagram for the grid current dynamic model.*

The state, input and output vector from the model in the figure 4.15 are given in (4.39), (4.40) and (4.41).

$$\mathbf{x}_G(t) = \begin{bmatrix} L_G i_{G_D}(t) & L_G i_{G_Q}(t) \end{bmatrix}^T \tag{4.39}$$

$$\mathbf{u}_G(t) = \begin{bmatrix} \mathbf{v}(t) & \mathbf{v}_G(t) & \omega \end{bmatrix}^T \tag{4.40}$$

$$\mathbf{y}_G(t) = \begin{bmatrix} i_{G_D}(t) & i_{G_Q}(t) \end{bmatrix}^T \tag{4.41}$$

The state space matrices for the grid impedance linear model are given by the (4.42), (4.43), (4.44) and (4.45).

$$A_G = \begin{bmatrix} -\frac{R_G}{L_G} & \omega \\ -\omega & -\frac{R_G}{L_G} \end{bmatrix} \tag{4.42}$$

$$B_G = \begin{bmatrix} 1 & 0 & -1 & 0 & L_G I_{Q_G} \\ 0 & 1 & 0 & -1 & -L_G I_{D_G} \end{bmatrix} \tag{4.43}$$

$$C_G = \begin{bmatrix} \frac{1}{L_G} & 0 \\ 0 & \frac{1}{L_G} \end{bmatrix} \tag{4.44}$$

$$D_G = \begin{bmatrix} 0 & 0 & 0 & 0 & 0 \\ 0 & 0 & 0 & 0 & 0 \end{bmatrix} \tag{4.45}$$

The high frequency filter included in the circuit for current filtering is a shunt second order filter [47]. It acts as single-tuned filter for frequency below the resonance frequency, and as a high pass filter at higher the resonance. From the figure 4.4, the circuit of the high frequency filter is simplified. The schematic of this branch filter is illustrated in figure 4.16.

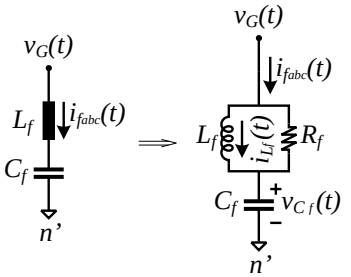

Figure 4.16: *Shunt second order passive filter.*

For the high frequency filter, the differential equation which relates the filter currents $\mathbf{i}_f(t)$ and the voltage at the point of common coupling with the voltage source converter $\mathbf{v}_G(t)$ is given by (4.46).

$$\frac{C_f L_f}{R_f}\frac{d^2\mathbf{v}_G(t)}{dt^2} + C_f\frac{d\mathbf{v}_G(t)}{dt} = C_f L_f\frac{d^2\mathbf{i}_f(t)}{dt^2} + \frac{L_f}{R_f}\frac{d\mathbf{i}_f(t)}{dt} + \mathbf{i}_f(t) \quad (4.46)$$

where, C_f, L_f and R_f are the filter passive component parameters. $\mathbf{i}_f(t)$ and $\mathbf{v}_G(t)$, the current and voltages of the high frequency filter, respectively.

Considering the differential equation from (4.46), the block diagram which represents the dynamic property between the input current of the filter and its voltage is given by figure 4.17.

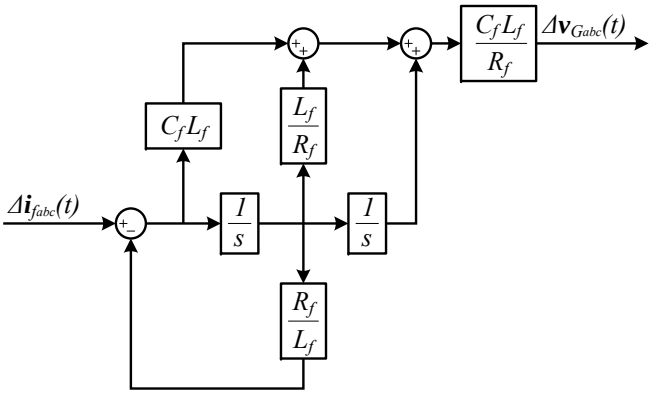

Figure 4.17: *Block diagram for the high frequency filter dynamic model.*

In the synchronous reference frame, considering the previous transformation presented by (4.7), the vectorial form for the high frequency filter differential

equation is give in (4.47).

$$\begin{aligned}\frac{C_f L_f}{R_f}\frac{d^2\mathbf{v}_{G_{DQ}}(t)}{dt^2} + C_f\frac{d\mathbf{v}_{G_{DQ}}(t)}{dt} &= C_f L_f\frac{d^2\mathbf{i}_{f_{DQ}}(t)}{dt^2} + \frac{L_f}{R_f}\frac{d\mathbf{i}_{f_{DQ}}(t)}{dt} + \dots \\ &\quad \mathbf{i}_{f_{DQ}}(t) + \omega^2\frac{C_f L_f}{R_f}\mathbf{v}_{G_{DQ}}(t) + \dots \\ &\quad \omega C_f\begin{bmatrix}0 & 1\\ -1 & 0\end{bmatrix}\mathbf{v}_{G_{DQ}}(t) - \dots \\ &\quad \omega^2 C_f L_f\mathbf{i}_{f_{DQ}}(t) - \dots \\ &\quad \omega C_f L_f\begin{bmatrix}0 & 1\\ -1 & 0\end{bmatrix}\mathbf{i}_{f_{DQ}}(t) \end{aligned} \tag{4.47}$$

For the state variables given by $\frac{L_f}{R_f}i_{L_f}$ and its derivative, the matrices of the linearised state space model for the HF filter is represented by (4.48), (4.49), (4.50) and (4.51).

$$A_{HF} = \begin{bmatrix}0 & 1 & \omega & 0\\ 0 & -\frac{R_f}{L_f} & 0 & \omega\\ -\omega & 0 & 0 & 1\\ 0 & -\omega & 0 & -\frac{R_f}{L_f}\end{bmatrix} \tag{4.48}$$

$$B_{HF} = \begin{bmatrix}0 & 0 & \frac{V_{R_{f_Q}}}{R_f}\\ 1 & 0 & \frac{L_f I_{R_{f_Q}}}{R_f}\\ 0 & 0 & -\frac{V_{R_{f_D}}}{R_f}\\ 0 & 1 & -\frac{L_f I_{R_{f_D}}}{R_f}\end{bmatrix} \tag{4.49}$$

$$C_{HF} = \begin{bmatrix}\frac{R_f}{C_f L_f} & \frac{1}{C_f} - \frac{R_f^2}{L_f} & 0 & 0\\ 0 & 0 & \frac{R_f}{C_f L_f} & \frac{1}{C_f} - \frac{R_f^2}{L_f}\end{bmatrix} \tag{4.50}$$

$$D_{HF} = \begin{bmatrix}R_f & 0 & 0\\ 0 & R_f & 0\end{bmatrix} \tag{4.51}$$

The node equation for the currents in the point of common coupling is written by (4.52).

$$\mathbf{i}_G(t) = \mathbf{i}_f(t) + \mathbf{i}(t) \tag{4.52}$$

The components of the branch tuned filter from figure 4.16 are based in the specification of reactive power consumption, quality factor and filtering frequency. The specification of the high frequency filter and its parameters are presented in table 4.5. The impedance characteristic of such device is presented in figure 4.18.

Parameter	Value	Unit
Reactive Power	26.7	MVA
Quality Factor	25	
Notch Frequancy	1950	Hz
Inductance	1.9	mH
Capacitance	3.4	μF
Resistance	600	Ω

Table 4.5: *High frequency filter settings.*

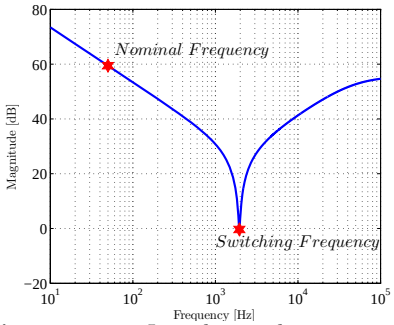

Figure 4.18: *Impedance characteristic.*

4.6 The Outer DC Voltage Control Loop

The direct DC voltage control method applied in the voltage source converter is able to, indirectly, regulate the power transfer between the AC and DC sides of the converter. Using the vector current control, the DC voltage loop is cascaded connected to the current control, promoting the D-axis reference current for the inner control loop. Changing the amplitude of the reference i_D^* current, the active power transfer is changed. Figure 4.19 brings the representation of the power flow in the two-level converter adopted to the analysis.

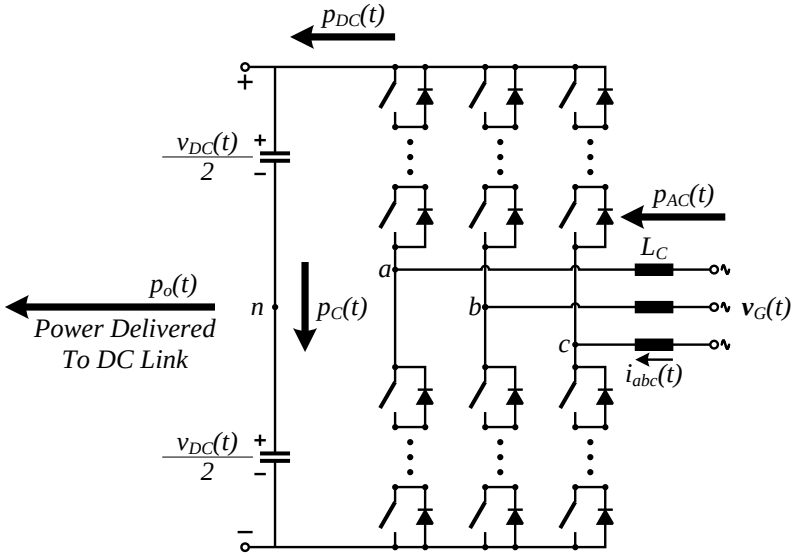

Figure 4.19: *Circuit schematic for voltage source converters with active power flow representation.*

From figure 4.19 the input power p_{AC} is processed by the converter resulting in the DC converter power p_{DC} and the converter losses P_{Losses} which is not specified in the figure. The total power delivered to the DC grid p_o is a result of

this DC power subtracted by the power used to charge or discharge the DC link capacitors.

The DC voltage control is, then, based in the instantaneous average model, which can be indirectly related with the instantaneous measurement of power in AC systems given by [44], where the active power is defined as the scalar product of the voltage and current vectors according to (4.53).

$$p(t) \quad := \quad \left(\frac{v_{DC}(t)}{2}\mathbf{u}_{DQ}(t)\right) \cdot \mathbf{i}_{DQ}(t) \tag{4.53}$$

where $\mathbf{i}_{DQ}$ is the current vector which flows through the phase reactors L_C, in synchronous reference frame. The term $\frac{v_{DC}}{2}\mathbf{u}_{DQ}$ represents the instantaneous voltage vector at the point *abc* from figure 4.19. v_{DC} is the DC bus voltage and $\mathbf{u}_{DQ}$ are the modulation indexes.

By applying the energy balanced law in the DC side of the converter from figure 4.19, the instantaneous input energy E_{DC} is numerically equal to the charging energy in the DC link capacitor C_{DC} and the output energy delivered to the DC link. This means that the energy balance equation is written according to (4.54).

$$E_{DC}(t) \quad = E_C(t) + E_o(t) \tag{4.54}$$

Differentiating (4.54) on both sides, it is possible to write the power balanced equation for the two-level converter type according to (4.55).

$$p_{DC}(t) \quad = \quad \frac{d\left(E_C(t)\right)}{dt} + p_o(t) \tag{4.55}$$

where the voltage versus energy relationship for the capacitor C_{DC} can be written according to (4.56).

$$E_C(t) \quad = \quad \frac{1}{2}C_{DC}v_{DC}^2(t) \tag{4.56}$$

Combining (4.56) into (4.55), the dynamic differential equation which describes the properties in the DC link voltage is derived by (4.57).

$$p_{DC}(t) \quad = \quad \frac{1}{2}C_{DC}\frac{dv_{DC}^2(t)}{dt} + p_o(t) \tag{4.57}$$

Considering the converter control loop from the figure 4.6, the aggregated input/output dynamic system can be represented with input signals given by the DC voltage $v_{DC}(t)$, voltage at the point of common coupling $\mathbf{v}_{G_{DQ}}$, grid frequency ω and referenced for the AC currents in the synchronous reference frame $\mathbf{i}_{DQ}^*$. The output of the current loop is the AC current vector $\mathbf{i}_{DQ}$. The grid angle is also required for the linear transformation presented by (4.7). For such modelling simplification and making use of equation (4.53), the plant for the DC voltage loop can be illustrated in the block diagram from figure 4.20.

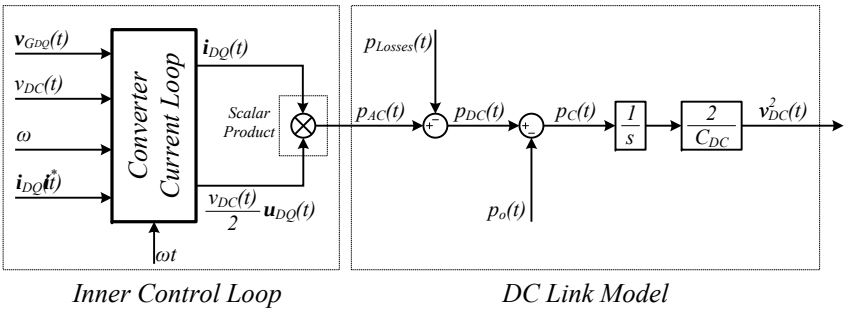

Figure 4.20: *Simplified block diagram of the DC voltage control loop.*

The non-linear block from figure 4.19 can be linearised by means of *Taylor's Series* using three variables. For the DC voltage controller, differently from the linearisation procedure presented in the current loop and feedforward, the expansion can continue up to the second order terms, since the relationship with the squared value of the DC voltage is in place due to energy balancing system. The series with the first and second order terms for n input signals is given in (4.58).

$$f(x_1(t),\ldots,x_n(t)) = f(X_1,\ldots,X_n) + \sum_{i=1}^{n}(x_i(t)-X_i)\frac{\partial f(x_1(t),\ldots,x_n(t))}{\partial x_i} + \frac{1}{2}\sum_{i=1}^{n}\sum_{j=1}^{n}(x_i(t)-X_i)(x_j(t)-X_j)\frac{\partial^2 f(x_1(t),\ldots,x_n(t))}{\partial x_i \partial x_j} \tag{4.58}$$

Considering (4.58) and the definition of instantaneous AC power at the AC terminals of the voltage source converter given by (4.53), the approximation of the AC power in figure 4.19 can be calculated using (4.60).

The expanded AC power calculation can be, as well, calculated according to (4.59).

$$p_{AC}(t) = \mathbf{u}_{DQ}(t)\frac{\sqrt{v_{DC}^2(t)}}{2}\mathbf{i}_{DQ}(t) \tag{4.59}$$

Considering (4.59) and the series expansion from (4.58), one can write (4.60).

$$p_{AC}(t) \approx -V_{DC}\mathbf{U}_{DQ}\mathbf{I}_{DQ} + \mathbf{u}_{DQ}(t)\frac{V_{DC}\mathbf{I}_{DQ}}{2} + v_{DC}(t)\frac{\mathbf{U}_{DQ}\mathbf{I}_{DQ}}{2} + i_{DQ}(t)\frac{V_{DC}\mathbf{U}_{DQ}}{2} \tag{4.60}$$

where the capital letters are representing the variable in the nominal set point condition.

The scalar product and the fact that the control variable is the voltage squared are the non-linearities in the DC dynamic system. The linearisation of the

dynamic system follows the procedure presented in (4.60) and the linear state space model has state variable and input/output signals given by (4.61), (4.62) and (4.63).

$$x_{DC}(t) = \left[\frac{C_{DC}}{2}v_{DC}^2(t)\right] \tag{4.61}$$

$$\mathbf{u}_{DC}(t) = \left[\begin{array}{cccc} p_o(t) & v_{DC}(t) & \mathbf{i}_{DQ}(t) & \mathbf{u}_{DQ}(t) \end{array}\right]^T \tag{4.62}$$

$$\mathbf{y}_{DC}(t) = \left[\begin{array}{cc} v_{DC}^2(t) & v_{DC}(t) \end{array}\right]^T \tag{4.63}$$

It is necessary to mention that the converter losses are going to be treated as a non-modelled variable and its effect is not considered in the linear model. Another issue related with the model from figure 4.20 is the output vector y_{DC}. In the small signal model the control variable is given by the square of the DC link voltage. However, the value of v_{DC} is required for the completeness of the overall model.

The matrices from the linear state model for the DC voltage plant are represented by the equations written in

$$A_{DC} = \left[\begin{array}{c} 0 \end{array}\right] \tag{4.64}$$

$$B_{DC} = \left[\begin{array}{ccc} -1 & \frac{\mathbf{U}_{DQ}\mathbf{I}_{DQ}}{2} & \frac{V_{DC}\mathbf{U}_{DQ}}{2} \quad \frac{V_{DC}\mathbf{I}_{DQ}}{2} \end{array}\right] \tag{4.65}$$

$$C_{DC} = \left[\begin{array}{c} \frac{2}{C_{DC}} \\ \frac{1}{C_{DC}V_{DC}} \end{array}\right] \tag{4.66}$$

$$D_{DC} = \left[\begin{array}{ccccc} 0 & 0 & 0 & 0 & 0 \\ 0 & 0 & 0 & 0 & 0 \end{array}\right] \tag{4.67}$$

4.7 The Outer AC Voltage Control Loop

For wind applications, the HVDC converter station at the offshore side is responsible for sustain the AC voltage at the point off common coupling. For that reason the AC voltage control mode is activated. For this mode of operation the control block diagram from figure 4.3 is enabled.

In the AC voltage control mode, the PLL is not present and the two, voltage magnitude and its angle, are directly imposed by the HVDC converter in the PCC node. This control mode emulates an infinite bus viewed from the wind farms.

In this work, the offshore wind farms are modelled as current sources were its amplitude is proportional to the wind power. With this simplification of the wind power plants, the representation of the voltage source converter connected to the weak offshore grid as shown in the figure 4.21.

Figure 4.5, previously presented, illustrates basically a simplification of the AC system for the onshore converter control mode. In the onshore, due to the

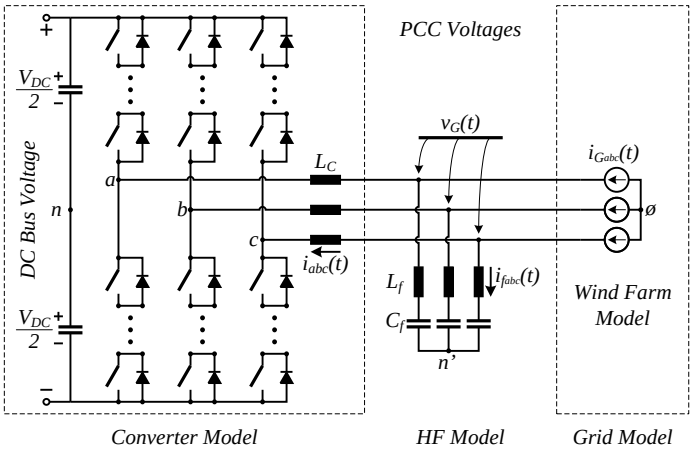

Figure 4.21: *Representation of the circuit diagram of the offshore voltage source converter station.*

emulation of an ideal voltage at the point of common coupling, some of the blocks are, consequently, removed. They are the PLL and the grid model.

The synchronisation for the voltage source converter is not allowed at the offshore station. The wind turbines have internally the ability to keep synchronised to the HVDC station and the angle is directly imposed. The grid was simplified by a pure current source with amplitude value proportional the amount of power produced by the wind power plant. Considering the mentioned simplification, the block diagram representing the main system from the offshore side is illustrated in the figure 4.22.

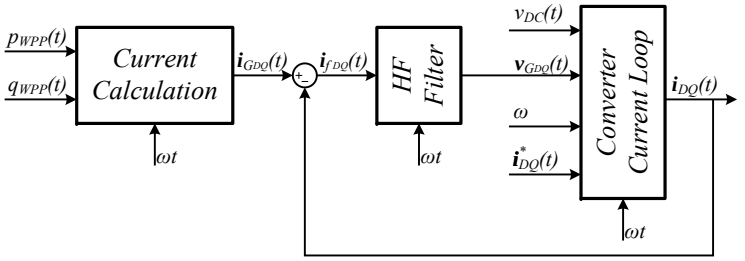

Figure 4.22: *Block diagram representation of AC converter side at offshore HVDC station.*

The current calculation block diagram representation from figure 4.22 is an algebraic loop where the input variables are the active and reactive power from the wind power plant (p_{WPP},q_{WPP}). The output representing the current vector $i_{G_{DQ}}$, in synchronous reference frame, calculated by (4.68) [44].

$$\begin{bmatrix} i_{G_D}(t) \\ i_{G_Q}(t) \end{bmatrix} = \frac{1}{v^2_{G_D}(t) + v^2_{G_Q}(t)} \begin{bmatrix} v_{G_D}(t) & -v_{G_Q}(t) \\ v_{G_Q}(t) & v_{G_D}(t) \end{bmatrix} \begin{bmatrix} p_{WPP}(t) \\ q_{WPP}(t) \end{bmatrix} \quad (4.68)$$

The equation from (4.68) represents a non-linearity in the block diagram from 4.22. Four variables represent the input vector of the system. They are the voltages in the synchronous reference frame, more two components for the active and reactive powers. The currents, in the linearised form, represent the output vector. Differently from the previous series expansion in two dimensional, the calculation of the linearised form of (4.68).

Its linearisation form is represented by (4.69) and the combination with the high frequency filter state space model (equations (4.48), (4.49), (4.50) and (4.51)) and the inner current loop form the offshore VSC-HVDC station dynamic model.

$$\begin{bmatrix} i_{G_D}(t) \\ i_{G_Q}(t) \end{bmatrix} = \frac{1}{\left(V_{G_D}^2 + V_{G_Q}^2\right)^2} \mathbb{M} \begin{bmatrix} v_{G_D}(t) \\ v_{G_Q}(t) \\ p_{WPP}(t) \\ q_{WPP}(t) \end{bmatrix} \tag{4.69}$$

where $\mathbb{M}$ is the matrix with the elements given by (4.70).

$$\begin{array}{rcrcr}
\mathbb{M}_{11} & = & -\left(V_{G_D}^2 - V_{GQ}^2\right) P_{WPP} & + & 2V_{G_D}^2 V_{GQ} Q_{WPP} \\
\mathbb{M}_{12} & = & -\left(V_{G_D}^2 - V_{GQ}^2\right) Q_{WPP} & - & 2V_{G_D}^2 V_{GQ} P_{WPP} \\
\mathbb{M}_{13} & = & & & V_{G_D}\left(V_{G_D}^2 + V_{GQ}^2\right) \\
\mathbb{M}_{14} & = & & - & V_{G_Q}\left(V_{G_Q}^2 + V_{GQ}^2\right) \\
\mathbb{M}_{21} & = & -\left(V_{G_D}^2 - V_{GQ}^2\right) Q_{WPP} & - & 2V_{G_D}^2 V_{GQ} P_{WPP} \\
\mathbb{M}_{22} & = & \left(V_{G_D}^2 - V_{GQ}^2\right) P_{WPP} & - & 2V_{G_D}^2 V_{GQ} Q_{WPP} \\
\mathbb{M}_{23} & = & & & V_{G_Q}\left(V_{G_D}^2 + V_{GQ}^2\right) \\
\mathbb{M}_{24} & = & & & V_{G_D}\left(V_{G_Q}^2 + V_{GQ}^2\right)
\end{array} \tag{4.70}$$

The combination of the equation (4.69) and the state model for the current control as well as for the high frequency filter defines the state space model for the offshore converter station. The inner current controller for this station has the same settings as the ones presented by the converter in which the DC voltage control mode was applied. Due to the weakness of the offshore grid, the high frequency filter parameters were changed. The increase in the reactive power and the decrease in the quality factor were adjusted by simulations. The parameters for the high frequency filter for the offshore converter station is presented in table 4.6 and its impedance characteristic is given in the figure 4.23.

For the PI control parameters the table 4.7 contains the settings for the tuned values of the AC voltage control loop.

4.8 VSC-HVDC Transmission Dynamic Model

The modelling process presented above was designed by spiting a larger system, represented by the voltage source converter plant and its controllers, in small pieces in which the block diagrams from figures 4.2 and 4.3 show in details the

Parameter	Value	Unit
Reactive Power	68.9	MVA
Quality Factor	5	
Notch Frequancy	1950	Hz
Inductance	784.7	μH
Capacitance	8.4	μF
Resistance	48.1	Ω

Table 4.6: *High frequency filter settings.*

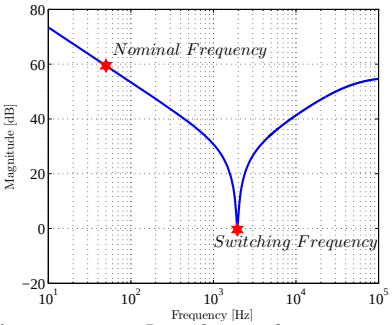

Figure 4.23: *Impedance characteristic.*

Parameter	Value	Unit
Proportional Gain	1.0	
Integral Gain	490.1	
Bandwidth	78	Hz

Table 4.7: *AC voltage PI controller parameters.*

smaller pieces. For a single-link VSC-HVDC transmission, the top level building blocks of the system are:

- Wind power plant
- Offshore AC cabling
- Offshore HVDC converter
- DC Cabling
- Onshore HVDC converter
- Grid

Grouping all the main systems itemized above, the six modules are able to describe a single-link VSC-HVDC transmission from a offshore wind park to shore by means of grid connected voltage source converter and are systematised in figure 4.1

From the modelling process performed in the previous sections in this chapter, the wind power plant was simplified using only current sources, where the amplitude of the current is directly proportional to the power delivered by the wind energy. The angle is defined by the offshore HVDC station. The modelling of the mechanical and electrical parts as well as the layout of a wind energy is not presented and focused in this work. Using this level of simplification, the wind farm and the AC cables are represented by the algebraic equation relating the electrical variables in the point of common coupling from (4.69). The AC cable between the AC collector of the wind power plant and the HVDC converter is not modelled.

The converter models were presented in the above sections. Both control modes are operative for a single link HVDC transmission. At the offshore side, the AC voltage control mode is active. With this operation mode, the offshore AC collection point is emulated such as an infinite bus for the wind turbines. For the onshore station, the DC voltage controller is activated. By this means, the DC voltage is kept constant in steady state and during transients, the control compensates the disturbance actions. The simple grid model is used for this system as well as the synchronisation method presented in the previous sections.

4.8.1 DC Cable Simplified Dynamic Model

The representation of the cable in the VSC-HVDC transmission present in figure 4.1 includes the DC submarine cables. This due to the consideration that the benchmark system is developed for offshore application. The cable modelling, however, can assume from simple modelling process (π-section approximation) to *Bergeron* and frequency dependent models.

The representation of the cable using π-section considers the connection of N modules characterized by two capacitors, one inductor and one resistor to represent the losses. The circuit diagram representation of a cable π-section is showed by figure 4.24 [48].

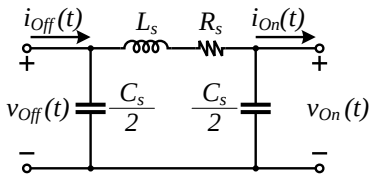

Figure 4.24: *Circuit diagram for a single π-section for cable modelling.*

Taking into account the representation of the π-section from figure 4.24, the mathematical model for such circuit can be represented by a third order differential equation. Defining the system states as the voltages at the shunt capacitors and the current in the series inductor and system inputs as the offshore and onshore DC currents, the dynamic representation of one π-section by means of state space approach is given by the equations (4.71) and (4.72).

$$\begin{bmatrix} \dot{v}_{Off}(t) \\ \dot{v}_{On}(t) \\ \dot{i}_{L_s}(t) \end{bmatrix} = \begin{bmatrix} 0 & 0 & \frac{-2}{C_s} \\ 0 & 0 & \frac{-2}{C_s} \\ \frac{1}{L_s} & \frac{-1}{L_s} & \frac{-1}{L_s} \end{bmatrix} \begin{bmatrix} v_{Off}(t) \\ v_{On}(t) \\ i_{L_s}(t) \end{bmatrix} + \begin{bmatrix} 1 & 0 \\ 0 & 1 \\ 0 & 0 \end{bmatrix} \begin{bmatrix} i_{Off}(t) \\ i_{On}(t) \end{bmatrix} \quad (4.71)$$

$$\begin{bmatrix} v_{Off}(t) \\ v_{On}(t) \\ i_{L_s}(t) \end{bmatrix} = \begin{bmatrix} 1 & 0 & 0 \\ 0 & 1 & 1 \\ 0 & 0 & 0 \end{bmatrix} \begin{bmatrix} v_{Off}(t) \\ v_{On}(t) \\ i_{L_s}(t) \end{bmatrix} + \begin{bmatrix} 0 & 0 \\ 0 & 0 \\ 0 & 0 \end{bmatrix} \begin{bmatrix} i_{Off}(t) \\ i_{On}(t) \end{bmatrix} \quad (4.72)$$

By the cascade connection of N π-sections in the system, the HVDC simplified cable model can be represented by the schematic circuit from figure 4.25.

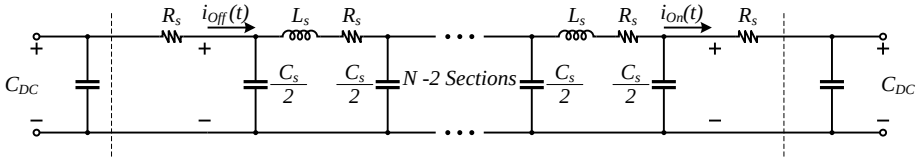

Figure 4.25: *Schematic representation of DC cable interconnection using π-sections.*

For the system representation illustrated by the figure 4.1, the parameters related to the *pi*-section circuitry elements are determined by the values represented by table 4.8.

Parameter	Value	Unit	Comment
Resistance per Unit Length	139	$m\Omega$	??
Inductance per Unit Length	159	μH	??
Capacitance per Unit Length	231	nF	??
Line Length	175	km	Assumed
Number of π Section	7		Assumed

Table 4.8: *DC cable distributed parameters.*

4.8.2 Study Cases

The validation of the HVDC system model by means of linear model is performed by comparing the EMTDC simulation results with the dynamic state space model of the system presented in figure 4.1. The complete model of the system is a combination of the modules presented in the previous sections. The system response is analysed by two main study cases: The onshore to offshore power transmission and the DC Bus voltage reference step system response.

4.8.2.1 Active Power Transmission

The active power transmission from onshore to offshore is performed by means of reduction in the wind farm power production from 0.8660 pu of power to 0.5 pu. It is considered that the wind farm production has a time constant equal to 10 ms which means that the active power cannot change instantaneously. At the offshore side, the voltages at the point of common coupling and the converter currents are illustrated by figure 4.26.

The power variation is sensed in offshore by verifying the voltages and currents in synchronous reference frame. The controller, however, is capable of maintaining the nominal values of the offshore AC voltage set point. As a consequence of power variation, the DC voltage presents a transient behaviour as well. The dynamics of the DC voltage at offside is presented in figure 4.27.

On the onshore side, the DC voltage is directly affected by the transients in the offshore DC voltage. However, at this station, the DC voltage control is

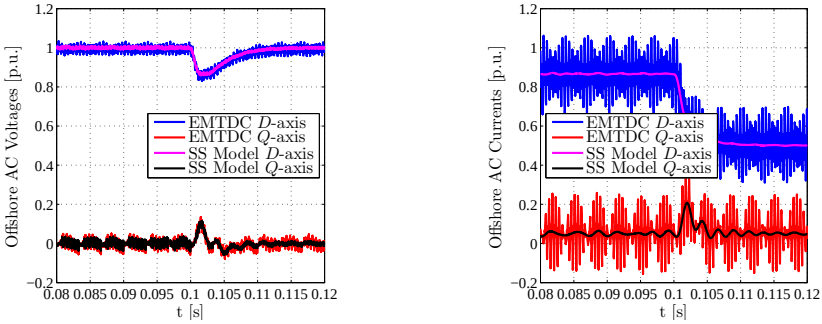

(a) AC voltages (b) AC currentss

Figure 4.26: *Voltages and currents from the offshore side converter.*

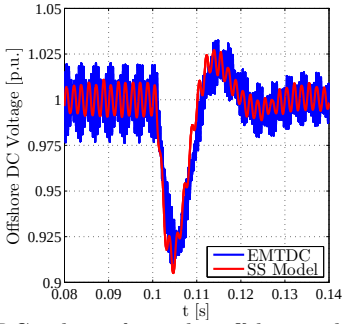

Figure 4.27: *DC voltage from the offshore side converter.*

present and in order to mitigate the response against disturbances. In the onshore station, the DC voltage dynamic performance as well as the comparison between the non-linear and the small signal dynamic model are presented in figure 4.28.

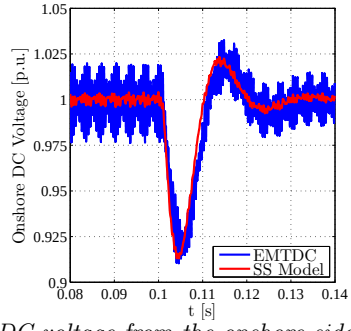

Figure 4.28: *DC voltage from the onshore side converter.*

The transient performance of the DC currents in synchronous reference frame are illustrated in figure 4.29.

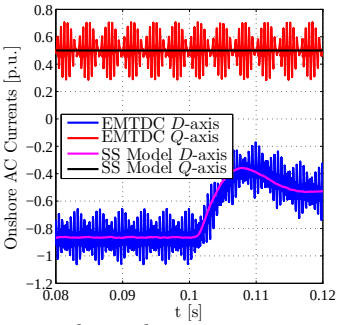

Figure 4.29: *Converter currents in the onshore station in synchronous reference frame.*

4.8.2.2 DC Bus Voltage Reference Variation

The results presented above illustrate the performance of the VSC-HVDC system under power disturbances. A different scenario can be explored when considering the DC voltage reference variation on the onshore side. By this means, the evaluation of the consequences of such change at the offshore can be performed analysing the offshore AC voltage at the point of common coupling. The results from figure 4.30 show the decoupling between the offshore AC side and the DC side perturbation. This phenomenon is related with the feedforward compensation in the current controller. The small signal model performance is also comparable with the EMTDC simulation.

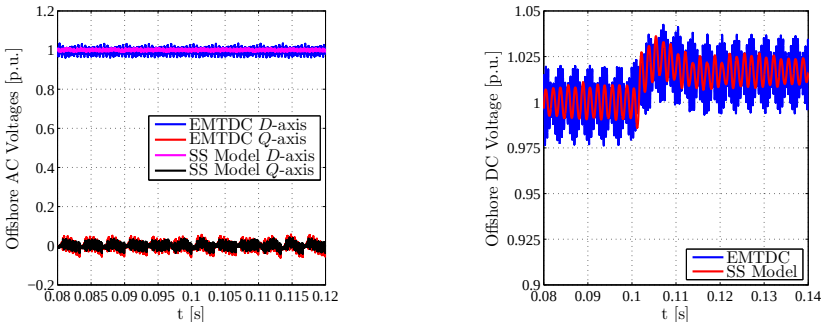

(a) AC voltages (b) DC currentss

Figure 4.30: *Offshore converter voltages at the point of common coupling and DC bus under DC voltage set point variation.*

At the onshore side, the converter presents the direct voltage control. The PI compensation is able to keep the system stable as well as promote zero error at the steady state. The overshoot and settling time can be design to lead the time response to a desired shape.

For the model validation comparison, the EMTDC model was compared with the small signal model given by the linearisation of the current and voltage loops.

The state space model of the system is provided in the main text. The dynamic behaviour of the offshore and onshore DC voltage are compared in figure 4.31.

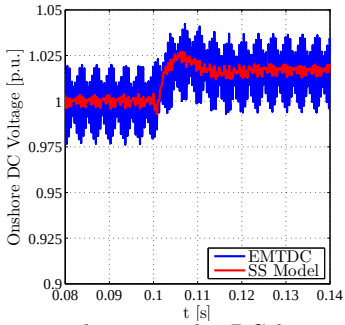

Figure 4.31: *Onshore converter voltages at the DC bus under DC voltage set point variation.*

CHAPTER 5

Robust Control Techniques Applied in DC Transmission Systems

THE energy transfer from offshore to onshore by means of HVDC is highly dependent of the controls performance. On the offshore, the weakness of the grid is a drawback for the engineering. On the onshore side, the control of DC voltage is affected by the power variations as well as by the grid conditions. In both cases, the assurance for stability is a must, and with the requirements from the grid codes, not only the stability is compulsory, but the dynamic performance of the converter is a essential role, as well.

This chapter investigates the stability and performance of the voltage source converters when they are interconnected by DC cables. The aim is to compare the stability and dynamic performance of the converter in the cases where they have classical proportional-integral controllers and robust controllers. The comparison is accomplished by means of frequency domain eigenvalue position.

First of all, an introduction about the control design and specification in the filed of robust control is presented and how the adopted control strategy (μ-synthesis) fits for high voltage DC applications. Using the linear models from the previous chapter, the eigenvalue position assessment of each of the station is evaluated considering system uncertainties such as different short circuit ratios, DC voltages and processed power.

The sensitivity of the system is tested in the complex plane by varying the parameters of the system. Both controllers, the PI and the robust control have their sensitivity compared by relating the rate of change of the position of their eigenvalues in the complex plane. The stability assessment for a point-to-point VSC-HVDC and for multiterminal case with four terminal are explored in the final sections.

5.1 General Feedback Control System Design

Automatic control is an interdisciplinary theory which has become important in the power system and in power electronics. Historically, the control theory has been divided in two main branches: classical and modern control [49]. Some authors mention post-modern categories to differentiate some recent techniques [54].

Classical control is still in use but it finds some limitations when the treatment of multiple-input multiple-output (MIMO) systems is required. Modern control theory has become popular after the $60s$ with the introduction of digital computers due to its processing power [50]. Inside modern control theory, many other section are, nowadays, part of the picture of control concepts. They are itemized below.

- Adaptive control
- Hierarchical control
- Intelligent control
- Optimal control
- Robust control
- Stochastic control

This work is based in the robust control theory and it aims for its application for grid connected voltage source converter in high voltage DC transmission. With this focus, it is possible to use the general feedback control architecture from figure 5.1.

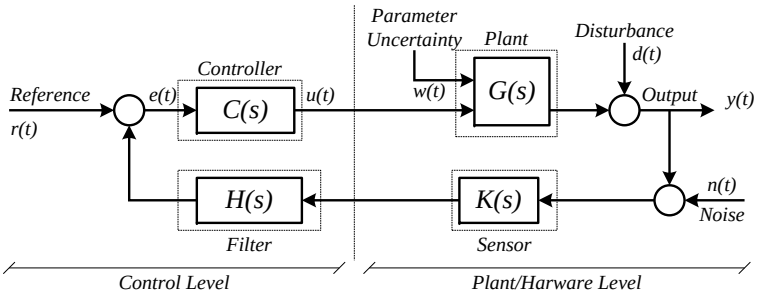

Figure 5.1: *General control architecture for a feedback dynamic system.*

The controller $C(s)$ is designed aiming for basically five performance criteria:

- Reference tracking
- Disturbance attenuation
- Noise rejection

- Less control energy
- Parameter uncertainties effect mitigation

In the classical control theory, the controller $C(s)$ can be design with the compromise among any of the four performance criteria. It is well know, however, that the emphasis in one of the them leads to depreciation of the others [51]. Moreover, the influence of the uncertainties in the nominal model is not so often considered even in some of the modern control design methods.

In a connection of voltage source converter and the utility grid, the uncertainties are confidently impose over the performance of power processing of such power electronic devices. In this case, it is possible to cite, for example, the grid AC voltage, converter DC voltage (which can vary in case of multiterminal DC connection based on droop control presented in the previous chapter) and converter processed power.

As a common practice in power system operation, the scheduling of power set points is sent to the converter station, and its control is designed considering this operating points settled by the system operators [52]. This process is made by using linearisation of the system. More than just the control design, the dynamic model of the system can assess its stability and dynamic performance.

However, even in the time frame between two consecutive set point updates, the entire power system presents variations. Those variations can be, for example, changes in the grid voltage values, load changing, and in case of wind power connection, fluctuation in the energy production by the wind farms connected to the grid. Those variations can change the properties of the system and have influence in the performance of the power delivered from the HVDC converters.

Considering a knowledge of the uncertainty and the effect of disturbances in the VSC devices, the analysis of the system using structured singular values as well as the control design by means of μ-synthesis can, intrinsically, be in accordance with uncertainty unification in the system. This enhances the performance over the gain scheduled controller, in case of small time scale, and on the same time, decrease the complexity of the system in comparison with more complex adaptive systems.

Another issue is directly related with the system performance analysis. With such methodology which quantifies the impact of the uncertainties already in the modelling process, the effectiveness of the controller and disturbance mitigation can be measured by the use of structured singular values and worst case analysis related with induced system norm [53, 54].

One chapter in the appendix shows a brief introduction about the theory and methodology adopted by μ-synthesis and analysis. There, one can find the description of uncertainty modelling procedure, linear fraction transformation as well as a summary regarding the design algorithm and optimisation process related in the control structure definition.

For the control design procedure and performance analysis of the system pre-

sented by figure 5.1, the following steps are required:

1. Modelling of the plant $G(s)$
2. Validation of the plant model
3. Modelling of uncertainties
4. Control design
5. Performance validation
6. Retuning of the control settings (if required)

The following section follows the steps presented above. The plant model uses the well known process of linearisation and small signal modelling using state space model. For the model validation, the comparison between the state space dynamic model and the EMTDC time domain simulation are evaluated for acceptance of the linear model. From the last chapter, one can find the derivation for the dynamic model for offshore and onshore converters as well as wind power plant, DC cable and grid.

The control design is a intermediate process, in which the theory behind it is refereed to [53, 54, 51]. The subitems related to control order reduction as well as weighting functions and control performance evaluation can also be found in the references.

5.2 Justification of Optimal Robust Control Design for HVDC Applications

In the interconnection of a HVDC system and a wind farm with the grid utility, the converters are able to control the variables in each the control modes are selected for: the DC voltage, in case of the onshore converter, and AC, on the offshore side. Considering for example the onshore side converter, one can divide the system in four main modules; three belonging to description of one station and the other one as the grid.

The utility grid is a combination of multiples machines, cables, transmission lines and loads. It presents a very complex dynamics, however, this work simplifies the grid behaviour by a simple Thevenin model.

For the converter viewpoint, using the grid simplification, the behaviour of the controllers inside the HVDC onshore stations are highly affected by the grid. Using the simplified Thevenin model, the stiffness and weakness of the grid can be evaluated. This characteristic can be included in the model by means of the series impedance L_G and R_G. The variation of the values of the short-circuit ration in the grid can, in some cases, emulated adversities in the grid and those

ones can affect the converter dynamics by means of variation in the voltages and currents in the point of common coupling.

In the case of a HVDC connection, looking from the DC side of the HVDC converter, the offshore system is a power source with a certain dynamics. Again, the incoming power from the offshore sides interacts with the whole rest of the system in a interconnected manner. Figure 5.2 helps to illustrates, in a simple block diagram, the interconnection among the AC side, HVDC converter and DC side.

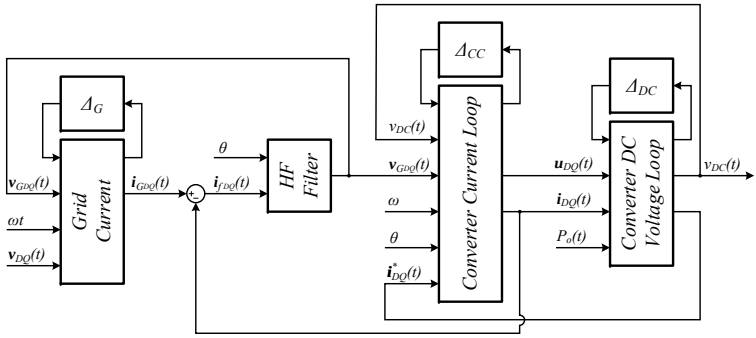

Figure 5.2: *Block diagram of the modules of onshore converter with its uncertainties.*

As a simplification manner, all the spoiled dynamics present in both, AC side and DC grid sides, can be represented as disturbances for the converter controllers. For the utility grid, for example and as it was mentioned before, the weakness and stiffness can be emulated by variations in the grid impedance.

From the models presented in the previous chapter, such values are treated as system parameters. The changes in the those parameters are modelled as model parameter variation using the block Δ_G in the figure 5.2.

Similar approach can be used for the power variations where, not only as a input disturbance for the system, but as a consideration in the operating point variation. In the linearisation process presented in the previous chapter, the operating point was crucial in the determination of some parameter values and the variation of such conditions can be sensitive to the converter controllers.

The representation of the system according to the figure 5.2 can drive the attentions to a method in the modern control theory called μ-synthesis where similar framework is te basic approach for design robust control for system under uncertainties.

Uncertainty in control systems assigns to the model imperfections as well as different forms of disturbances in which a system can be under effect. The former represents the discrepancies between the nominal mathematical model and the real physical system. For the current application, the variations the grid impedances and operating points. The last case references to the unpredictable nature of the disturbance bounded inputs. One can refer to power variations, for example. The trade-off represented by the uncertainty modelling in the classical

control theories are, nowadays, solved by new control techniques based on the optimal robust techniques, in case, the μ-synthesis.

5.3 Robust Control: Design and Specification

The adopted control design method presents the advantage in simplify some dynamics of the system by means of system parameter variation and bounded input disturbances. The design method requires details in optimisation techniques related with non-convex optimisation, linear fraction transformation, structured singular values and system norms. Those concepts are commonly used in modern control technique and cab be found in [53] and [54]. Details regarding implementation are described in [51]. Few definitions and brief details are given in the appendix. The objective of this is work is to to concentrate the efforts in methods for the control design, but simplify the description of the dynamics of a complex system and apply a robust technique to improve the converter dynamics.

The process of the μ-synthesis lies on the principle of output feedback control. The main objective is find a controller $C(s)$ such that the performance of the system, considering the plant and the uncertainties, is satisfied for determined range of variation of the uncertainty block Δ. Figure 5.3.

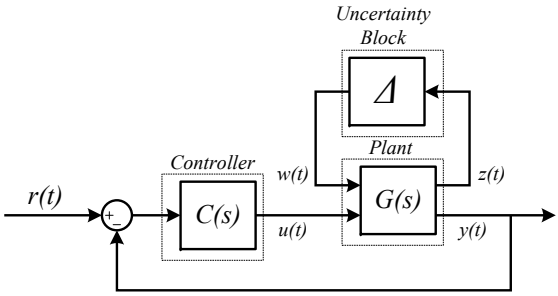

Figure 5.3: *Simplified representation of feedback system with augmented plant.*

The preliminary step is describe the augmented plant in terms of input/output state space model considering the uncertainty block Δ. This representation is an extension of state space model of the system including the inputs $w(t)$ and outputs $z(t)$ related to the uncertainty block. This characterisation of the dynamic system is written in equations (5.1), (5.2) and (5.3).

$$\dot{\mathbf{x}}(t) = A\mathbf{x}(t) + B_1\mathbf{z}(t) + B_2\mathbf{u}(t) \tag{5.1}$$
$$\dot{\mathbf{z}}(t) = C_1\mathbf{x}(t) + D_{11}\mathbf{z}(t) + D_{12}\mathbf{u}(t) \tag{5.2}$$
$$\dot{\mathbf{y}}(t) = C_2\mathbf{x}(t) + D_{21}\mathbf{z}(t) + 2_{22}\mathbf{u}(t) \tag{5.3}$$
$$\tag{5.4}$$

According to (5.4), the matrices A, B_2, C_2 and D_{22} belong to the nominal

state space model for the plant $G(s)$ with no uncertainties.

With the uncertainty model described in the mathematical form from (5.4), it is necessary to determine the performance specification. This stage is direct related to the requirements derived from the grid prerequisites, standards and codes. In the robust optimal control, the specification is translated to the optimisation by means of weight functions which can be scalar, transfer functions and even additional dynamic systems.

The choice of the weight functions is, usually, the drawback in the design process [51]. The trial and error is some times the unique solution, however, in some cases there are methods for designing the functions. The direct method for inspection, method, is though, used for define the performance criteria for the high power converter in the HVDC connection. For all the control loops the same methodology is applied. Few parameters change in order to fulfil the requirements. Generally, two weight transfer functions are included in the system, one for the reference tracking performance and another included to filter and bound the control command. They are, respectively W_p and W_u. Figure 5.4 shows the uncertainty plant been controlled by the augmented controller with integral additional integral action and the position of the weighting functions for the design.

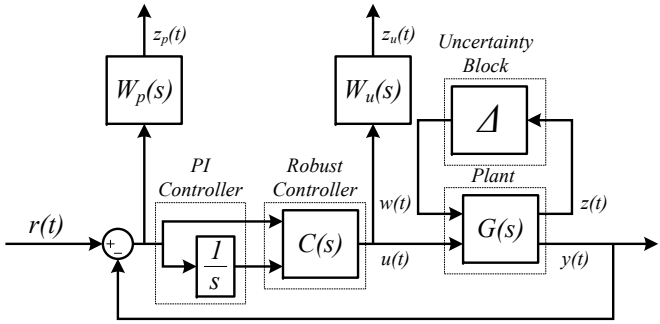

Figure 5.4: *General robust weighting architecture for the design of robust control by means of μ-synthesis.*

The first weight function W_p shapes the time response of the error. Into it, the requirements regarding settling time and damping factor are specified. The PI controller is included just after the error calculation for guaranteeing zero error at the steady state as well as alleviates the iteration process during the control design optimisation.

The output of the control command is weighted as well. This function is applied to put the constraints in the optimisation such that the control effort to achieve the specification requirements have low control energy. For the switched devices, in addition, this function can be design with filtering characteristics. For the current controller for example, the weight function can have a cut-off frequency such that the command signal will not face double crossings in the modulator.

The final stage is the control optimisation algorithm where the state space

model of the controller is obtained. The objective function describes the seek for a controller $C(s)$ such that the $\mathscr{H}_\infty$-norm of the augmented system structured singular values of the transfer matrix between the outputs z_p and z_u and the inputs is minimised. In layman's words, the $\mathscr{H}_\infty$-norm represents the worst case performance that a system can present. The structure singular values, are in a way, related to the eigenvalues of the state space dynamic system considering the range of variation in the uncertainty matrix Δ.

This optimisation process requires iterations, usually the $D-K$ iterative process [53] and , first of all, do not guarantee uniqueness of the solution due to the non-convexity of the system. Another disadvantage is that it does not guarantee convergence.

5.3.1 Uncertainty Model

The uncertainties are intrinsic in the main blocks from figure 4.5. The considered uncertainties for the dynamic system are input voltages and the short circuit ratio (representation of stiffness of the grid), for the grid current dynamic block; active and reactive power for the converter current block and grid frequency can present variation, as well. For quantitative analysis, the voltages, SCR and converter DC voltages and processed powers are considered to vary according to the values presented by table 5.1.

	Uncertainty Value	Variable
Grid AC Voltage	±10%	$\delta_{V_{AC}}$
Grid frequency	±1%	δ_w
Grid SCR	7 to 3	δ_{L_G} and δ_{R_G}
DC Voltage	±3%	$\delta_{V_{DC}}$
Converter Power	±25%	δ_P and δ_Q

Table 5.1: *Parameter uncertainties for current loop analysis.*

5.3.2 The Inner Loop with Uncertainties

From figure 5.2, the uncertainty matrices are the representation of the variations in the system. For the inner current controller viewpoint, the uncertainties are going to be reflected in variations the power transfer set point. Due to the possibility to measure disturbances, the performance of the inner current controller against disturbances is improved by the feedforward compensation. As a result, the model of the inner current controller considering the uncertainties ca be considered such as is illustrated in figure 5.5.

The uncertainty from the DC voltage value is the unique variational block present, since that it is considered the feedforward action. Such condition where considering the DC voltage variation is a prediction for multiterminal connection, since, in this kind of system topology the changes in the DC voltage are present.

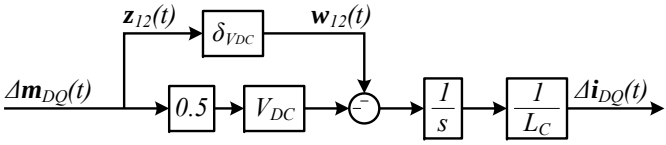

Figure 5.5: *Simplified block diagram of the inner current plant with uncertainties.s*

Assuming the model from figure 5.5, the augmented state space model with system uncertainties is given by equations (5.5), (5.6) and (5.7)

$$\dot{\mathbf{x}}_{DQ}(t) = \begin{bmatrix} 0 & 0 \\ 0 & 0 \end{bmatrix} \mathbf{x}_{DQ}(t) + [-1]\, \mathbf{w}_{DQ}(t) + \begin{bmatrix} -V_{DC} \\ 2 \end{bmatrix} u_{DQ}(t) \tag{5.5}$$

$$\mathbf{z}_{DQ}(t) = \begin{bmatrix} 0 & 0 \\ 0 & 0 \end{bmatrix} \mathbf{x}_{DQ}(t) + [0]\, \mathbf{w}_{DQ}(t) + [1]\, u_{DQ}(t) \tag{5.6}$$

$$\mathbf{y}_{DQ}(t) = \begin{bmatrix} \frac{1}{L_C} & 0 \\ 0 & \frac{1}{L_C} \end{bmatrix} + [0]\, \mathbf{w}_{DQ}(t) + [0]\, u_{DQ}(t) \tag{5.7}$$

5.3.3 DC Voltage Loop with Uncertainties

The DC voltage model considers the variations in power transfer from the AC to DC side or vice versa. In the model, the uncertainty of the DC voltage controller is direct connected to the power variations. By this means, the δ components of the uncertainty matrix Δ have the uncertainties in voltage and currents processed by the converter station. Figure 5.6 illustrates the DC voltage plant model for the DC loop plant model with the system uncertainties.

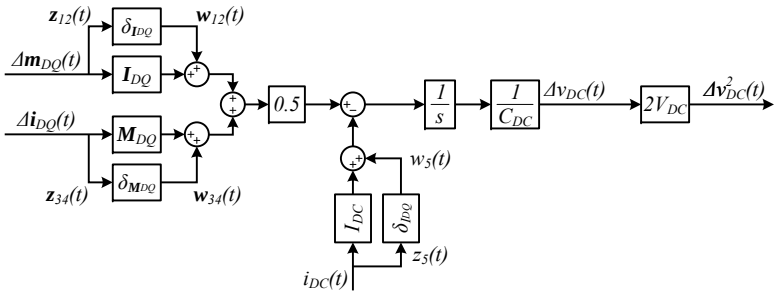

Figure 5.6: *DC voltage loop plant considering the uncertainties in the model.*

At the AC side of the converter, the range of variation of the current in the synchronous reference frame, i_{DG}, is a result of variations in the power and voltages at the power of common coupling. The DC current value, is then, a combination of the modulation indexes and currents. The modulation indexes considerer the feedforward components as well. By the linearised block diagram from figure 5.6, the state space model which includes the uncertainties of the DC loop plant is given by (5.8), (5.9) and (5.10)

$$\dot{x}_{DC}(t) = [0]\, x_{DC}(t) + \begin{bmatrix} 0.5 & 0.5 & 0.5 & 0.5 & -1 \end{bmatrix} \mathbf{w}_{DC}(t) + \begin{bmatrix} M_D & M_Q & I_D & I_Q & -1 \end{bmatrix} \mathbf{u}_{DC}(t) \quad (5.8)$$

$$\mathbf{z}_{DC}(t) = [0]\, x_{DC}(t) + \begin{bmatrix} 0 & 0 & 0 & 0 & 0 \end{bmatrix} \mathbf{w}_{DC}(t) + \begin{bmatrix} 1 & 1 & 1 & 1 & 1 \end{bmatrix} \mathbf{u}_{DC}(t) \quad (5.9)$$

$$y_{DC}(t) = \left[\frac{1}{C_{DC}}\right] x_{DC}(t) + \begin{bmatrix} 0 & 0 & 0 & 0 & 0 \end{bmatrix} \mathbf{w}_{DC}(t) + \begin{bmatrix} 0 & 0 & 0 & 0 & 0 \end{bmatrix} \mathbf{u}_{DC}(t) \quad (5.10)$$

5.3.4 AC Voltage Loop with Uncertainties

The control of the voltage at the AC side of the converter i required at the offshore station. As the same uncertainty variable presented in the DC voltage control loop, the power variation is the uncertainty for the system where the AC voltage control mode is the compensation strategy.

Indirectly presented in the model, the uncertainty is power is reflected in the model by means of consideration in the voltage and current level in the converter model. The voltage is the control variable, and the AC currents are the input disturbances. By then, the uncertainties are included the disturbance input as a definition of the variational variable which serves as input for the robust control design algorithm. Figure 5.7 illustrates the uncertainty plant model for the AC voltage loop of the converter station.

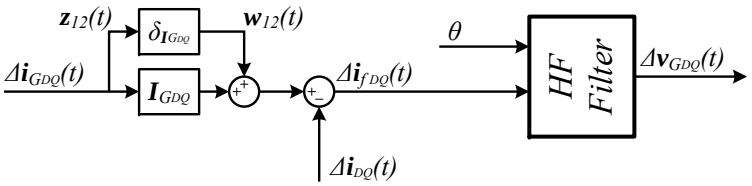

Figure 5.7: *AC voltage loop plant considering uncertainties in the system.*

The augmented plant model presented in figure 5.7 have the state model, model with the framework from the equation (5.4). The dynamic state space equation model is represented by the state space equation of the high frequency filter in (4.47).

5.4 Control Design Performance Specification

5.4.1 Inner Current Control Loop

The performance specification for the inner current controllers from the offshore and onshore converter have the same parameters. The first criterion is

regarding reference tracking. For this purpose, the extra integrator was included in the loop to guarantee zero error in steady-state. This action suppress the necessity in forcing the optimisation algorithm in finding an optimal controller such that there is a integrator in its structure. In some cases, more constraints in the optimisation process can drive the algorithm to divergence.

The second consideration in the control design for the converters AC currents are related with the settling time. Due to the limitation in bandwidth, the current controller is set to have 390 Hz of bandwidth. This value is five times less than the switching frequency and guarantee compensation for lower harmonics, if required. The damping factor is chosen to be $\frac{1}{\sqrt{2}}$.

The last specification considers the filtering and saturation prediction of the control command error. The first is required for the proper modulation performance and the former, guarantees that the converter operates at the considered linear region. All the requirements are summarised in table 5.2.

Parameter	Value	Unit	Comment
Bandwidth	390	Hz	Assumed
Damping Factor	$\frac{1}{\sqrt{2}}$		Assumed
Filter Bandwidth	975	Hz	Assumed
Control Command Saturation Gain	1.0		Assumed

Table 5.2: *Summary of the requirements specified for the current control robust design.*

For the robust control design, the specification presented in table 5.2 can be translated to weight functions. For the performance specification, the W_p function is selected and for the control command compensation W_u. Each of the objectives related with the specification requirements are itemized below:

W_p: Performance weight function with high gains in low frequency for the reference tracking performance. The settling time is defined by the bandwidth set by the cut-off frequency. The damping is also specified by the loop shape of the function.

W_u: Weight for the control output command guarantees saturation avoidance and filtering of the high harmonic contents. This action is required to assure the absence of double crossings in the modulator.

The frequency response of the selected weight functions are illustrated by the bode plots presented in figures 5.8(a) and 5.8(b).

5.4.2 DC and AC Outer Voltage Control Loops

For the onshore converter the DC voltage control loop is present while in the offshore sites the AC voltage control loop promotes voltage support to the connection with the wind farms. The connection between the outer controllers and the inner current control is design such that the dynamic decoupling is assured.

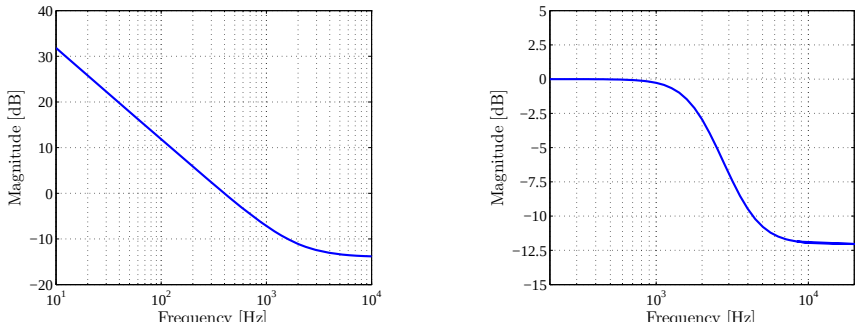

(a) Reference tracking (W_p). (b) Control Command (W_u).

Figure 5.8: *Weighting functions for the performance specifications in the inner current controller.*

For the outer loop control specification, the weight functions for the control design have the same frequency response presented in figures 5.8(a) and 5.8(b). However, different parameters define the settling times and control command weights.

For simplification in the design and simulations, it is considered that all the voltage source converters in the same are sized with the same parameters presented in table 4.1 and 4.2. Both, outer loops, the DC and AC voltage loops, are considered to have the same specification which is described in table 5.3.

Parameter	Value	Unit	Comment
Badwidth	78	Hz	Assumed
Damping Factor	$\frac{1}{\sqrt{2}}$		Assumed
Filter Bandwidth	390	Hz	Assumed
Control Command Saturation Gain	1.0		Assumed

Table 5.3: *Summary of the requirements specified for the current control robust design.*

5.5 Control Performance Comparison in a Point-to-Point VSC-HVDC Transmission

The previous chapter presented the results of the model validation in a point-to-point HVDC connection. There, the accuracy of the model was tested against the EMTDC simulations. The effort in making a precise state space model lies on the advantage in the allowance in the assessment of the frequency domain analysis of the dynamic system.

The usage of the state space model derived previously allows the frequency domain analysis by means of robust performance and system sensitivity. The first considers the evaluation of the eigenvalue position in the complex plane. The damping and eigenvalue frequencies define the main characteristic the dynamic

performance.

The sensitivity analysis is related with system parameter variations. The evaluation of the system operating point and how the changes in its parameters can affect the stability performance is defined by the rate of eigenvalue position variation.

5.5.1 Model Performance under Active Power Variation

In the point-to-point transmission case, the control of power is directly performed by the wind power plants. The HVDC links acts a corridor. For this study case, the performance of the HVDC controllers are evaluated by means of disturbance rejection, since, the incoming power is modelled with such behaviour.

In the offshore shore side, the stiffness of the AC voltage control promotes better operation conditions for the wind turbines connected by the AC collection. The performance under the input power disturbances is a reasonable of the control quality.

At the offshore side, the power variation promotes changes in the DC voltage which directly affects the current controller states. The limited range of operation of a HVDC converter is a key point for determination of the final cost of the system. Allowing the operation of the DC voltage in higher DC levels requires more costly converter station. The second point is related with the DC cables which are, as well, sensitive to voltage operating conditions.

For this study case, a point-to-point HVDC connection transmission system presents two operating conditions. The initial case consider the classical PI controller. The second case makes use of the robust control design by means of the μ-synthesis. The test case consider a initial condition for the offshore power deliver at 0.8660 *pu* of active power. At the onshore operation the reactive current reference is set to be 0.5 *pu*. At the offshore side, the AC voltages have their time domain simulation response given by figure 5.9.

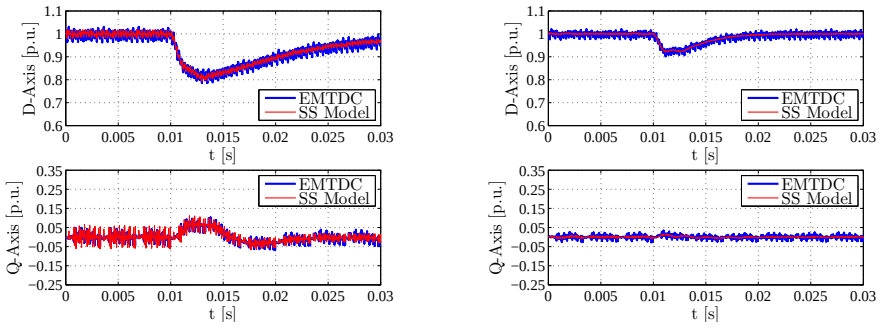

(a) AC voltage PI controller performance (b) AC voltage robust controller performance

Figure 5.9: *Control performance evaluation for wind power variation.*

The three main characteristics between the figures 5.9(a) and 5.9(b) are related to the deepest point, settling time and overshoot. The performance of the robust boosted the dynamics of the system. The overshoot, which can affect the sizing of the offshore components, is highly improved by the robust controller as a combination of fast current controller and higher order control characteristic.

The DC voltages for the offshore and onshore sides play a very important role in the operation of the HVDC system. The DC voltage controller, as previously mentioned, is placed at the onshore converter controller. By this means, the loose control at the onshore side converter can compromise the operation of the offshore converter. Due to the non-controllability of the offshore DC voltage and also due to the effect of the DC cable dynamic the converter, the DC voltage at the sending-end converter is directly under influence of the onshore converter station. The improvements presented by the robust control in the DC voltage compensation is illustrated by the time domain simulation from figure 5.10.

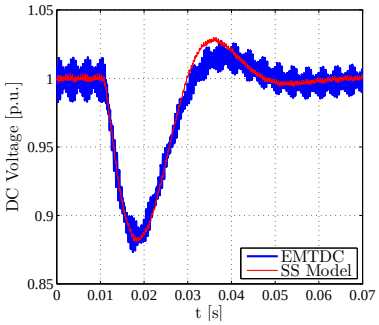

(a) Onshore DC voltage PI controller performance

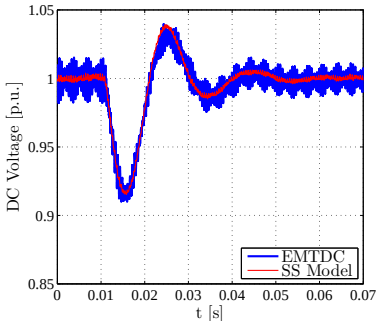

(b) Onshore DC voltage robust controller performance

Figure 5.10: *Control performance evaluation for wind power variation.*

The refined controller promoted by the onshore DC voltage controller is directly measured by the overshoot mitigation during the transient condition. The settling time between the response of the classical PI controller and the robust augmented controller are approximately the same.

At the offshore side, the improvements in overshoot voltage is as well improved. The time domain simulation results for the offshore side converter station are illustrated by the figure 5.11.

5.5.2 Model Performance under DC Reference Variation

The DC voltage reference changes in a HVDC transmission is a previous study for predicting the roust performance of the HVDC system in the multiterminal connection. The evaluation of the robust control over the proportional-integral compensator are presented in figure 5.12.

As the same improvements presented for disturbance rejection in the previous

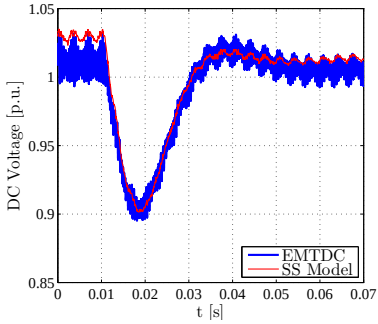

(a) Offshore DC voltage PI controller performance

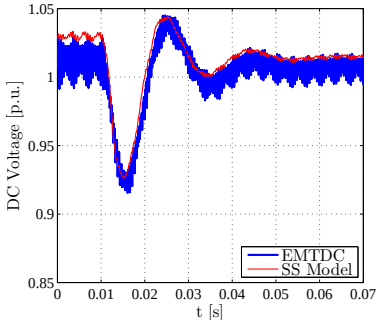

(b) Offshore DC voltage robust controller performance

Figure 5.11: *Control performance evaluation for wind power variation.*

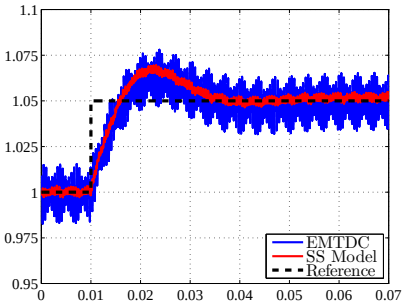

(a) Onshore DC voltage PI controller performance

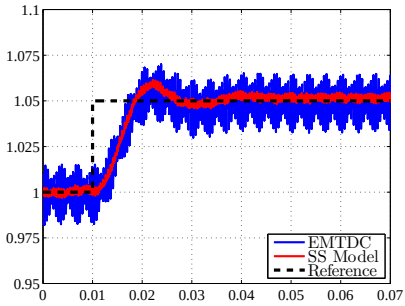

(b) Onshore DC voltage robust controller performance

Figure 5.12: *Control performance evaluation for wind power variation.*

case, the robust controller could better track the reference. The settling time does not present significant improvements in both of the cases. The main contribution that makes the robust controller a better candidate is related with the overshoot mitigation. While the overshoot rate from the PI controller is around 30 to 40%, the robust controller performance presents a overshoot close to 5%.

5.5.3 System Performance under Grid Impedance Variation

The grid impedance variation is a test study which aims to be a preliminary assessment for grid faulted conditions. The variation in the short circuit ratio of the system can emulate the changes in the interconnected utility grid such as line trips for example.

The analysis is performed using the EMTDC simulation. The system is initially operation at 0.8660 *pu* of active power. At the onshore operation the reac-

tive current reference is set to be 0.0 *pu*. The grid impedance present a sudden change which reflects a variation of the short ratio from 7 to 3. The simulation results which consider this scenario are shown in figure 5.13.

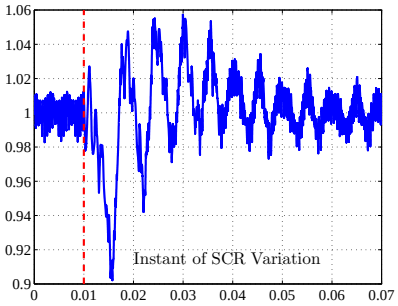

(a) DC voltage time domain simulation for PI Controller.

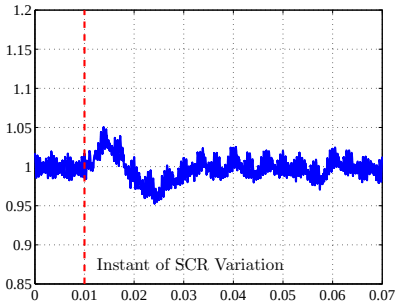

(b) DC voltage time domain simulation for Robust Controller.

Figure 5.13: *DC voltage time response for variation in the utility grid short circuit ratio.*

The variation of the grid impedance clearly affects the DC voltage. The robust controller performance is, again, higher in comparison which the PI controller. The effect of the grid impedance variation is, as well, promoted by the performance of the synchronisation loop presented in the phase-locked loop. The influence of the synchronism delay effect of the phase-lock loop is not evaluated in this work.

Conclusions

The increase in size and power capacity of the wind turbines and the wind availability in the sea sites, moved the wind farms from the land to offshore. This action forced the seek for new technologies which could be able to transmit the bulk amount of energy. Due to the lack of reactive power compensation and loss levels, the HVDC solution came to overcome the traditional HVAC. Allied with the developments in the power semiconductors and converter topologies, the voltage source converters are able to provide this interconnection between the wind farms and shore by means of DC.

This possibilities in linking more than one wind farms and more than one grid utility using HVDC is an envisage and the static analysis presented in first the part of this work proposed a methodology for operating a DC network by means of droop control. The optimisation algorithm is applied in a classical load flow technique and depending on the determination of the cost function, the functionality of the multierminal DC system can fulfil some requirements of the grid utilities.

The main results are based in the choice of two main objectives: loss minimisation an dispatch optimisation. In the minimisation of losses, the cable models were simplified and the loss model of the two-level converter were included in the iterative method. In the dispatch problem, the classical revenue quadratic cost function is tested against the minimisation of the dispatch error. The advantage in limiting the error between the scheduled dispatch in the last case is compared with the improvements in operating the system with smaller losses in the first case.

The dynamic viewpoint in a HVDC transmission is provided by means of small signal analysis of the converter. The operation of the control modes, one for onshore and the other for offshore, were modelled and the results were comparable with the time domain simulations provided by the EMTDC model. The modelling part is a important stage for the derivation of the complete model of the converter plant, since the control definition is highly dependent of the model accuracy when it is connected with the real system.

The simplification of the dynamics of the system using structure uncertainty models and its use for the robust design of the converter controllers presented promising benefits. The main test cases are able to demonstrate the improvements in the dynamic operation of a point-to-point VSC-HVDC system under transient conditions.

Nowadays, many options are available for the robust control design. The μ-synthesis is one them. The control design in this work, by itself, does not presented novelties related with algorithm developments. The contribution states in the definition of the weight function for the design. Usually, such task involves trial and error process.

The study of variation in the power delivered from the wind farms, the voltage reference order variation as well as grid impedance deviations are tested. The first case consider a real scenario predicting the variability of the wind behaviour. The second case gives insights regarding the possibilities of multiterminal connection. In this case, the connection with the static optimisation is in the fact that the changes in the DC voltage references, in one of the stations in the DC grid, acts as disturbance for the other converters where the droop controllers are in operation.

The changes in the grid impedance emulates the possible discrepancies in the conditions of the utility grid. Line tripping is one of the possible real cases which can endorse the accomplished study. The results are able to show that the augmented controller, design by means of μ-synthesis performs in a better condition than the classical PI controller.

Main Contributions

In the operation of a multiterminal VSC-HVDC, some control methods are proposed in the literature. The droop control is one of them and it was selected to be the most attractive candidate. This work proposed an optimisation algorithm to defined the droop factors in a multiterminal DC connection. The methodology is based in an optimisation technique where some requirements can be set in the initial states of the operation and the advantages are in accordance to loss minimisation, including cables and converter, as well as revenue maximisation and dispatch error minimisation. Depending on the scenario selected to the system operators, one of the cost functions can be selected and the droop factors are calculated according the settled requirements.

For the dynamic studies, the modelling of converter uncertainties and its integration in the control design were presented. The concept of the use of structured singular values was included in the voltage source converter model in order to simplify some of the dynamic properties of the grid and offshore wind power plants. The use of weight functions in the robust design framework was simplified by the used of selected weight functions. Due to the characteristics of the control and operation of the voltage source converter, the proposed weighting can be used as a standard method for VSC applications.

Future Work

The dynamic behaviour of the converter under disturbances effect is a important role for a point-to-point connection. In a multiterminal DC system, the droop controller can act was well for dynamic improvements. The droop factor can be extended by another dynamic system where, for the static viewpoint, the gain is determined by the optimisation algorithm analysed in this work and the dynamic properties are used to mitigate the disturbances of the system. The robust design can be applied into this scenario as control method design.

The modular multilevel converter is the current state-of-art in the high power high voltage market. Its dynamics is different from the two level case. It is possible to operate such system with higher bandwidth, however, the effect of the dynamics of the internal controllers in the system dynamics is still not clear.

The use of the simplified uncertainty models in the power system can be extended to the operation of the HVDC and multiterminal HVDC systems under faulted conditions. DC faults and AC grid faulted conditions can be explored. The results from the large signal analysis can be translated to the robust control framework.

List of published papers:

P1: Da Silva, R.; Teodorescu, R.; Rodriguez, P.; *Power Delivery in Multiterminal VSC-HVDC Transmission System for Offshore Wind Power Applications;* In: Proceedings of the IEEE Innovative Smart Grid Technologies Conference Europe (ISGT Europe), PES 2010 . IEEE Press, 2010.

P2: Stan, A. I.; Stroe, D. I.; Da Silva, R.; *Control strategies for VSC-based HVDC transmission system;* In: Proceedings of the 2011 IEEE International Symposium on Industrial Electronics (ISIE). IEEE Press, 2011. p. 1387-1392.

P3: Da Silva, R.; Teodorescu, R.; Rodriguez, P.; *Multilink DC Transmission System for Supergrid Future Concepts and Wind Power Integration;* In: Proceedings of the Power Generation Conference 2011. Institution of Engineering and Technology, 2011.

P4: Craciun, B. I.; Da Silva, R.; Teodorescu, R.; Rodriguez, P.; *Multilink DC Transmission for Offshore Wind Power Integration;* In: Proceedings of the 21st 2012 IEEE International Symposium on Industrial Electronics (ISIE). IEEE Press, 2012. p. 1894-1899.

P5: Sztykiel, M.; Da Silva, R.; Teodorescu, R.; Zeni, L.; Helle, L.; Kjaer, P. C.; *Modular Multilevel Converter Modelling, Control and Analysis under Grid Frequency Deviations;* In: Proceedings of the EPE Wind Energy and T& D Seminar 2012.

P6: Da Silva, R.; Chaudhary, S. K.; Teodorescu, R.; Rodriguez, P.; Annakkage, U.; *Optimal Operation of Multiterminal VSC-HVDC Based Transmission Systems for Wind Power Application;* Submitted in: IEEE Transaction on Power Delivery.

Bibliography

[1] P. Bresesti, W. Kling, R. Hendriks, and R. Vailati, "HVDC connection of offshore wind farms to the transmission system," *Energy Conversion, IEEE Transactions on*, vol. 22, pp. 37 –43, Mar. 2007.

[2] P. Bresesti, W. Kling, and R. Vailati, "Transmission expansion issues for offshore wind farms integration in europe," in *Transmission and Distribution Conference and Exposition, 2008. T #x00026;D. IEEE/PES*, pp. 1 –7, Apr. 2008.

[3] F. Nozari and H. Patel, "Power electronics in electric utilities: HVDC power transmission systems," *Proceedings of the IEEE*, vol. 76, pp. 495 –506, Apr. 1988.

[4] M. Aredes, A. F. C. Aquino, and G. Santos Jr, "Multipulse converters and controls for HVDC and FACTS systems," *Electrical Engineering (Archiv fur Elektrotechnik)*, vol. 83, no. 3, pp. 137–145, 2001.

[5] V. K. Sood, *HVDC and FACTS Controllers: Applications of Static Converters in Power Systems*. Springer, 1 ed., May 2004.

[6] M. Bahrman, "HVDC transmission overview," in *Transmission and Distribution Conference and Exposition, 2008. T #x00026;D. IEEE/PES*, pp. 1 –7, Apr. 2008.

[7] A. Chattopadhyay, "Alternating current drives in the steel industry," *Industrial Electronics Magazine, IEEE*, vol. 4, pp. 30 –42, Dec. 2010.

[8] B. Wu, *High-Power Converters and AC Drives*. Wiley-IEEE Press, 1 ed., Mar. 2006.

[9] I. Colak, E. Kabalci, and R. Bayindir, "Review of multilevel voltage source inverter topologies and control schemes," *Energy Conversion and Management*, vol. 52, pp. 1114–1128, Feb. 2011.

[10] N. Flourentzou, V. Agelidis, and G. Demetriades, "VSC-Based HVDC power transmission systems: An overview," *Power Electronics, IEEE Transactions on*, vol. 24, pp. 592 –602, Mar. 2009.

[11] A. Nabae, I. Takahashi, and H. Akagi, "A new neutral-point-clamped PWM inverter," *Industry Applications, IEEE Transactions on*, vol. IA-17, pp. 518 –523, Sept. 1981.

[12] A. Lesnicar and R. Marquardt, "An innovative modular multilevel converter topology suitable for a wide power range," in *Power Tech Conference Proceedings, 2003 IEEE Bologna*, vol. 3, p. 6 pp. Vol.3, June 2003.

[13] S. Katoh, S. Ueda, H. Sakai, T. Ishida, and Y. Eguchi, "Active-gate-control for snubberless IGBTs connected in series," in *Power Electronics Specialists Conference, 2002. pesc 02. 2002 IEEE 33rd Annual*, vol. 2, pp. 609 – 613 vol.2, 2002.

[14] J. Pou, R. Pindado, and D. Boroyevich, "Voltage-balance limits in four-level diode-clamped converters with passive front ends," *Industrial Electronics, IEEE Transactions on*, vol. 52, pp. 190 – 196, Feb. 2005.

[15] G. Adam, S. Finney, A. Massoud, and B. Williams, "Capacitor balance issues of the diode-clamped multilevel inverter operated in a quasi two-state mode," *Industrial Electronics, IEEE Transactions on*, vol. 55, pp. 3088 –3099, Aug. 2008.

[16] M. Hagiwara and H. Akagi, "PWM control and experiment of modular multilevel converters," in *Power Electronics Specialists Conference, 2008. PESC 2008. IEEE*, pp. 154 –161, June 2008.

[17] A. Antonopoulos, L. Angquist, and H.-P. Nee, "On dynamics and voltage control of the modular multilevel converter," in *Power Electronics and Applications, 2009. EPE '09. 13th European Conference on*, pp. 1 –10, Sept. 2009.

[18] R. Marquardt, "Modular multilevel converter: An universal concept for HVDC-Networks and extended DC-Bus-applications," in *Power Electronics Conference (IPEC), 2010 International*, pp. 502 –507, June 2010.

[19] K. Friedrich, "Modern HVDC PLUS application of VSC in modular multilevel converter topology," in *Industrial Electronics (ISIE), 2010 IEEE International Symposium on*, pp. 3807 –3810, July 2010.

[20] G. Mondal, R. Critchley, F. Hassan, and W. Crookes, "Design and simulation of a modular multi-level converter for MVDC application," in *Industrial Electronics (ISIE), 2011 IEEE International Symposium on*, pp. 200 –205, June 2011.

[21] H.-J. Knaak, "Modular multilevel converters and HVDC/FACTS: a success story," in *Power Electronics and Applications (EPE 2011), Proceedings of the 2011-14th European Conference on*, pp. 1 –6, Sept. 2011.

[22] C. Barker and N. Kirby, "Reactive power loading of components within a modular multi-level HVDC VSC converter," in *Electrical Power and Energy Conference (EPEC), 2011 IEEE*, pp. 86 –90, Oct. 2011.

[23] L. Harnefors, A. Antonopoulos, S. Norrga, L. Angquist, and H. Nee, "Dynamic analysis of modular multilevel converters," *Industrial Electronics, IEEE Transactions on*, vol. PP, no. 99, p. 1, 2012.

[24] Wikipedia contributors, "Super grid," July 2012.

[25] N. Ahmed, A. Haider, D. Van Hertem, L. Zhang, and H.-P. Nee, "Prospects and challenges of future HVDC SuperGrids with modular multilevel converters," in *Power Electronics and Applications (EPE 2011), Proceedings of the 2011-14th European Conference on*, pp. 1 –10, Sept. 2011.

[26] D. Van Hertem and M. Ghandhari, "Multi-terminal VSC HVDC for the european supergrid: Obstacles," *Renewable and Sustainable Energy Reviews*, vol. 14, pp. 3156–3163, Dec. 2010.

[27] S. Chaudhary, R. Teodorescu, P. Rodriguez, and P. Kjar, "Chopper controlled resistors in VSC-HVDC transmission for WPP with full-scale converters," in *2009 IEEE PES/IAS Conference on Sustainable Alternative Energy (SAE)*, pp. 1 –8, Sept. 2009.

[28] D. Jovcic, D. van Hertem, K. Linden, J.-P. Taisne, and W. Grieshaber, "Feasibility of DC transmission networks," in *2011 2nd IEEE PES International Conference and Exhibition on Innovative Smart Grid Technologies (ISGT Europe)*, pp. 1 –8, Dec. 2011.

[29] J. H. BJORN JACOBSON, "Proactive hybrid HVDC breakers - a key innovation for reliable HVDC grids," in *Proceedings on The Electric Power System of the Future - Integrating Supergrids and Microgrids International Symposium*, (Bologna, Italy), Cigre, Sept. 2011.

[30] M. Merlin, T. Green, P. Mitcheson, D. Trainer, D. Critchley, and R. Crookes, "A new hybrid multi-level voltage-source converter with DC fault blocking capability," in *9th IET International Conference on AC and DC Power Transmission, 2010. ACDC*, pp. 1 –5, Oct. 2010.

[31] Y. Phulpin and D. Ernst, "Ancillary services and operation of multi-terminal HVDC grids." http://orbi.ulg.ac.be/handle/2268/101095, Oct. 2011.

[32] B. Johnson, R. Lasseter, F. Alvarado, and R. Adapa, "Expandable multiterminal DC systems based on voltage droop," *IEEE Transactions on Power Delivery*, vol. 8, pp. 1926 –1932, Oct. 1993.

[33] L. Xu, L. Yao, and M. Bazargan, "DC grid management of a multi-terminal HVDC transmission system for large offshore wind farms," in *International Conference on Sustainable Power Generation and Supply, 2009. SUPERGEN '09*, pp. 1 –7, Apr. 2009.

[34] R. Pinto, S. Rodrigues, P. Bauer, and J. Pierik, "Comparison of direct voltage control methods of multi-terminal DC (MTDC) networks through modular dynamic models," in *Proceedings of the 2011-14th European Conference on Power Electronics and Applications (EPE 2011)*, pp. 1 –10, Sept. 2011.

[35] S. Boyd and L. Vandenberghe, *Convex Optimization*. Cambridge University Press, Mar. 2004.

[36] J. Beerten, S. Cole, and R. Belmans, "A sequential AC/DC power flow algorithm for networks containing multi-terminal VSC HVDC systems," in *Power and Energy Society General Meeting, 2010 IEEE*, pp. 1 –7, July 2010.

[37] G. Daelemans, K. Srivastava, M. Reza, S. Cole, and R. Belmans, "Minimization of steady-state losses in meshed networks using VSC HVDC," in *Power Energy Society General Meeting, 2009. PES '09. IEEE*, pp. 1 –5, July 2009.

[38] M. Bierhoff and F. Fuchs, "Semiconductor losses in voltage source and current source IGBT converters based on analytical derivation," in *Power Electronics Specialists Conference, 2004. PESC 04. 2004 IEEE 35th Annual*, vol. 4, pp. 2836 – 2842 Vol.4, 2004.

[39] B. Ooi and X. Wang, "Voltage angle lock loop control of the boost type PWM converter for HVDC application," *IEEE Transactions on Power Electronics*, vol. 5, pp. 229 –235, Apr. 1990.

[40] L. Harnefors, *On Analysis, Control and Estimation of Variable-speed Drives*. 1997.

[41] L. Zhang, L. Harnefors, and H.-P. Nee, "Power-synchronization control of grid-connected voltage-source converters," *IEEE Transactions on Power Systems*, vol. 25, pp. 809 –820, May 2010.

[42] A. Yazdani and R. Iravani, *Voltage-Sourced Converters in Power Systems*. Wiley, 1 ed., Feb. 2010.

[43] A. G. , "ABB BorWin1 - ABB HVDC reference projects in europe," July 2012.

[44] H. Akagi, E. H. Watanabe, and M. Aredes, *Instantaneous Power Theory and Applications to Power Conditioning*. Wiley-IEEE Press, 1 ed., Mar. 2007.

[45] A. Ghoshal and V. John, "A method to improve PLL performance under abnormal grid conditions." http://eprints.iisc.ernet.in/12985/, 2007.

[46] "IEEE guide for planning DC links terminating at AC locations having low short-circuit capacities," *IEEE Std 1204-1997*, p. i, 1997.

[47] A. Nassif, W. Xu, and W. Freitas, "An investigation on the selection of filter topologies for passive filter applications," *IEEE Transactions on Power Delivery*, vol. 24, pp. 1710 –1718, July 2009.

[48] C. H. Chien and R. Bucknall, "Analysis of harmonics in subsea power transmission cables used in VSC #x2013;hvdc transmission systems operating under steady-state conditions," *IEEE Transactions on Power Delivery*, vol. 22, pp. 2489 –2497, Oct. 2007.

[49] G. F. Franklin, J. D. Powell, and A. Emami-Naeini, *Feedback Control of Dynamic Systems*. Prentice Hall, 6 ed., Oct. 2009.

[50] K. Ogata, *Modern Control Engineering*. Prentice Hall, 5 ed., Sept. 2009.

[51] D.-W. Gu and P. H. Petkov, *Robust Control Design with MATLABÂ®*. Springer, 2005 ed., Aug. 2005.

[52] P. Kundur, *Power System Stability and Control*. McGraw-Hill Professional, Jan. 1994.

[53] K. Zhou, J. C. Doyle, and K. Glover, *Robust and Optimal Control*. Prentice Hall, 1 ed., Aug. 1995.

[54] K. Zhou and J. C. Doyle, *Essentials of Robust Control*. Prentice Hall, 1 ed., Oct. 1997.

[55] G. J. Balas, "Robust control of flexible structures: theory and experiments." http://resolver.caltech.edu/CaltechETD:etd-10252002-160528, 1990.

[56] J. Doyle, A. Packard, and K. Zhou, "Review of LFTs, LMIs, and mu;," in *, Proceedings of the 30th IEEE Conference on Decision and Control, 1991*, pp. 1227 –1232 vol.2, Dec. 1991.

APPENDIX A

Model Validation

This appendix presents details regarding the validation of the linear model of voltage source converter presented in the main text. The model validation follows the following structure:

- Model validation of the AC current loop of the voltage source converter using proportional-integral controller
- Model validation of the DC voltage control loop by means of proportional-integral compensation
- Model validation of the AC voltage control with a PI controller

A.1 Inner Current Controller with Classical PI Controller

This section shows the comparison between the state space model and the EMTDC model of the inner current loop of the voltage source converter. The current loop has basically three blocks. The plant, the PI controller and the feedforward compensation. The synchronisation structure represented by the PLL is an extra control loop. Figure 4.5 represents the main block structures in which the AC current system can be split for the modelling process.

In the inner current controller the conditions to be analysed are the response to a step variation in the references of currents in the synchronous reference frame axis and the effect of the disturbances over the system performance. The disturbance for the inner controller are the AC and DC voltages as well as the coupling effect due to the *Park's Transformation*.

The system parameter values are all included into the table A.1.

Parameter	Value	Unit	Comment
Grid Voltage	150	kV	Line-to-line RMS
Grid Frequency	50	Hz	
Nominal SCR	5		Assumed
SCR Angle	80	Degrees	Assumed
Nominal D-axis Current	0.8660	pu	Assumed
Nominal Q-axis Current	-0.50	pu	Assumed
AC Current Feedback Gain	375μ		$k_{i_{AC}}$
AC Voltage Feedback Gain	6.67μ		$k_{v_{AC}}$
DC Voltage Feedback Gain	3.33μ		$k_{v_{DC}}$
AC Current Feedforward Gain	0.0178		$k_{FF_{i_{AC}}}$
AC Voltage Feedforward Gain	1.0		$k_{FF_{v_{AC}}}$
DC Voltage Feedforward Gain	1.0		$k_{FF_{v_{DC}}}$
Current Controller Proportional Gain	1.0		$k_{P_{i_{AC}}}$
Current Controller Integral Gain	2450		$k_{I_{i_{AC}}}$

Table A.1: *Parameters values for the AC current model validation.*

A.1.1 Response to the Reference Step Variation

The time domain simulation considers the PI controller. The step response from the current references in both, direct and quadrature axes, changes the D-axis from 0.8660 *p.u.* to 0.50 *p.u.* at 33.3 *ms* and from 0.50 *p.u.* to zero in the quadrature one at 66.6 *ms*. On figure A.1 one can find the step response of the AC current in SRF for reference variation mentioned above.

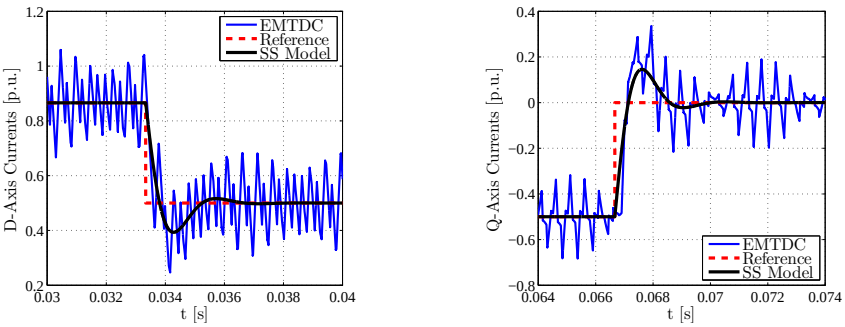

(a) D-axis (b) Q-axis

Figure A.1: *DQ-axes currents for reference step variation.*

The EMTDC simulation shows the switching effect as well the tracking behaviour due to the PI controller. Despite the effect of the current ripple, the state space linear model presents similar dynamics compared with the non-linear simulations. The time domain response of the system currents in *abc*-frame is performed by the EMTDC simulations and they are illustrated in figure A.2(a). The modulation indexes are placed in sequence into the figure A.2(b).

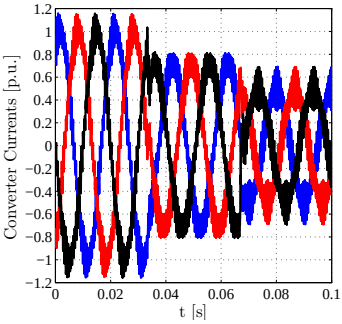

(a) EMTDC results for *abc* converter currents

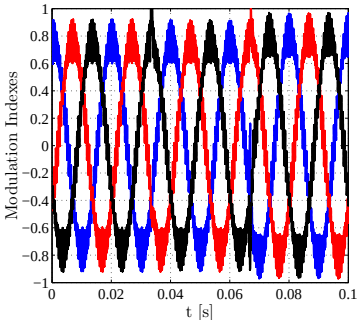

(b) EMTDC results for *abc* converter currents

Figure A.2: *Converter currents and modulation indexes for EMTDC simulation.*

For the tracking effort analysis, the error signals are evaluated in figure A.4. After the transient response, the error in both, D and Q-axes are kept zero in average. The presence of the integral action allows such phenomena.

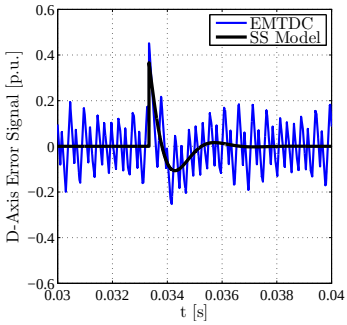

(a) D-axis

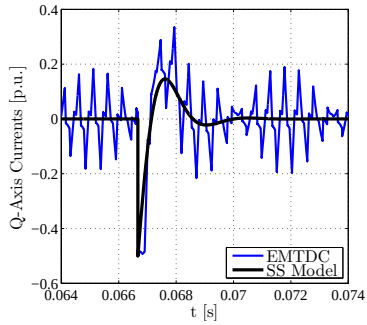

(b) Q-axis

Figure A.3: *DQ-axes currents for reference step variation.*

The switching effect and the absence of filtering in the current feedback measurement carries the high harmonic components. The carrier based pulse-width modulation (PWM), requires, however, proper proprieties of the input signals to avoid double crossing in the rising and falling edges of the triangular carrier. The verification of the non-existence of double crossings during the transients in the currents are illustrated in figure A.4.

The high harmonic content present in the current which pass through the phase reactor is a result of the switching effect. The main component of the current waveform is sinusoidal with frequency equal to the nominal grid voltage (50 Hz). The other main components are integers of the switching frequency (1950 Hz). Figures A.5(a) and A.5(b) shows, respectively, few cycles of the converter currents in steady-state as well as the harmonic content of the current in the phase a of the converter reactor L_C.

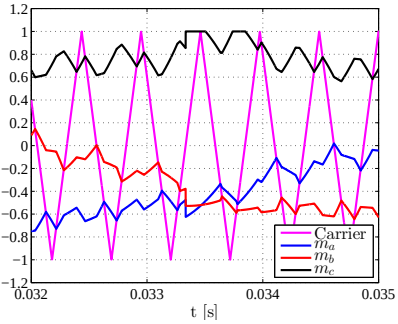

(a) Double crossing checking for D-axis reference current step variation.

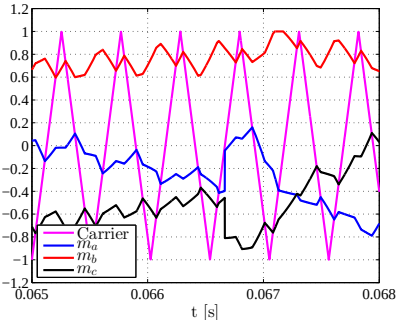

(b) Double crossing checking for D-axis reference current step variation.

Figure A.4: *Verification of modulation double crossing for grid current reference step response.*

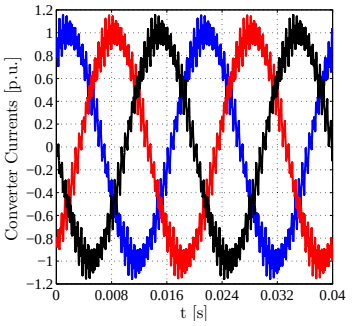

(a) Converter currents in steady-state.

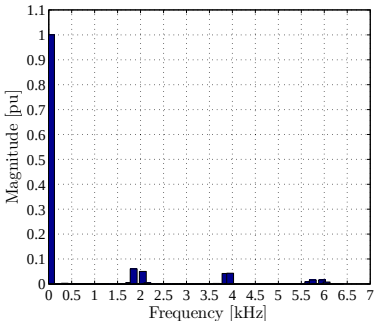

(b) Harmonic spectrum of the converter currents.

Figure A.5: *Harmonic analysis of the converter phase reactor currents.*

A.1.2 Coupling Effect and Feedforward Performance

The synchronous reference frame given by the *Park's Transformation*, promotes the decoupling of the zero sequence as well as promotes the advantage of using a coordinate system where the coordinates are constant values in steady-state. However, the differential equations, when transformed from abc to ϕdq-frame, usually, present a coupling effect given by the relationship of one coordinate to another.

The equations of the state space model for the current control in the main text has explicitly showed the relationship between the D and Q-axis currents. The feedforward term is commonly used in real applications to overtake such relationship. The effectiveness of the feedforward can be validated by means of signal checking. For the same simulation case from the last section, where the reference tracking had the performance evaluated, the PI command signals and

the output of the feedforward can be compared. Figure A.6 shows the D and Q-axis PI outputs and, on the same time, the feedforward output signal.

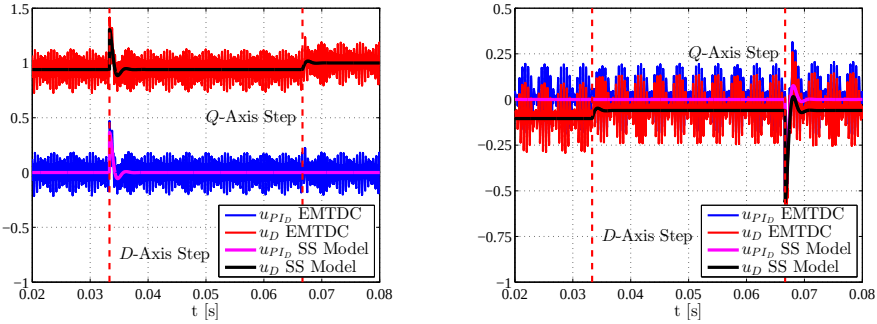

(a) PI output signal for D-axis reference step variation

(b) PI output signal for Q-axis reference step variation

Figure A.6: *Coupling effect comparison by means of visualisation of control signals.*

The output the PI controllers given by the labels $u_{PI_{DQ}}$ are just affected during the transient in their own axis components. On the other hand, the control signals which are going to be applied in the modulator u_{DQ} present transitory behaviour during transients in opposite components as well. The small signal model is able to provide the same behaviour as the EMTDC non-linear simulation shows, not considering, however, the high frequency content.

A.1.3 DC Voltage Variation Effect

Presenting an input port in the small signal linear model of the converter AC current plant, the DC voltage is also included in the complete control model by means of feedforward compensation. The linearisation required by the completeness of such feedback path is shown in the main text as well as the linear model. This appendix shows the disturbance rejection of the current control loop under DC voltage variations.

The effectiveness of the feedforward loop is evaluated using the procedure adopted in the validation of decoupling DQ current network presented above. For the DC voltage disturbance effect, the D-axis current control block which presents the majority influence, since the disturbances in the DC voltages are directly connected to the active power.

For the dynamic simulation, it was considered a variation of the DC voltage from 300 kV to 330 kV, which represents a disturbance of 10% from the nominal value. The instant of time in which the disturbance was injected in the system was 50 ms. The simulation results with the time response of the PI controller as well as the control command with the influence of the feedforward is showed in figure A.7.

From figure A.7 it is possible to verify that all the effect of the disturbance is

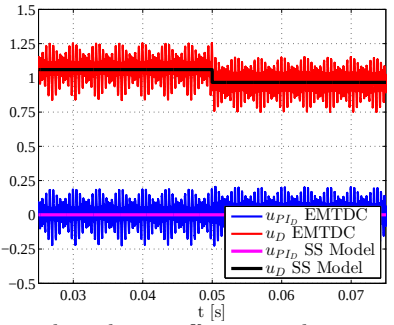

Figure A.7: *DC voltage disturbance effect over the current converter controllers.*

completely lead by the feedforward compensation since the PI control signal u_{PI_D} does not present any action over the DC voltage variation. The same performance is guaranteed in the small signal linear model.

A.1.4 AC Voltage Variation Effect

The last feedforward control input component is the AC voltage. The direct measurement of the voltage at the converter terminals at the point of common coupling is used as infeed signals for the feedforward compensation in the AC current control loop. The performance of such component is similar to the ones presented by the decoupling as well as by the DC voltage feedforward compensation. The performance of the AC feedforward loop is showed in figure A.8. For the voltage variation, just the amplitude was considered. Later results show the effect of the changes in the grid angle. However for this case, the synchronisation must be considered in the model.

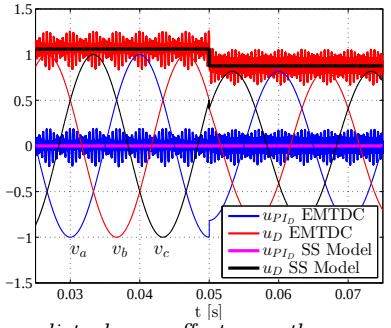

Figure A.8: *AC voltage disturbance effect over the current converter controllers.*

The variation in the amplitude of the AC voltage at the point of common coupling is directly compensated by the AC feedforward loop present in the converter AC current controller. The PI controller, clearly, does not sense such effect.

A.2 DC Voltage Outer Loop

The modelling process presented in the main text considered as a state related to the DC link capacitor the energy storage in such passive element. By this means, this control feedback loop promotes an energy regulation system for the DC link. The parameters of the PI controller used for the validation of the DC energy regulation system is presented by the table A.2.

Parameter	Value	Unit	Comment
DC Voltage Controller Proportional Gain	1.0		$k_{P_{v_{DC}}}$
DC Voltage Controller Integral Gain	2450		$k_{I_{v_{DC}}}$

Table A.2: *Parameters values for the DC voltage model validation.*

From figure 4.20 and through the equation written in (4.57), the DC voltage can be affected by DC voltage reference variation as well as due to disturbances in the DC link model as power exchanging. For the reference tracking evaluation performance of the state space model, the converter reference is kept constant up to the time 50 *ms*. At this moment the DC voltage reference is ordered to change from 1 *pu* to 1.03 *pu*. The time response of both systems, the one from the EMTDC platform and the state space model, are illustrated by the DC voltage waveforms as well as by the AC current in *D*-axis variation.

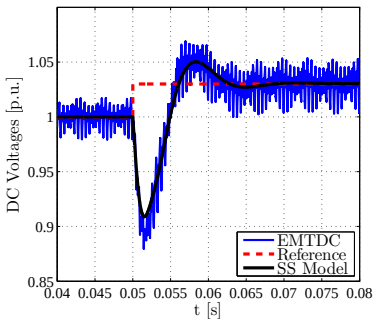

(a) DC voltage response to the the power infeed step variation

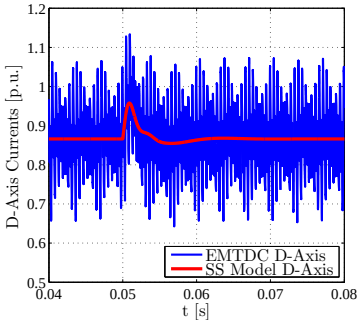

(b) DQ-axes currents for DC voltage reference step response

Figure A.9: *Step response performance for DC voltage reference variation.*

The power infeed in the DC grid is evaluated by adding a DC current source whose magnitude is proportional to the power order. The model validation considers that the HVDC converter has the operating power point at 0.5 *pu* active power. On the same time, the reactive power reference is set to be 0.5 *pu*. At the instant 50 *ms*, the power command changes the reference from 0.5 *pu* to 0.8660 *pu*. The results comparing the EMTDC time domain simulation and the state space linearised dynamic model is showed by the DC voltage variation at the DC bus and *DQ*-axes currents present by figure A.10.

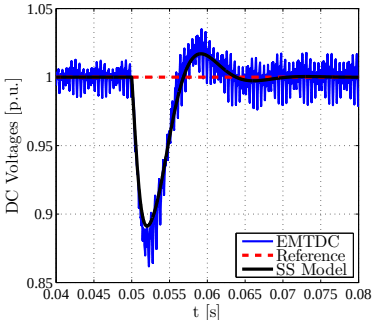

(a) DC voltage response to the power infeed step variation

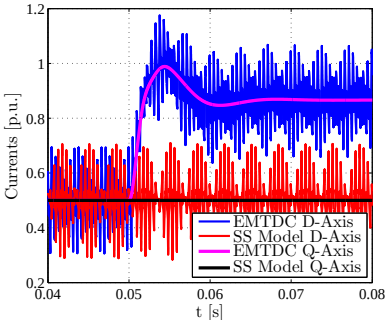

(b) DQ-axes currents for the power infeed step variation

Figure A.10: *Step response performance for DC voltage reference variation.*

A.3 AC Voltage Outer Loop

For the offshore side, the voltage at the point of common coupling is directly defined by the HVDC converter by means of direct voltage control at that bus. The purpose of such control mode (offshore control mode) is make an emulation of an infinite bus. The feedback control is based in a proportional-integral compensator with the parameters illustrated by table A.3.

Parameter	Value	Unit	Comment
DC Voltage Controller Proportional Gain	1.0		$k_{P_{v_{AC}}}$
DC Voltage Controller Integral Gain	490.1		$k_{I_{v_{AC}}}$

Table A.3: *Parameters values for the AC voltage model validation.*

For the offside, the wind power plant is modelled as a power source where the amplitude of the currents are proportional active and reactive power reference settings. The calculation of the current components in synchronous reference frame follow the instantaneous power theory [44]. For the wind power model, the reference for active power changes in a time constant equal to 10 ms and the reactive power can be changed instantaneously.

A.3.1 Step Response to the Reference AC Voltage Variation

The dynamics of the AC voltage controller can be visualized by means of step response of under reference variation. This simulation scenario refers to a variation of the D-axis component of the offshore PCC voltage reference by means on decrease 10% of its nominal value of 150 kV. The time of application of the step is at 50 ms. The dynamics of the AC voltages as all as the AC currents are illustrated in figure A.11.

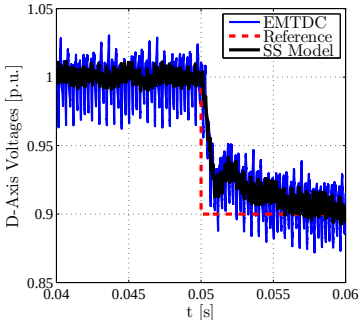

(a) D-axis voltage for offshore voltage reference step response.

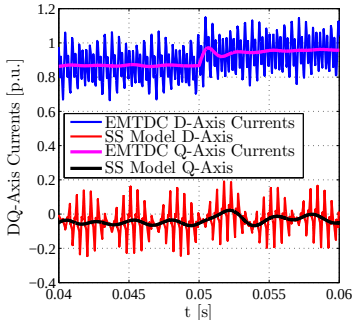

(b) DQ-axes currents for offshore voltage reference step response.

Figure A.11: *Voltages and currents in synchronous references at the offshore HVDC converter station.*

For the voltage waveform at the point of common coupling, one can analyse the amplitude and frequency of the voltage using EMTDC time domain simulation . The harmonic spectrum of such variables can be derived from each of the components in *abc*-fram. The AC voltage wave forms at the point of common coupling in the offside and the harmonic spectrum of one of the system voltages are illustrated in figure A.12.

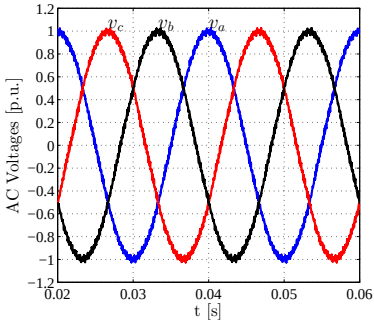

(a) Converter AC voltages in steady-state.

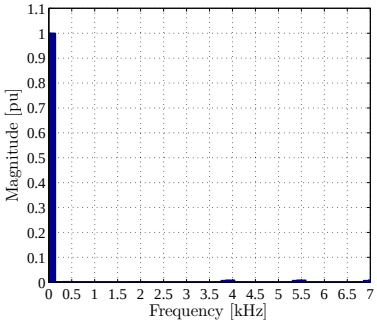

(b) Harmonic spectrum phase a voltage.

Figure A.12: *Harmonic analysis of the converter AC voltages at offshore station.*

A.3.2 Step Response to the Wind Power Variation

Controlling the offshore VSC-HVDC station in voltage control mode allows the wind farms to run freely according to wind availability. The verification of such condition is simulation in EMTDC and using the linearised model present in the main text. The simulation considers a wind production reduction from 0.8660 *pu*os active power to 0.5 *pu* with time constant of 10 *ms*. The results

showing the time domain comparison among the non-linear EMTDC model as well as the state space model for the offshore side are presented in figure A.13.

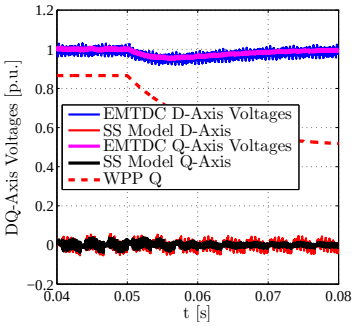

(a) Voltage at the PCC for the reduction in the wind farm energy production

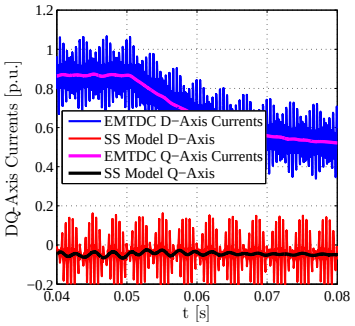

(b) Converter currents for the reduction in the wind farm energy production

Figure A.13: *Simulation comparison between the EMTDC time domain simulation and the linearised state space model for wind power production variation.*

A.3.3 Step Response to the Wind Power Reactive Power Compensation

The weakness of the offshore grid is an important issue for controlling properly the voltage at the point of common coupling. The wind farms, when considering full-scale converters as turbine conversion devices, are able to operate compensation reactive power according to grid requirements. This action helps the offshore converter in maintaining the offshore grid voltage. For the modelling purpose, it is considered that the wind farms can fully support reactive power. The simulation comparison between the EMTDC simulation platform and the state space model of the offshore converter side considers constant wind production of 0.866 *pu* of active power and variation of wind farm reactive power from 0.1 *pu* to 0.3 *pu* at the instant of time equal to 50 *ms*. This change is considered to be a step change. The results for such scenario is showed in figure A.14.

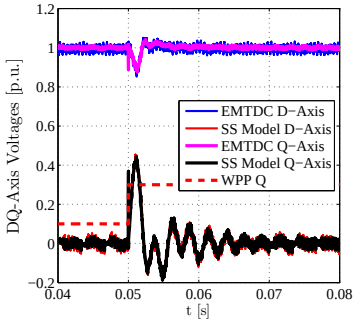

(a) Converter currents for the variation in the wind farm reactive power support

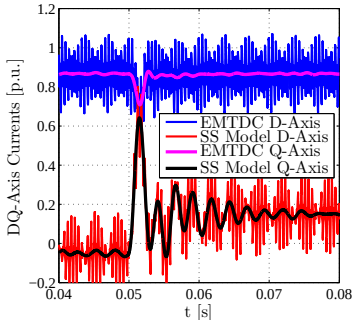

(b) Converter currents for the variation in the wind farm reactive power support

Figure A.14: *Simulation comparison between the EMTDC time domain simulation and the linearised state space model for wind power reactive power compensation.*

APPENDIX B

Introduction to Optimal Robust Control

B.1 Concepts

In layman's terms, the robustness of the system from the figure 5.1 can be defined as the amount of the variation of the parameter uncertainty and size of the disturbance and noise signals for which the system remains stable.

Stability is a crucial requirement in any feedback system. One can stand in the need of certain performance level of the feedback system even whether the uncertainties and disturbances are included. By performance specification the criteria of settling time, damping factor, phase margin, rise time, maximum overshoot, are considered.

Usually, the controller $C(s)$ is designed for the purpose of tracking the reference signal, and, it is desired, that, on the same time, the effect of the parameter uncertainties, disturbance and measurement noise are attenuated. It is well known, however, that satisfying both sensitivity (output variation under effect of the parameter uncertainties, disturbance and noise) and reference tracking is an infeasible problem [53].

So the performance specification of the system, e.g., tracking error, time response and maximum overshoot, can be satisfied for certain range of variation of the uncertainties and disturbances. By then, robust performance can be defined as the amount of variation of the uncertainties such that the system remains stable and satisfy some of the performance criteria specified in the beginning of the control design.

In optimal control theory, some techniques have been discussed in the literature regarding using optimal controllers which have the optimal criteria based on the minimisation of the impact of disturbances and uncertainties over the output response [53, 54]. One of the tools presented by such theory is the μ-synthesis.

This technique aims to minimise the structured singular values of a dynamic

system where the uncertainties are included in the model in a structured form. Details in this approach can be found in the references [53, 54, 51]. The following sections describes, briefly the uncertainty modelling using the structured form as well as the control synthesis. The method is then applied in the control of voltage source converters as a possible control technique to reduce the sensitivity of the system under disturbance effects.

B.2 Uncertainty Model

The uncertainties in the system representation from figure 5.1 can be classified into disturbance signals and dynamic perturbations [51]. The first case can be exemplified by changes in power and variation of the grid voltage and frequency in a grid connected voltage source converter. The last case consider the disparity between the nominal model and the actual dynamics due to parameter variations.

Some of the uncertainties in the system that may occur can be grouped into one single perturbation block. For the present analysis, two main uncertainty types are considered: the additive perturbation and inverse additive perturbation. Both cases are illustrated in figure B.1.

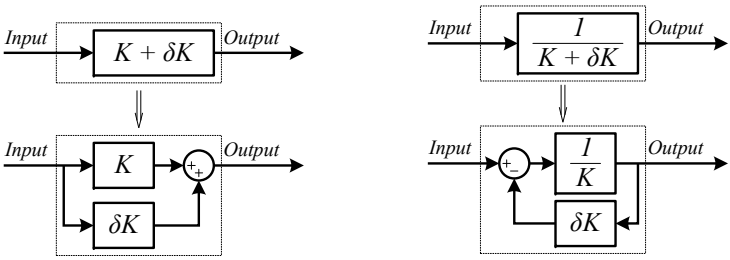

(a) Additive (b) Incerse additive

Figure B.1: *Additive and inverse additive uncertainty types.*

Considering a general dynamic system M, and a set of parameters from M such that the uncertainties can be structured using the formulation in figure B.1, the standard configuration for representing the nominal system and its structured uncertainty block Δ is represented in figure B.2.

where Δ is a diagonal matrix such that, $\Delta = diag\{\delta_1, \delta_2, \ldots, \delta_n\}$, and δs are the uncertainties of the model.

The interconnection transfer function matrix M from figure B.2 can be fractionated such as (B.1).

$$M = \begin{bmatrix} M_{11} & M_{12} \\ M_{21} & M_{22} \end{bmatrix} \tag{B.1}$$

It is defined as upper *Linear Fraction Transformation* (LFT) of M, the matrix

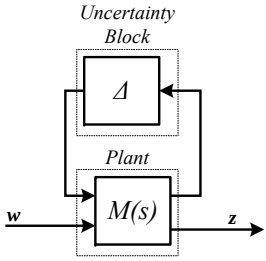

Figure B.2: *Standard representation of dynamic systems with structured uncertainties.*

equation given by (B.2).

$$\mathscr{F}_u(M,\Delta) \quad = \quad \left[M_{11} + M_{21}\Delta\left(\mathbf{I} - M_{11}\Delta\right)^{-1} M_{12}\right] \tag{B.2}$$

where $\mathbf{I}$ is the identity matrix.

As a generalisation of the concept of singular value decomposition, which can be used for constant matrices, the structured singular values are able to deal with matrices where the elements of the matrix can vary in a predefined range. The definition of the calculation of structured singular values is written in figure (B.3).

$$\mu_\Delta\left(M(s)\right) \quad = \quad \frac{1}{min\left\{\bar{\sigma}(\Delta) : det\left(\mathbf{I} - M(s)\right) = 0, \text{ is structured}\right\}} \tag{B.3}$$

The value of $\bar{\sigma}$ comes from the small gain theorem, briefly written in (B.4).

$$\frac{1}{\alpha_{max}} \quad := \quad \|\Delta\|_\infty = \sup_{s\in\mathbb{C}_+} \bar{\sigma}\left(M(s)\right) = \sup_{\omega} \bar{\sigma}\left(M(j\omega)\right) \tag{B.4}$$

The small gain theorem states that the maximum size of Δ, in terms of $\mathscr{H}_\infty$-norm, is the supreme value of $\bar{\sigma}$ such that the feedback system remains marginally stable.

B.3 Control Synthesis and Performance

Considering the block diagram from figure 5.1, and the signals $r(t)$, $u(t)$, $d(t)$ and $y(t)$ as the reference signal, control signal, disturbance signal and the output signal, respectively, the relationship among them and the state space models from the block diagram are given by (B.5), (B.6) and (B.7)

$$y(t) \quad = \quad \left(\mathbf{I} + GCHK\right)^{-1} GCr(t) + \left(\mathbf{I} + GCHK\right)^{-1} d(t) \tag{B.5}$$

$$e(t) \quad = \quad HK\left(\mathbf{I} + GCHK\right)^{-1}\left(HK\right)^{-1} r(t) - HK\left(\mathbf{I} + GCHK\right)^{-1} d(t) \tag{B.6}$$

$$u(t) \quad = \quad GCHK\left(\mathbf{I} + GCHK\right)^{-1}\left(HK\right)^{-1} r(t) - GCHK\left(\mathbf{I} + GCHK\right)^{-1} d(t) \tag{B.7}$$

The reference and disturbance signals are bounded, and considering the induced system norms of the blocks from figure 5.1, for the reference tracking, disturbance attenuation and less control energy, the minimisation of the $\mathscr{H}_\infty$-norms are related respectively to:

Reference tracking:	$\left\| HK\left(\mathbf{I}+GCHK\right)^{-1}\right\|_\infty$
Disturbance attenuation:	$\left\| HK\left(\mathbf{I}+GCHK\right)^{-1}\right\|_\infty$
Control energy:	$\left\| GCHK\left(\mathbf{I}+GCHK\right)^{-1}\right\|_\infty$

As a standard procedure in optimal robust control, the sensitivity and complementary sensitivity functions can be defined by (B.8) and (B.9).

$$\mathscr{S} := \frac{Y(s)}{D(s)} \tag{B.8}$$

$$\mathscr{T} := 1-\mathscr{S} \tag{B.9}$$

Combining the equations (B.8), (B.9) with (B.5), (B.6) and (B.7), the sensitivity and complementary sensitivity functions from the block diagram from figure 5.1 can be written in (B.10) and (B.11).

$$\mathscr{S} = \left(\mathbf{I}+GCHK\right)^{-1} \tag{B.10}$$

$$\mathscr{T} = \left(\mathbf{I}+GCHK\right)^{-1}GCHK \tag{B.11}$$

In accordance to (B.10) and (B.11) the seek for a stabilising controller can be written with regard to minimisation of the sensitivity function by (B.12).

$$\min_{C \text{ Stabilising}} \quad \left\| HK\left(\mathbf{I}+GCHK\right)^{-1}\right\|_\infty \tag{B.12}$$

In general, the algorithms applied in the optimisation problem (B.12) have difficulties for convergence [53]. By including weighting functions, the stabilising controller to meet the design specifications can be, usually, found.

When the uncertainty block from figure B.2, which transfer matrix given by the linear transformation (B.2), the problem can be translated by μ-synthesis solution problem using *D-K Iteration*.

Such optimisation problem is not convex and, as consequence, the global convergence is not guaranteed. The weighting design for such problem can also represent a troublesome in the process design [55, 56]

B.4 D-K Iteration Algorithm

The μ-synthesis is a control methodology which tries to minimise the structured values in a uncertain system by translating the problem in the definition of

system norms. Usually, the $\mathscr{H}_\infty$ is used. The search for stabilising controllers is made by a iterative method given by the $D-K$ iteration.

Algorithm 4 D-K Iteration Algorithm

Require: Initialisation: initial controller $K_0(s)$
function 1. Closed Loop Function($\mathscr{F}_l(P(s), K_0(s))$)
Calculation of the closed loop function between the plant $P(s)$ and $K_0(s)$
end function
function 2. D-Scale(Upper Bounds)
Calculation of D scale using:

$$\inf_{\mathscr{D}(\omega)} \sigma_{max}\left[\mathscr{D}(\omega)\mathscr{F}_l(P(j\omega), K_0(j\omega))\mathscr{D}^{-1}(\omega)\right]$$

end function
function 3. Design($\mathscr{H}_\infty$)
Design $\mathscr{H}_\infty$ for the system $\mathscr{D}(s)P(s)\mathscr{D}^{-1}(s)$
end function'
Return to 1

APPENDIX C

PSCAD Model

The time domain simulation is built in PSCAD/EMTDC platform. The justification for this choice lies on the fact that PSCAD is a well established simulation tool in the field of power systems. Basically, the model presents four main blocks:

1. Wind farm
2. Offshore HVDC station
3. DC cable
4. Onshore HVDC station
5. Onshore AC grid

The main diagram with the PSCAD modules are presented in figure C.1.

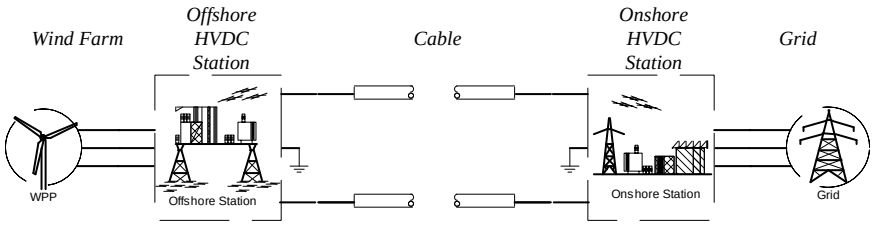

Figure C.1: *PSCAD main block diagram architecture.*

C.1 Wind Farm Model

The wind farm model contains the algebraic equation model for the calculation of currents based on the HVDC converter terminal voltages and the power order. The power model of the aggregated wind farm is, in PSCAD, modelled as current sources. The circuit diagram is presented by figure C.2.

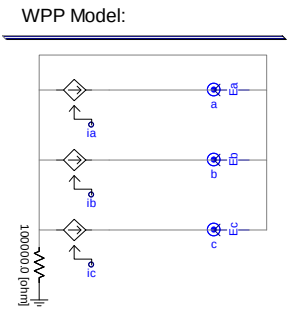

Figure C.2: *PSCAD model for the aggregated wind power plant.*

The nodes Ea, Eb and Ec are the voltage measurements. The labels ia, ib and ic are the signals with the current signals.

The measurement of the voltages passes throughout the park transformation. The references for the currents are calculated using the instantaneous power theory. The input signals for the reference current calculation are the voltages and power references. The first part of the current reference calculation containing the measurement and reference frame transformation is presented in C.3.

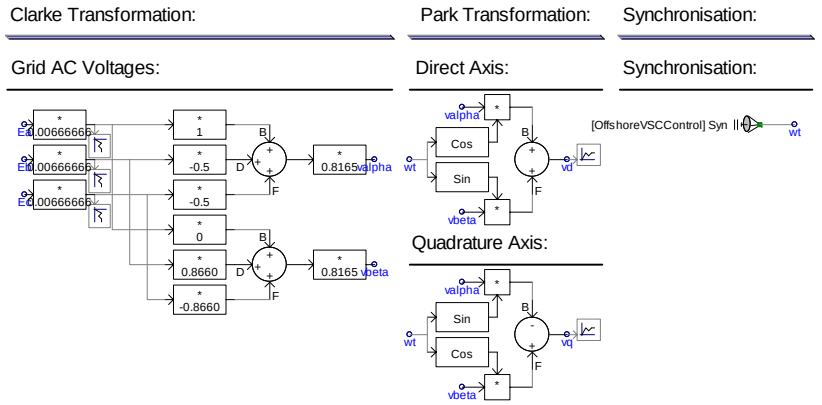

Figure C.3: *Wind power plant measurement and reference transformation.*

The synchronisation signal is an external signal which comes from the offshore HVDC station. The power calculation and inverse reference frame transformation is give by the by the figure C.4.

The external signals of power and reactive power commands are set during the simulation process. In the PSCAD model those signals are labelled with the

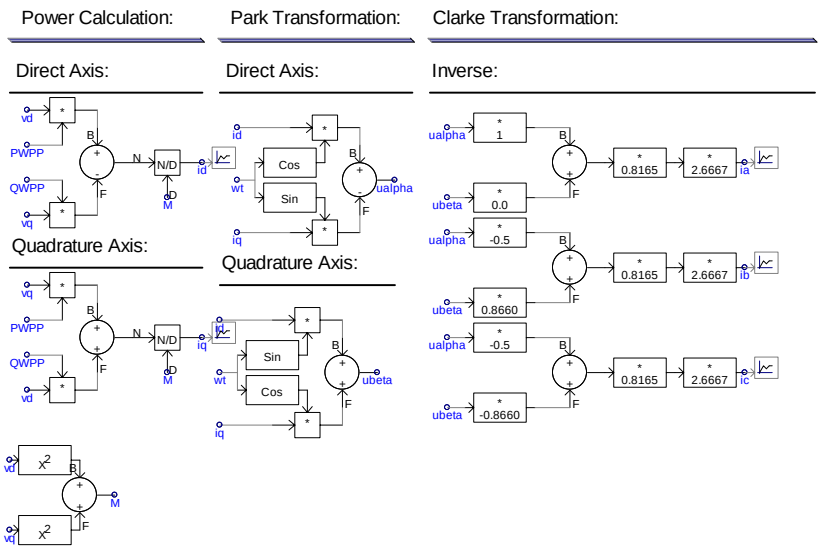

Figure C.4: *Wind power plant power calculation and inverse synchronisation frame.*

node names $PWPP$ and $QWPP$.

During the initialisation process, the signals $PWPP$ and $QWPP$ are forced to be zero. After the start-up of the onshore station and offshore station, a signal is sent to the wind farm module and the power orders are able to be sent to their destination in the model. The block diagram of the start-up sequence of the wind power plant is presented by figure C.5.

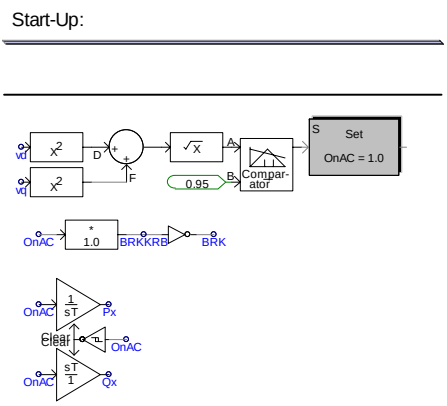

Figure C.5: *Wind farm start-up sequence.*

Signals Px and Qx are the initial values for the power set points $PWPP$ and $QWPP$.

C.2 Offshore Converter Station

The offshore converter station is composed by two main blocks: the converter circuitry and the control module. The interconnected overview of the offshore modules are presented in figure C.6.

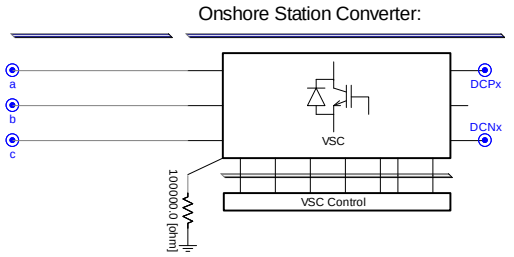

Figure C.6: *Offshore PSCAD model with converter and control modules.*

The AC side presents the nodes a, b and c which are connected to the wind power plant. The DC side nodes are connected by the $DCPx$ and $DCNx$.

Inside the converter circuity module, the voltage source converter is built using the two-level topology. The main components are the converter phase reactor, switching devices, DC capacitor and high frequency filter which is included in a separated block. The circuit schematic of the system is presented in figure C.7.

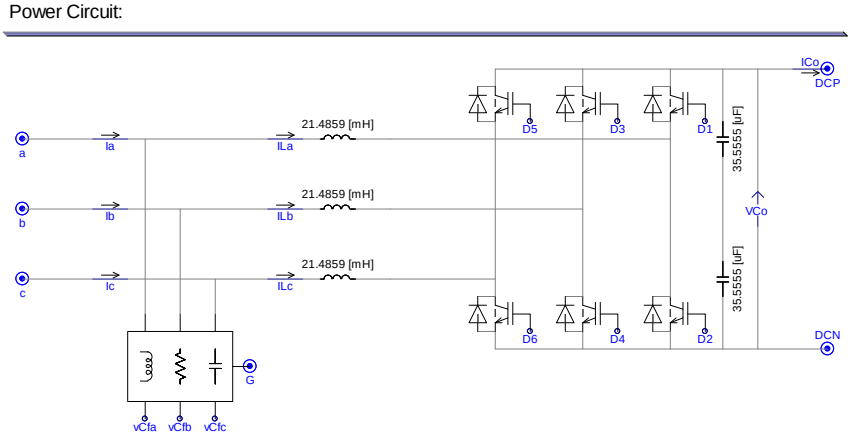

Figure C.7: *Offshore converter circuit schematic.*

The measurement points are indicated in figure C.7. The measurement variables are grid currents, converter currents, DC voltages and filter voltages. The measurement signals are used for control purpose in the controller module. The IGBT devices are controlled by means of PWM signals generated in the control module. The signals related to the modulator are label with dn, where n is the switch number.

The high frequency filter circuit diagram is presented in figure C.8.

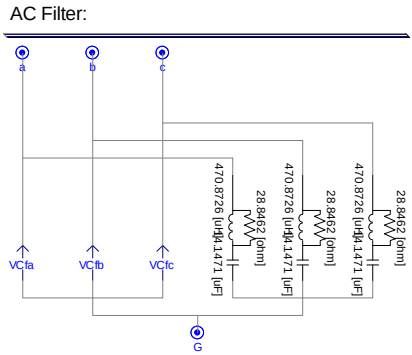

Figure C.8: *Circuit schematic for the high frequency filter.*

The control module is composed by five main modules: the measurements with the feedback gains, the synchronous reference frame transformation, the controllers including PLL (disabled in the offshore station), current controller and AC voltage controller, the inverse reference transformation and the modulator. The five blocks are in the schematic presented by figure C.9.

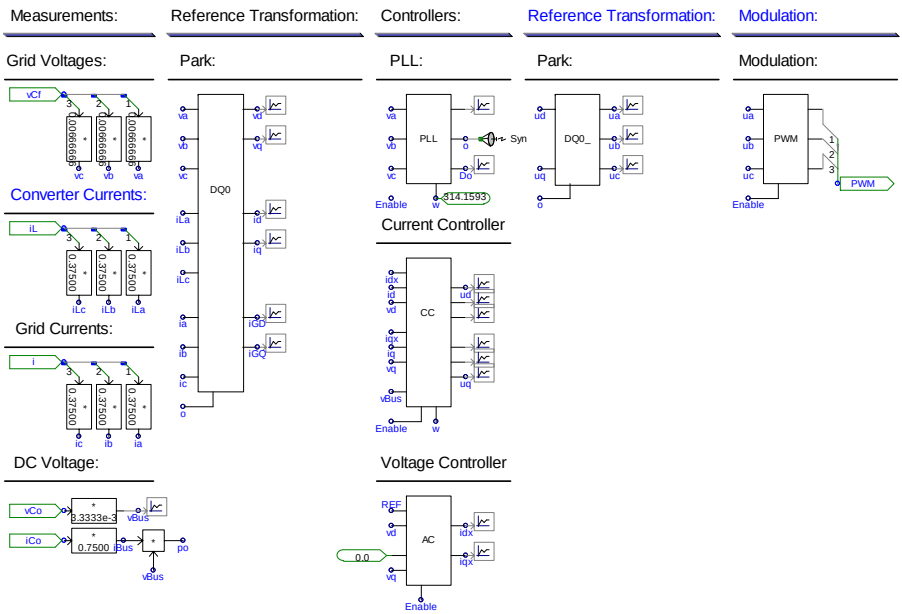

Figure C.9: *Offshore control block diagram.*

The measurement column includes the feedback of the VSC circuit. The variables are scaled by block gains. The next stage in the control flow chart is the synchronous reference transformation. The variables in the *abc* domains are transformed to the ϕdq-frame by means of a linear transformation. The matrix format of given in the main text. In PSCAD, the calculation is made by means of the schematic presented in figure C.10.

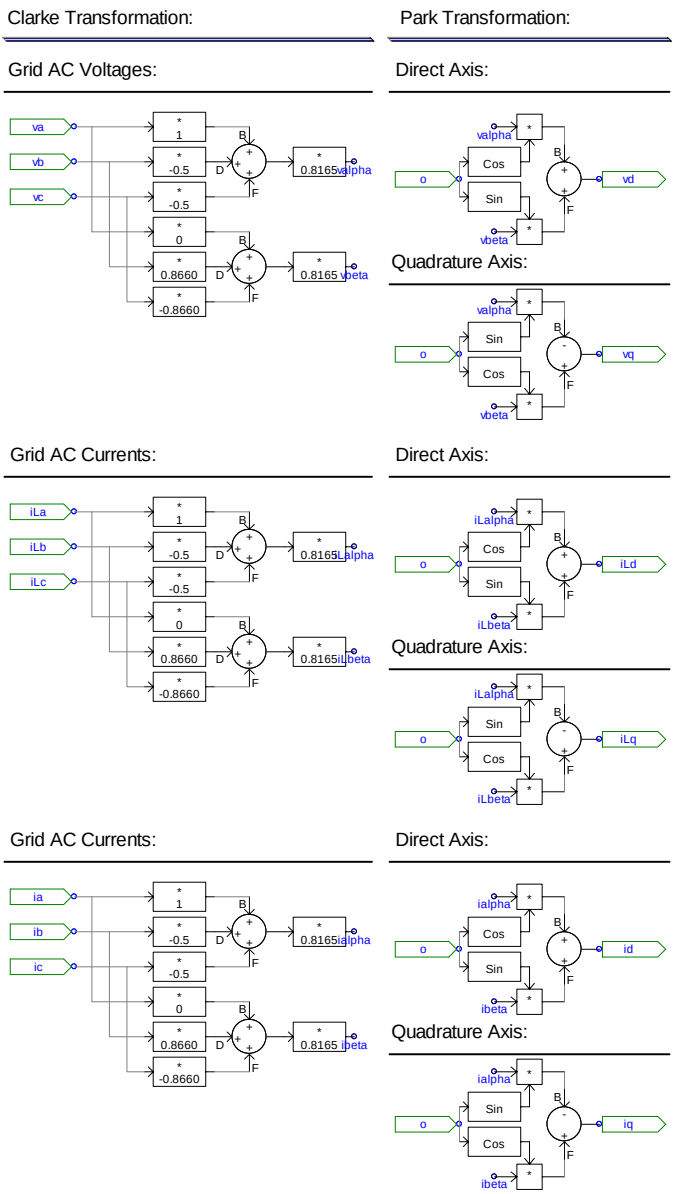

Figure C.10: *Park transformation implemented in PSCAD simulation platform.*

The current controller is the following block in the process. Its main structure is formed by error calculation, PI control with unitary gain, the augmented control block and the feedforwards (decoupling, AC and DC voltages). The PSCAD diagram for the current controller is illustrated in figure C.11.

The central block in the figure C.11 is the implementation of a state space model in C code. During the simulations this block can be changed to a static

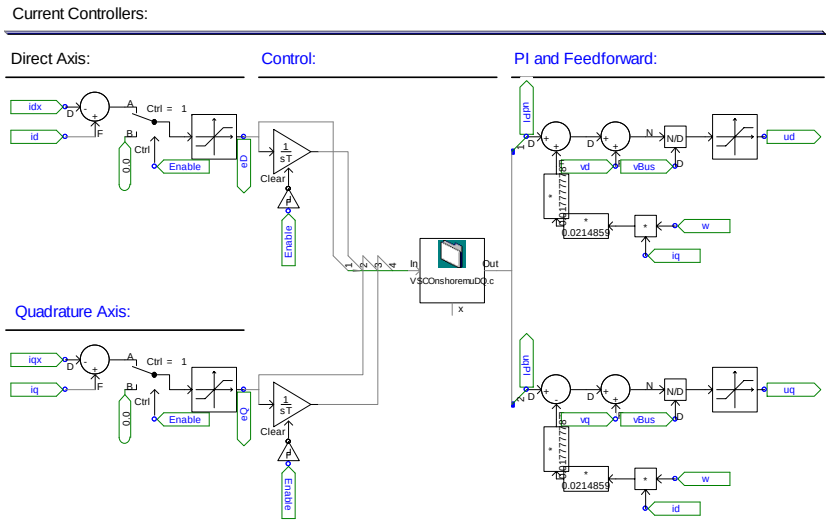

Figure C.11: *PSCAD implementation of the current controller.*

gain, in case of the PI selection control mode, or using the robust controller. For the initialisation purpose, the integrators are not operating. After the a flag indication for normal operation all the integrator are de-blocked.

For the AC voltage controllers, the error signal comparison, unitary PIs and the high order controllers are presented. The high order controller is, again, implemented in a external C function. For th AC voltage controller, the figure C.12 illustrates the implementation in PSCAD of the AC voltage controller for the offshore station.

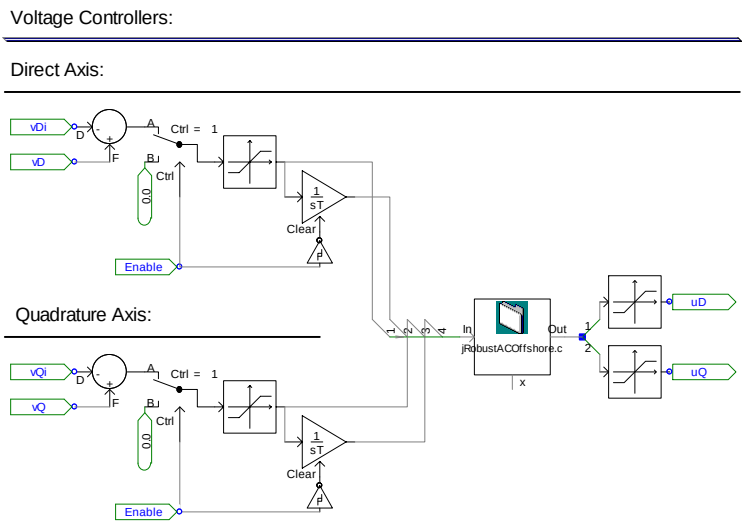

Figure C.12: *PSCAD implementation of the AC voltage controller.*

The inverse reference transformation generates the sinusoidal waveforms which

are going to be compared with the triangular carrier in the modulator. The PSCAD implementation of the inverse synchronous reference frame transformation is illustrated in figure C.13.

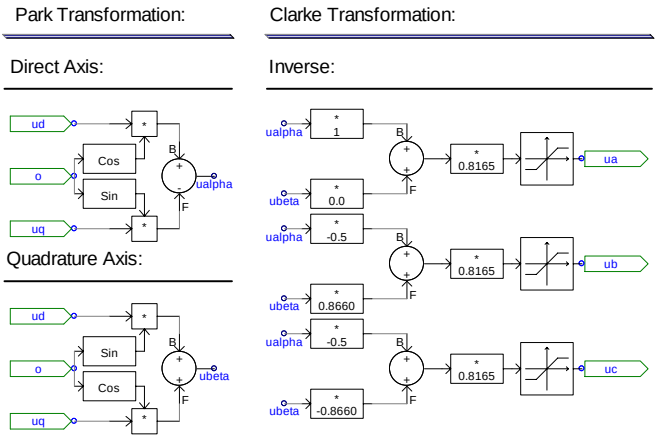

Figure C.13: *Inverse Park transformation implemented in PSCAD simulation platform.*

After the inverse Park's Transformation, the sinusoidal signals are compared with the triangular carrier. This comparison generates the PWM signals which are injected in the IGBT drives in the power circuit. The PSCAD model for the modulator is illustrated in figure C.14.

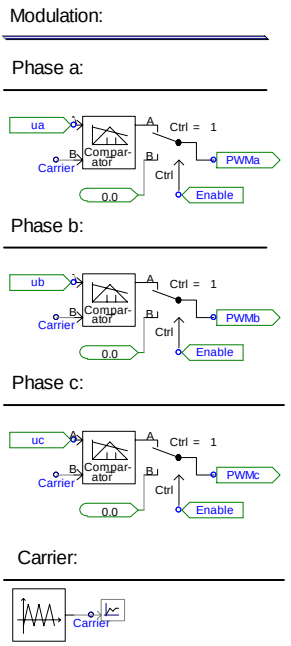

Figure C.14: *Modulation PSCAD implementation schematic.*

The start-up of the offshore station is based in the measurement of the DC voltage presented in the DC link. It is set by assumption that, after the DC voltage achieves more than 97% of the nominal DC voltage, the rest of the controllers are enabled. The start block sequence and commands are shown in figure C.15.

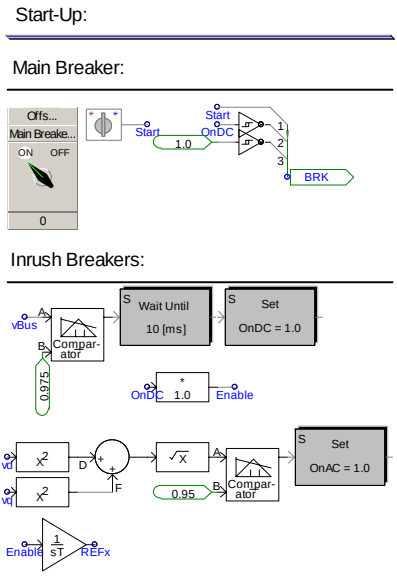

Figure C.15: *Offshore station start-up sequence implementation.*

The signal $REFx$ is the initial value for the AC voltage reference. The integrator generates the ramp signal for the initialisation of the voltage reference. The start-up of the offshore station can be also controlled by the manual control switch from PSCAD blockset.

C.3 Onshore Converter Station

The offshore station has approximately the same structure presented by the offshore station. The main modules, the converter circuit module and the control modules are in the same way connected as in the figure C.6. The onshore converter circuit has, however, fewer components added in order to provide the proper initialisation. The figure C.16 shows the circuit diagram of the onshore converter station.

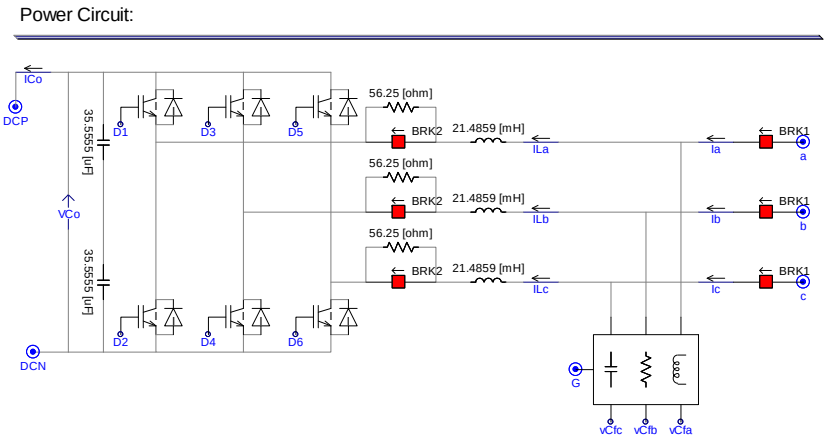

Figure C.16: *Onshore converter circuit schematic.*

From figure C.16, it is possible to observe the presence of two breaker in the main circuit. They are included to the operation of the converter during the start-up.After the main breaker (BRK1) be enabled, the in-rush currents are limited by the series resistors connected in parallel with the in-rush breaker (BRK2). After a control command be send, the in-rush breaker is enabled and the system can go to the normal operation. The rest of the components of the onshore converter circuitry are the same as presented for the offshore converter station.

Compared with the offshore station, the onshore converter control has two main differences. The first off is that the controller is connected to the grid utility and must be in synchronisation with the other generators. For this purpose, the phase-lock loop is included in the control architecture. The block diagram representation of the PLL implemented in PSCAD is given in the figure C.17.

Due to the control operation mode the onshore converter is enabled to regulate the DC voltage across the DC capacitor. As mentioned in the main text, the DC voltage is measured and squared for the compensation of the energy balance in the DC capacitor. The reference signal is provided by the station operator and its value is compared with the measured values squared. This error is compensated, firstly, by the proportional integral controller and after that by the robust controller, if enabled. The current reference signal is then generated after the control compensation.

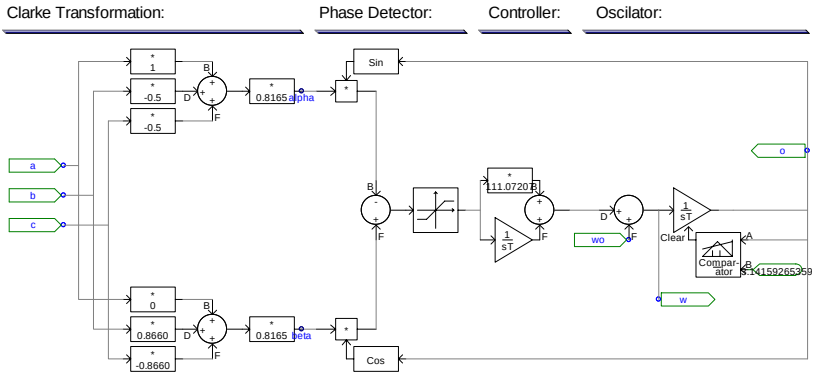

Figure C.17: *Phase-lock loop implementation is PSCAD platform.*

The implementation in PSCAD follows this procedure. The error generation and PI controller are directly extracted from the default PSCAD blocks. The robust controller is implemented suing C function using the same approach which was developed for the current and AC voltage controllers. The PSCAD block diagram of the DC voltage controller is illustrated in figure

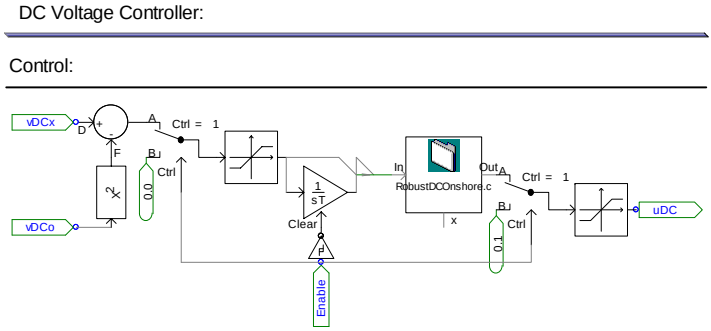

Figure C.18: *PSCAD implementation of the DC voltage controller.*

The start-up sequence of the onshore converter is performed by the control of the operation of the circuit breakers included in the power circuit. First of all, the measurements of the AC voltage initiates the sequence. The main breaker is activated (BRK1) and after the DC voltages achieves 60% of its nominal value the inrush breaker is enabled. The current controller is then activated and the Dc voltage at the DC link is boosted up to its nominal value. After this point, the DC voltage controller is enabled and the converter is under normal operation.

The block diagram showing the flags and measurable variable for the start-up of the onshore HVDC converter is illustrated by the diagram in figure C.19.

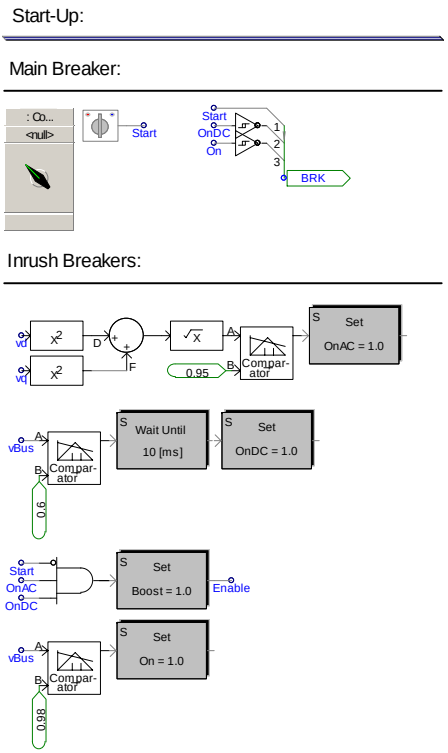

Figure C.19: *Onshrore start-up sequence implementation in PSCAD.*